

ASSEMBLIES OF ASSEMBLIES: SUPRAMOLECULAR ORDERING OF
NANOSCOPIC RUTHENIUM POLYPYRIDYL BUILDING BLOCKS

by

KELLY L. WOUTERS

Presented to the Faculty of the Graduate School of
The University of Texas at Arlington in Partial Fulfillment
of the Requirements
for the Degree of

DOCTOR OF PHILOSOPHY

THE UNIVERSITY OF TEXAS AT ARLINGTON

December 2007

Copyright © by Kelly L. Wouters 2007

All Rights Reserved

ACKNOWLEDGEMENTS

First and foremost, I would like to express my sincere gratitude to my supervising professor, Frederick MacDonnell. Without his guidance, patience, and encouragement, I would never have been able to complete my course of study. He has always impressed me with his continual creativity as well as the depth and breadth of his knowledge of chemistry.

I would also like to thank the members of my committee, Professor Rasika Dias and Professor Krishnan Rajeshwar for their advice and insight. I also want to recognize other faculty members who have assisted me during my studies, especially Professor Dennis Marynick and the late Professor Dmitry Rudkevich. Professor Rudkevich will be warmly remembered by all those who knew him either personally or professionally.

I am enormously indebted to Professor Norma Tacconi for all her hard work. Her endless enthusiasm and optimism is inspiring.

I also wish to acknowledge our collaborators Dr. Nasir Basit and Professor Wiley Kirk for their work regarding the molecular conductivity studies.

I owe many thanks to all the members of the MacDonnell research group, both past and present. Special thanks goes to Dr. Mahn-Jong Kim, Dr. Rama Konduri, Dr. Thamara Janaratne, Mr. Rungano Chitakunye, Ms. Arthi Krishnan, Mr. Cale McAlister, Ms. Fiona Onger, Mr. Abhishek Yadav, and Dr. Shreeyukta Singh not for only their chemistry expertise but also for some fun times as well.

I would like to acknowledge the financial support received from the Robert A. Welch Foundation, National Science Foundation, and The University of Texas at Arlington.

My parents, Edwin and Nora Wouters, deserve special recognition for the many, many years of support and encouragement.

Finally, and in many ways, most importantly, I would like to express my heartfelt gratitude to my wonderful wife, Melina. It is only due to all of her hard work and continuous patience that any of this was even possible. I am forever grateful.

November 7, 2007

ABSTRACT

ASSEMBLIES OF ASSEMBLIES: SUPRAMOLECULAR ORDERING OF NANOSCOPIC RUTHENIUM POLYPYRIDYL BUILDING BLOCKS

Publication No. _____

Kelly L. Wouters, PhD.

The University of Texas at Arlington, 2007

Supervising Professor: Frederick MacDonnell

Biological systems have long since perfected the development of nanoengineering. Cellular structure and machinery is based, to a significant extent, on the formation of nanometer to micron-sized assemblies of proteins. These architectures start with unique primary, secondary, tertiary, and quaternary structural complexity and can be constructed from a relatively simple set of building blocks.

Using this strategy as inspiration, assemblies based on $[\text{Ru}(\text{phenanthroline})_3]^{2+}$ building blocks have been synthesized forming polyruthenium species bridged by the tpphz (tetrapyrido[3,2-a:2',3'-c:3'',2''-h:2''',3'''-j]phenazine) and tatpp (9,11,20,22-tetraaza tetrapyrido[3,2-a:2',3'-c:3'',2''-l:2''',3'''-n]-pentacene) ligands. Importantly, these assemblies exhibit unique hierarchical structural components which

arise directly from the chirality inherent in the octahedral tris chelate $[\text{Ru}(\text{phen})_3]^{2+}$ building blocks. The use of optically pure starting materials allows for the formation of distinct diastereomers, and ultimately, the local stereochemistry can be used to direct the global structure of these complexes. These rigid and robust molecules have been shown to develop primary, secondary, tertiary, and quaternary structural elements, yet, like proteins, are synthesized from a simple set of nanoscopic building blocks.

The quaternary structure arises from the tendency of these complexes to form aggregates. Light scattering experiments have revealed the presence of polydisperse colloids in solution. Further studies using electric birefringence have demonstrated that the nature of these colloids changes with respect to the shape, or tertiary structure of the complexes.

This dissertation describes the behavior of these aggregate structures, these “assemblies of assemblies”, and the effect aggregation has on some of the properties of the complexes.

Scanning tunneling microscopy experiments were conducted in order to observe the native packing structure of these complexes in the solid state. Based on this data as well as crystallographic data of several related compounds, we believe that these complexes assume a stacked columnar arrangement aligned along their central bridging ligands.

Additionally, the conductivity of thin films of these compounds was measured which revealed differences with respect to such factors as counterions, temperature, and global structure.

One particular complex, the tatpp-bridged dimer $[\text{Ru}_2(\text{phen})_4(\text{tatpp})]^{4+}$ (**P**), has been shown to undergo a multielectron photoreduction in the presence of a sacrificial electron donor. It is hoped that it may be possible to affect the efficiency of the photochemical processes via control of the supramolecular ordering of the molecules.

TABLE OF CONTENTS

ACKNOWLEDGEMENTS.....	iii
ABSTRACT	v
LIST OF ILLUSTRATIONS.....	xii
Chapter	
1. INTRODUCTION.....	1
1.1 Nature’s Approach to Nanoengineering	1
1.2 Mimicking Biology Via Ruthenium Polypyridyl Chemistry.....	2
1.2.1 Synthetic Methods	3
1.2.2 Hierarchical Structure	8
1.2.2.1 Primary Structure	9
1.2.2.2 Secondary Structure	9
1.2.2.3 Tertiary Structure	10
1.2.2.4 Quaternary Structure	12
1.3 Scope of Dissertation	15
2. HIERARCHICAL STRUCTURE OF $[\text{Ru}_6(\text{phen})_8(\text{tpphz})_5]^{12+}$	16
2.1 Introduction	16
2.1.1 Hexamer Synthesis	16
2.1.2 Stereospecific Synthesis	19

2.2 Experimental.....	20
2.3 The Meso Ru ₂ Problem.....	23
2.3.1 Side Reaction	23
2.3.2 Synthesis of Meso Ru ₂	25
2.4 Hexamer Tertiary and Quaternary Structure	26
2.4.1 Tertiary Structure of Hexamer.....	26
2.4.2 Quaternary Structure of Hexamer.....	30
2.5 Summary and Conclusion.....	32
3. SCANNING TUNNELING MICROSCOPY IMAGING OF RUTHENIUM POLYPYRIDYL COMPLEXES	33
3.1 Introduction.....	33
3.2 Experimental.....	35
3.3 Results and Discussion	37
3.3.1 Tatpp Bridging Ligand	37
3.3.2 Ruthenium Complexes: Monomers	43
3.3.3 Ruthenium Complexes: Dimers.....	46
3.3.4 Ruthenium Complexes: Hexamers	52
3.4 Summary and Conclusion.....	55
4. ELECTRICAL CONDUCTIVITY	56
4.1 Introduction.....	56
4.2 Experimental.....	59
4.3 Results and Discussion	61
4.3.1 Conductivity of Ruthenium Polypyridyl Complexes	61

4.3.2 Ionic Conduction	64
4.3.3 Effect of Changing the Counterion.....	67
4.3.4 Conductivity of a Neutral Complex.....	70
4.3.5 Temperature Dependence of Conductivity	72
4.3.6 Tertiary Structure and Conductivity	74
4.4 Summary and Conclusion.....	77
5. PHOTOCHEMISTRY AND AGGREGATION.....	78
5.1 Introduction.....	78
5.1.1 Spectroscopic Characterization of P	79
5.1.2 UV-Vis Absorption Spectrum of P	80
5.1.3 Spectra of Reduced Species.....	81
5.1.4 Photochemistry of P	82
5.1.5 The Mechanism of Photoreduction.....	84
5.2 Experimental.....	88
5.3 Aggregation of P	91
5.3.1 Crystals of Related Complexes.....	91
5.3.2 STM Evidence	95
5.3.3 NMR Evidence	95
5.4 Aggregation (Via Concentration) and Reduction.....	98
5.4.1 Kinetics of Photoreduction with Respect to Aggregation	101
5.4.2 Electrochemistry	103
5.5 Aggregation (Via Ionic Strength)	104

5.5.1 NMR.....	104
5.5.2 Mass Spectroscopy	105
5.5.3 Photochemistry	107
5.6 Summary and Conclusion.....	108
REFERENCES	110
BIOGRAPHICAL INFORMATION.....	117

LIST OF ILLUSTRATIONS

Figure		Page
1.1	Ruthenium(II) trisphenanthroline	3
1.2	Synthesis of $\Lambda_3\Delta$ - Ru ₄	5
1.3	Synthesis of Ru ₁₀	6
1.4	Examples of ruthenium polypyridyl complexes.....	8
1.5	Ball-and-stick and space-filling models of Ru ₁₀	11
1.6	Plot of the electric field-induced birefringence signals of $\Lambda_6\Lambda_3\Lambda$ - Ru ₁₀ and $\Lambda_6\Delta_3\Lambda$ - Ru ₁₀	13
1.7	Comparison of hierarchical structural elements.....	14
2.1	Synthesis of $[\text{Ru}_2(\text{phen})_4(\text{tpphz})]^{4+}$	17
2.2	Synthesis of Ru _{2one}	17
2.3	Synthesis of Ru ₆	18
2.4	Partial circular dichroism spectra of $\Lambda\Lambda$ - Ru ₂ and impure $\Delta\Lambda$ - Ru ₂ in MeCN.....	24
2.5	Redox side reaction showing diimine formation and diimine/diamine coupling to form Ru ₂ (bottom).....	25
2.6	Partial circular dichroism spectra of $\Lambda\Lambda$ - Ru ₂ and $\Delta\Lambda$ - Ru ₂ (made in the presence of HOAc) in MeCN	26
2.7	Tertiary structures of Ru ₆ containing dimer cores of $\Lambda\Lambda$, $\Delta\Delta$, and $\Delta\Lambda$	27
2.8	Newman projections of Ru ₂ showing chirality-dependent eclipsed or staggered peripheral phenanthrolines	28

2.9	Molar Circular Dichroism Spectra of Ru₆ Complexes	30
2.10	Plot of electric field-induced birefringence signals of $\Lambda_4(\Delta\Lambda)$ - Ru₆ and $\Lambda_4\Lambda_2$ - Ru₆	31
3.1	STM image of a [Ru(terpy)(terpy-py)](PF ₆) ₂ monolayer on Pt(100)	34
3.2	STM image of an ordered monolayer of Ru ₇ on HOPG	34
3.3	STM image of electrochemically assisted self-assembly of a Zn-tatpp complex on HOPG with a dense packing arrangement	39
3.4	STM image of electrochemically assisted self-assembly of a Zn-tatpp complex on HOPG with a loose packing arrangement	39
3.5	UV-Vis absorption spectrum of the blue film formed by potential cycling in 120 μ M tatpp(Zn) _x ^{y+} with 0.15 M TBAPF ₆ in CH ₃ CN	42
3.6	UV-Vis absorption spectra of tatpp(Zn) in acetonitrile after adding 1 and 2 equivalents of cobaltocene	42
3.7	STM image of 1 (PF ₆) ₂ on HOPG	44
3.8	STM images of HOPG	45
3.9	8.75 nm x 2.75 nm STM image of 1 (PF ₆) ₂ on HOPG	46
3.10	Complexes [Ru ₂ (phen) ₄ tpphz] ⁴⁺ [2 ⁴⁺] and [Ru ₂ (phen) ₄ tatpp] ⁴⁺ [3 ⁴⁺]	47
3.11	STM image of [2 (Cl) ₄] on HOPG showing a domain boundary	48
3.12	50 nm x 50 nm STM image of [2 (Cl) ₄] on HOPG	49
3.13	23 nm x 10 nm STM image of [3 (CF ₃ SO ₃) ₄] on HOPG	50
3.14	STM image of [2 (CF ₃ SO ₃) ₄] on HOPG (2-D Surface plot)	51
3.15	3-D Contour plot of [2 (CF ₃ SO ₃) ₄] on HOPG	52

3.16	$[\text{Ru}_6(\text{phen})_8(\text{tpphz})_5]^{12+}$ [4 ¹²⁺]	53
3.17	STM image of [4 (CF ₃ SO ₃) ₁₂] on HOPG	54
4.1	Complexes $[\text{Ru}_2(\text{phen})_4\text{tpphz}]^{4+}$ [1 ⁴⁺] and $[\text{Ru}_2(\text{phen})_4\text{tatpp}]^{4+}$ [2 ⁴⁺].....	58
4.2	$[\text{Ru}_6(\text{phen})_8(\text{tpphz})_5]^{12+}$ [3 ¹²⁺]	59
4.3	Gold microcontact pattern on the silicon substrate	60
4.4	Cartoon representation of the ruthenium complex as measured with the gold microcontact pattern on the silicon substrate	61
4.5	Current vs. voltage plot of a 1 (Cl) ₄ sample on a glass substrate	63
4.6	Repeat current vs. voltage scans of $[\Lambda_4\Lambda_2\text{-}\mathbf{3}](\text{Cl})_{12}$ on a glass substrate	66
4.7	Current vs. voltage plots of both the Cl and PF ₆ salts of 1 ⁴⁺ on a glass substrate	69
4.8	Enlarged current vs. voltage plot of 1 (PF ₆) ₄ on a glass substrate	69
4.9	$\text{Ru}_2(\text{bpy})_2(\text{oxalato})_2\text{tpphz}$ [4].....	70
4.10	Current vs. voltage plot of 4 on a glass substrate.....	71
4.11	Temperature dependence of $[\mathbf{2}(\text{Cl}_4)]$ conductivity between temperatures of -110 and +85 °C	73
4.12	The current measured at -40 V for $[\mathbf{2}(\text{Cl}_4)]$ as a function of temperature	73
4.13	Ball and stick and space-filling diagrams of $[\Lambda_4(\Delta\Lambda)\text{-}\mathbf{3}]\text{Cl}_{12}$ and $[\Lambda_4\Lambda_2\text{-}\mathbf{3}]\text{Cl}_{12}$	74
4.14	Current vs. voltage plots of $[\Lambda_4(\Delta\Lambda)\text{-}\mathbf{3}]\text{Cl}_{12}$ and $[\Lambda_4\Lambda_2\text{-}\mathbf{3}]\text{Cl}_{12}$ on a glass substrate	76
5.1	Dimers P and Q and their multi-electron photoreduction with a sacrificial reducing agent	78

5.2	Ladder scheme of redox/protonation states of P	79
5.3	Overlaid UV-Vis absorption spectra of [Ru(phen)3] ²⁺ , zinc(II)-tatpp adduct (tatpp), and P in MeCN.....	80
5.4	Absorption spectra in MeCN of P in various redox and protonation states	82
5.5	Photoreduction of P in MeCN.....	83
5.6	Photochemical formation of P *	84
5.7	State diagram for P showing energy migration through the molecule	85
5.8	Return of P * to the ground state.....	86
5.9	Formation of P [•] via reductive quenching of P * by TEA.....	87
5.10	Chemdraw and crystal structures of Z	92
5.11	Chemdraw and crystal structures of Q	93
5.12	PM3 calculation of the HOMO of tatpq.....	94
5.13	Expanded packing crystal structure of Q	94
5.14	STM images of P on HOPG.....	95
5.15	Partial proton NMR spectra of P in D ₂ O at concentrations of 4 mM, 2 mM, and 1 mM.....	98
5.16	Plot of the kinetic data for photoreduction of P at concentration of 16 μM and 160 μM.....	102
5.17	DPV of the first P reduction with increasing concentration	104
5.18	Partial proton NMR spectra of 2 mM P in D ₂ O with no added NaCl and 0.1 M NaCl	105
5.19	ESI-Mass Spectra for P and P with NaCl	106

5.20	Plot of the kinetic data for the photoreduction of P at different ionic strengths.....	108
------	--	-----

CHAPTER 1

INTRODUCTION

1.1 Nature's Approach to Nanoengineering

Nature is very clever. Living organisms rely on assemblies of proteins for their structure and function at the cellular level. Depending on their function, these essential protein complexes can be nanometers to even micrometers in size. For example, microtubules, an important component of the cytoskeleton, playing a role in many processes including mitosis and vesicular transport, have diameters of approximately 25 nm and can be several micrometers in length.^{1,2} To construct such complex microscopic structures from molecular building blocks, nature employs a self-assembly process involving large scale organization of the molecular components.

This marvelous demonstration of nanoengineering is the result of a hierarchical structure strategy, with primary, secondary, tertiary, and quaternary structural elements.^{3,4} When faced with the task of constructing these large cellular components, biological systems begin with a simple recipe: a sequence of amino acids. This sequence of small amino acids essentially contains all the information needed to determine the form and function of a much larger nanoscopic assembly, and is referred to as the primary structure of the complex.

The secondary structure element refers to the local arrangement of the different segments of the protein. The most common secondary structures are α -helices and β -pleated sheets. Moreover, the arrangement of these subunits in three-dimensional space defines the protein's tertiary structure. The overall, folded shape of the protein plays a vital role in determining its biological function. Finally, the quaternary structure describes the manner in which multiple proteins self-assemble into larger functional units. The quaternary arrangement is largely dependent on the tertiary structure, as the most-favorable intermolecular interactions are influenced by molecular shape.

This elegant synthetic approach has inspired supramolecular chemists to explore the possibilities of using non-covalent bonding interactions to assemble molecules into multimolecular complexes.^{5,6} Noteworthy developments in the field of supramolecular chemistry include molecular self-assembly, molecular recognition, and host-guest chemistry.⁷⁻⁹ Work by Zimmerman et. al. has even demonstrated the synthesis of elaborate porphyrin-based structures that actually resemble globular proteins with binding cavities of specific size and shape.¹⁰

1.2 Mimicking Biology Via Ruthenium Polypyridyl Chemistry

One method of mimicking nature's strategy centers on the synthesis of conformationally-rigid, nanometer-sized complexes. The basic building block used throughout this work is the chiral, chemically robust ruthenium(II) trisphenanthroline molecule, shown in Figure 1.1. This complex can be viewed as a three bladed propeller having both a threefold (C_3) symmetry axis and three twofold (C_2) symmetry axes perpendicular to the C_3 axis. This complex exists in two enantiomeric forms: a left-

handed conformation (Λ) and a right-handed one (Δ). These enantiomers of $[\text{Ru}(\text{phen})_3]^{2+}$ are both separable and stable.

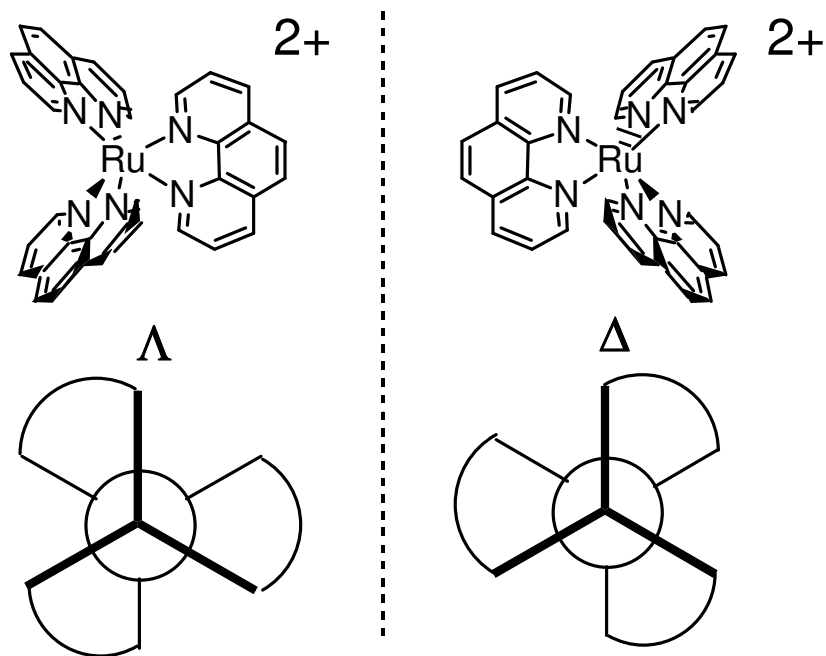


Figure 1.1 Ruthenium(II) trisphenanthroline

1.2.1 Synthetic Methods

To link these ruthenium polypyridyl units together, a series of condensation reactions was employed. Functionalization of the peripheral phenanthroline units allows the addition of complementary dione and diamine reactive species to each building block. The coupling reaction between the dione and diamine is high yield (>90%) and results in the formation of rigid, conjugated bridges between the ruthenium atoms. For example, Figure 1.2 shows the formation of a tetramer where each metal center is connected by the tpphz bridging ligand. With use of enantiomerically pure

starting materials, complexes can be synthesized with precisely defined stereochemistry.

Using this basic synthetic strategy, a wide variety of different complexes can be generated. By further oxidation of the periphery of the multinuclear complexes, larger structures can be formed upon the addition of $[\text{Ru}(\text{phen})_2(\text{phendiamine})]^{2+}$. One example is the decamer shown in Figure 1.3.

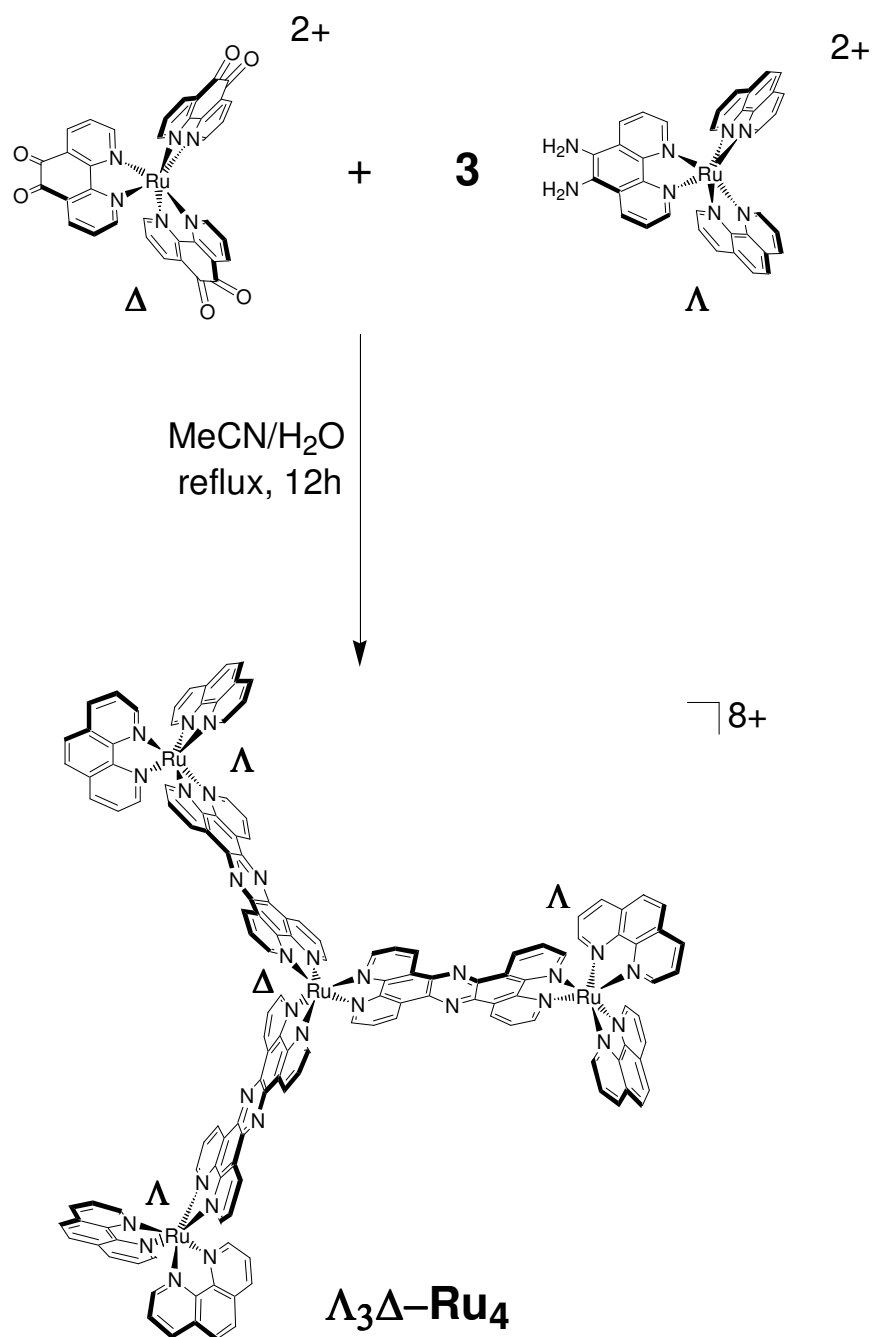


Figure 1.2 Synthesis of $\Lambda_3\Delta\text{-Ru}_4$.

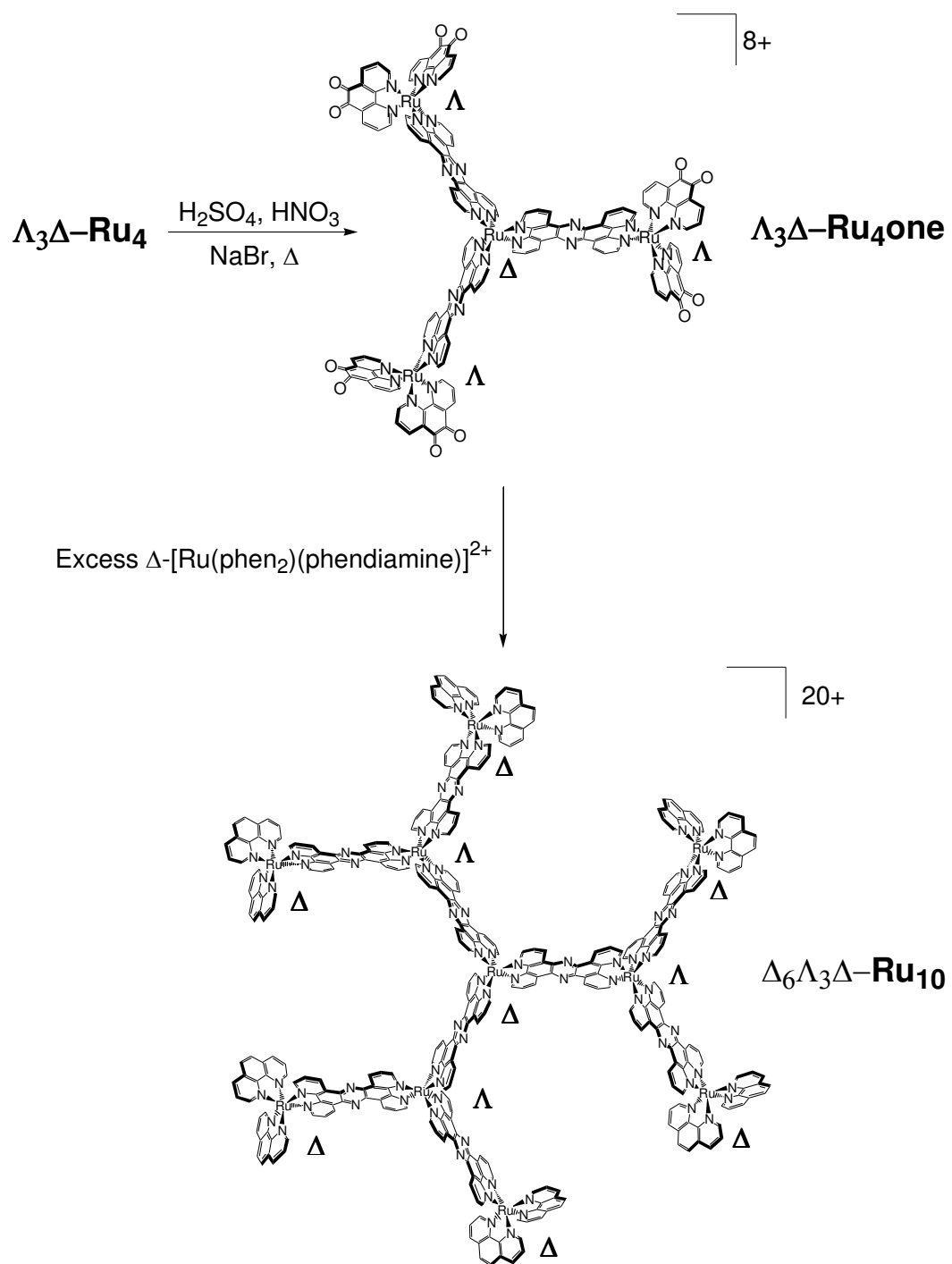


Figure 1.3 Synthesis of Ru_{10} .

Additionally, different routes can be taken to afford the formation of different ligands including tatpp and tatpq. With these tools, we are able to generate a wide variety of complexes that vary with respect to the number of ruthenium centers, the distance between the metal atoms, and chemical (e.g., redox) properties of the bridging ligands. Several of these complexes are shown in Figure 1.4 along with their respective lengths/diameters. It should be noted that all of these assemblies are highly charged cations with each ruthenium atom contributing a +2 charge (**Ru₆** and **Ru₁₀** have charges of +12 and +20, respectively). As a result, in practice, these complexes exist as salts with solubility properties dependent on the counterion. For example, these complexes show good solubility in acetone and acetonitrile as hexafluorophosphate salts and in water and methanol as chloride salts.

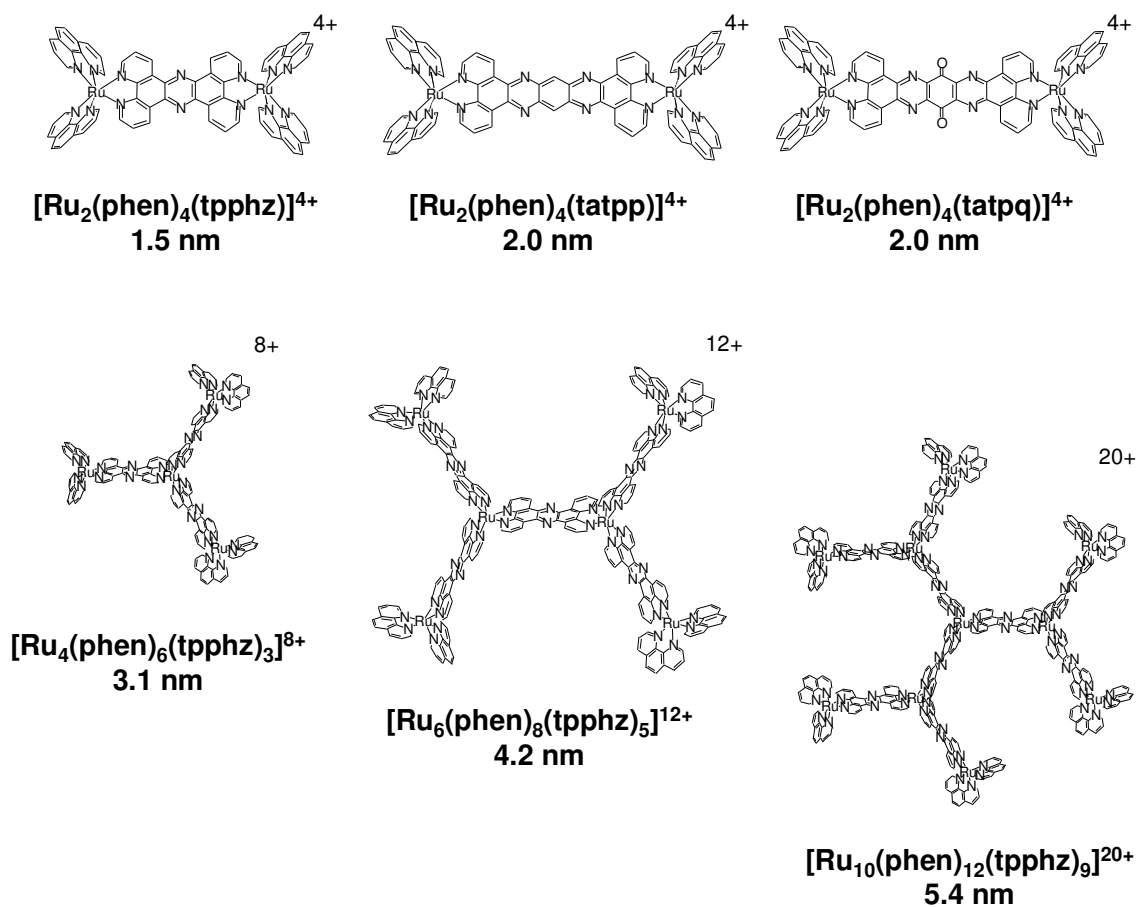


Figure 1.4 Examples of ruthenium polypyridyl complexes.

1.2.2 Hierarchical Structure

Although this system is entirely abiotic, it maintains nature's strategy of utilizing hierarchical structure to generate large assemblies. Hierarchical organization has been demonstrated in other synthetic metal-organic systems. Mixtures of 1,3,5-tricarboxylic benzoic acid molecules and Fe atoms have been shown to assemble and form two-dimensional networks containing higher-order structural elements.¹¹ In addition, light-harvesting columns of zinc phthalocyanine perlenediimide derivatives

have been generated via self-assembly.¹² However, one distinct aspect of our system is that it has primary, secondary, tertiary, and even quaternary structural elements which can be tuned synthetically.

1.2.2.1 Primary Structure

As biology begins with amino acids, we also begin with a relatively simple set of building blocks. However, unlike the set of 20 amino acids biology has at its disposal, we only have two building blocks: the Λ and Δ enantiomers of $[\text{Ru}(\text{phen})_3]^{2+}$ (and its closely related derivatives). Since these enantiomers are separable and stable, we are able to select which form is used in each synthetic step. As a result, we can, for example, make a tetramer with a Δ core, surrounded by three Λ building blocks ($\Lambda_3\Delta\text{-Ru}_4$) or we can construct the opposite sequence ($\Delta_3\Lambda\text{-Ru}_4$). In addition, homochiral species can be synthesized containing either all Λ ($\Lambda_3\Lambda\text{-Ru}_4$) or all Δ ($\Delta_3\Delta\text{-Ru}_4$) ruthenium centers, bringing the total number of synthetically-accessible forms of the tetramer to four species. Each complex is identical except with respect to their enantiomeric compositions. We refer to the stereochemical sequence of the complex as its primary structure.

1.2.2.2 Secondary Structure

In proteins, there exists two common secondary structures: the α -helix and the β -pleated sheet. However, in our system, we only observe one secondary structural element.

The shape of the tetramer, **Ru₄**, (Figure 1.2) is basically triangular, due to the three-fold axis of symmetry at the $[\text{Ru}(\text{phen})_3]^{2+}$ core. However, this structure is

essentially flat, with all four Ru(II) atoms lying in the same plane. Since mathematics requires only three points to define a plane, the fact that these four points are coplanar represents a higher level of ordering. In the larger assemblies (**Ru₆** and **Ru₁₀**), these triangles (four-metal planes) are repeated much like folded proteins can contain multiples of their secondary structural elements.

1.2.2.3 Tertiary Structure

The smaller complexes, such as dimers and tetramers, only exhibit primary and secondary structure. All dimers are essentially rod-shaped and all tetramers are triangular in form. However, the larger assemblies of **Ru₆** and **Ru₁₀** are sufficiently large to begin exhibiting differences in global shape, or tertiary structure.

The manner in which the secondary structural elements are spatially oriented defines the topology (tertiary structure) of the complex. Depending on the chirality of the building blocks (primary structure), the four-metal planes can either lie in the same plane or can be twisted relative to each other. This is a result of how chirality affects the orientation of the peripheral phenantholines when two [Ru(phen)₃]²⁺ building blocks are coupled and will be discussed in more detail in Chapter 2.

For example, in the decamer case, a total of four isomers, $\Lambda_6\Lambda_3\Lambda$ -**Ru₁₀**, $\Lambda_6\Delta_3\Lambda$ -**Ru₁₀**, $\Delta_6\Delta_3\Delta$ -**Ru₁₀**, and $\Delta_6\Lambda_3\Delta$ -**Ru₁₀**, have been previously synthesized.¹³ This notation represents the stereochemistry of the outermost rutheniums first, then the central ring, and then the core site. Figure 1.5 shows two of these complexes, where we see a distinct difference in tertiary structure. The only difference between these two isomers is in the stereochemistry at three sites, but this small change in primary

structure has a dramatic effect on the overall topology. As shown in Figure 1.5, when viewed from the central Ru core, each arm consists of a plane of four ruthenium centers (the secondary structural element). For $\Lambda_6\Delta_3\Lambda$ -**Ru**₁₀, these planes are oriented at an angle of 90° relative to the molecular C₃ axis, indicative of a planar structure where all ten Ru atoms lie in the same plane. For $\Lambda_6\Lambda_3\Lambda$ -**Ru**₁₀, this pitch angle is ~18°, resulting in a massive right-handed propeller structure.

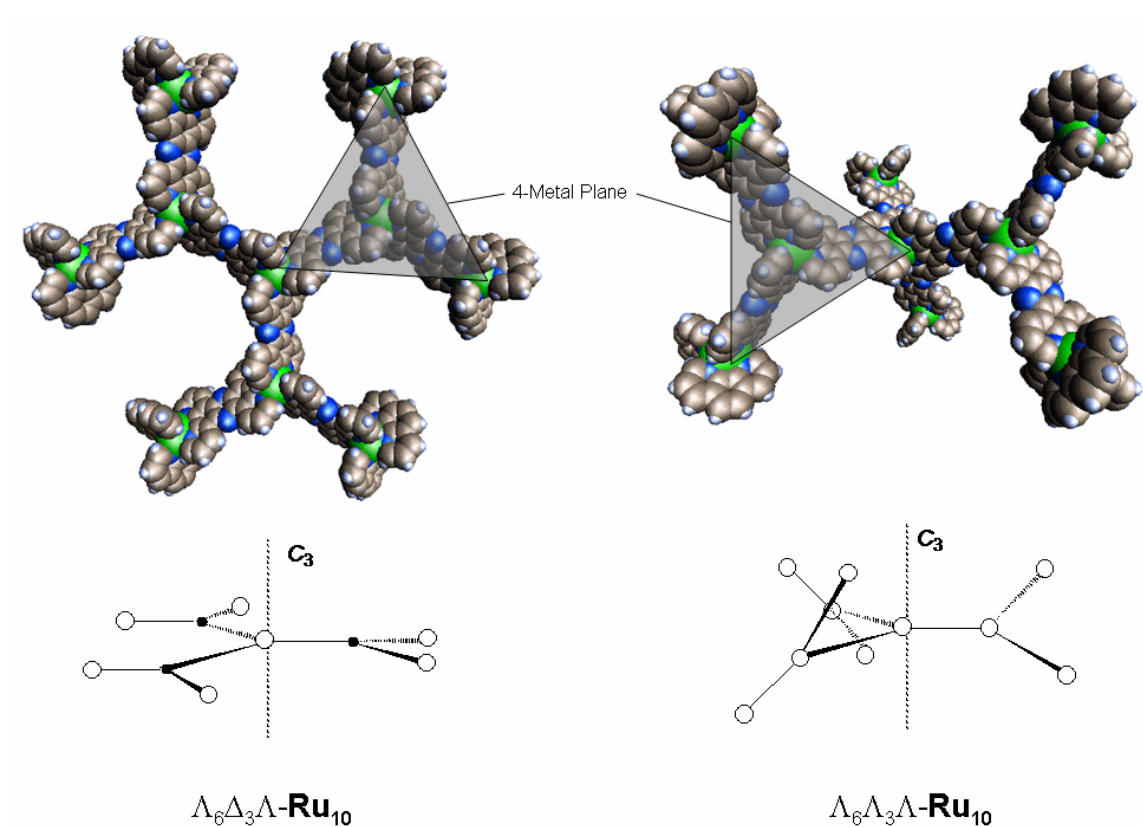


Figure 1.5 Ball-and-stick and space-filling models of **Ru**₁₀.

1.2.2.4 Quaternary Structure

Just as nature groups multiple proteins together to form larger structures, we are studying the ways in which these ruthenium polypyridyl complexes assemble. It has been reported by Kol et. al. that octahedral ruthenium polypyridyl complexes such as $[\text{Ru}(\text{bpy})_2(\text{eilatrin})][\text{PF}_6]_2$ dimerize via π - π stacking in solution.¹⁴ Such intermolecular interactions have been shown in a wide variety of chemical systems to give rise to hierarchical assemblies, often in the form of stacked columns.¹⁵⁻¹⁷

Previous experiments with our ruthenium complexes have shown that this family of molecules is colloidal in solution.¹⁸ In addition, further studies on the decamer have shown that these aggregates are polydisperse, and that there are marked differences in their aggregate structures.¹³ Importantly, these differences are directly affected by their topology (tertiary structure) and represent the existence of a quaternary level of structural hierarchy.

Using electric birefringence, the colloidal properties of the decamer were shown to be different for $\Lambda_6\Delta_3\Lambda$ -**Ru10** and $\Lambda_6\Lambda_3\Lambda$ -**Ru10**. For the flat $\Lambda_6\Delta_3\Lambda$ -**Ru10** isomer, the amplitude of the birefringence is small and the corresponding decay signal is fast (on the microsecond timescale). On the other hand, for the twisted $\Lambda_6\Lambda_3\Lambda$ -**Ru10** isomer, the amplitude of the birefringence is much larger and the decay far slower (on the second timescale).

To confirm that these differences were related to tertiary structure only, two tetramers were also examined: $\Lambda_3\Delta$ -**Ru4** and $\Lambda_3\Lambda$ -**Ru4**. These complexes have similar three-dimensional shapes, but also form polydisperse colloids in solution. The electric

birefringence signals for these complexes were indistinguishable, indicating no difference in their aggregate structures.

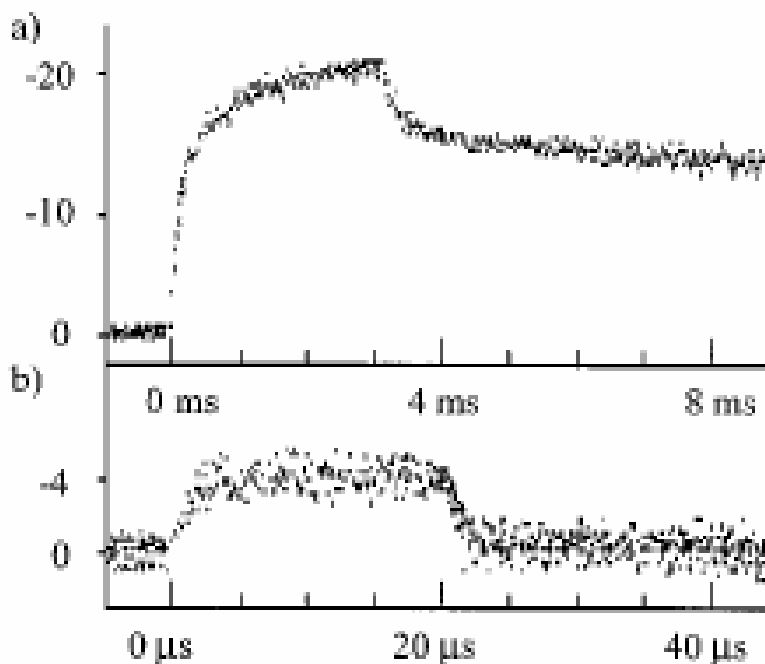


Figure 1.6 Plot of the electric field-induced birefringence signals ($E = 4.8$ kV/cm) of $\Lambda_6\Lambda_3\Lambda$ -**Ru10** (a: top trace, pulse length = 3 ms) and $\Lambda_6\Delta_3\Lambda$ -**Ru10** (b: bottom trace, pulse length = 20 ms). The ordinate is proportional to the transmitted light intensity.¹³

The presence of variable quaternary organization completes the analogy between our system and biology. An overall hierarchical structure comparison between these complexes and biology is shown in Figure 1.7. Importantly, the global structure of these compounds can be tuned by exploiting the chirality inherent in the octahedral $[\text{Ru}(\text{phen})_3]^{2+}$ building block. Since this tertiary structure affects the quaternary packing, we can essentially use the local stereochemistry of each building block to direct the intermolecular interactions. This research represents an entirely

nonbiological system that has the capability to mimic the higher order structures observed in protein assemblies.

This synthetic strategy demonstrates one way to organize nanoscopically-sized complexes over large distances. Ultimately, the basic principles and discoveries described herein could eventually lead to the development of new applications, materials, and devices.

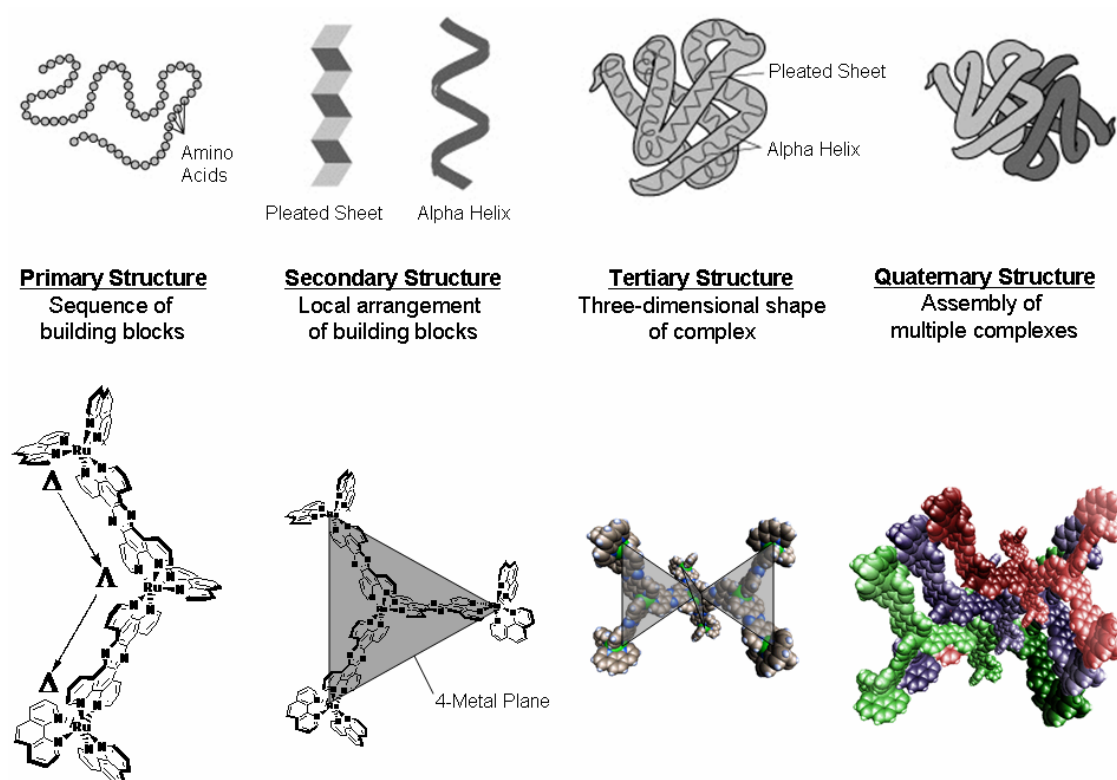


Figure 1.7 Comparison of hierarchical structural elements.

1.3 Scope of Dissertation

This dissertation will focus on various aspects regarding the intermolecular (quaternary) interactions of these ruthenium polypyridyl complexes. Using a variety of approaches and techniques, we will examine the nature of the assemblies of these nanoscopic molecules. Chapter 2 discusses the development of quaternary structure in the hexanuclear Ru(II) complex. In Chapter 3, we will examine the solid-state packing arrangements of these molecules and their component ligands using scanning tunneling microscopy. Chapter 4 covers the electrical conductivity of thin films of these complexes. Finally, the consequences of solution aggregation on the photochemical properties of some of these complexes is presented in Chapter 5.

CHAPTER 2

HIERARCHICAL STRUCTURE OF $[\text{Ru}_6(\text{phen})_8(\text{tpphz})_5]^{12+}$

2.1 Introduction

Due to the chemical properties of the planar aromatic tpphz bridging unit, these nanoscopically-sized building blocks are robust, rigid, and exhibit well-defined topologies. But of all the ruthenium polypyridyl complexes studied in our lab, the hexamer presents an interesting case, for it is the smallest of these species to exhibit differences in tertiary structure. Previous experiments had investigated the effect of tertiary structural differences on the quaternary organization of the decamer,¹³ but the structure of the hexamer had not yet been studied.

2.1.1 Hexamer Synthesis

Like the decamer, **Ru₆** is built stepwise beginning with its core. However, instead of building around a single $[\text{Ru}(\text{phen})_3]^{2+}$ unit, the central core of the hexamer is a dimer bridged by the tpphz ligand. This dimer core is synthesized via the coupling reaction shown in Figure 2.1.¹⁹ The complex $[\text{Ru}(\text{phen})_2(\text{phendione})]^{2+}$ is reacted with $[\text{Ru}(\text{phen})_2(\text{phendiamine})]^{2+}$ to form the $[\text{Ru}_2(\text{phen})_4(\text{tpphz})]^{4+}$ dimer.

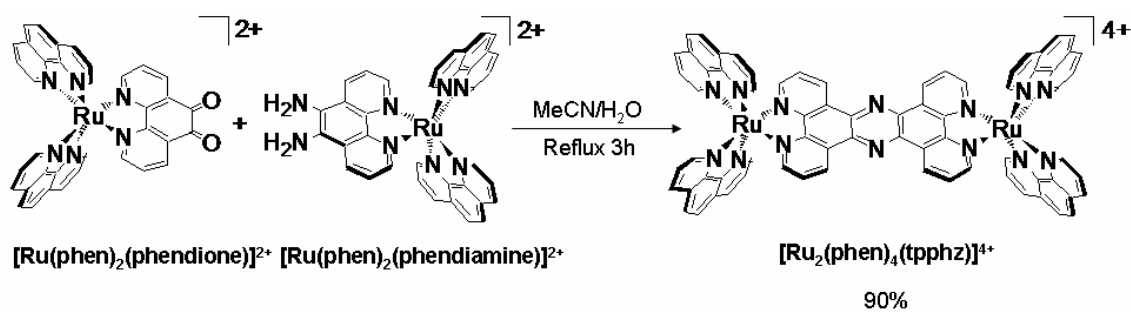


Figure 2.1 Synthesis of $[\text{Ru}_2(\text{phen})_4(\text{tpphz})]^{4+}$

Once this step is complete, the peripheral phenanthroline units are oxidized at the 5 and 6 positions to generate the tetradione complex (**Ru₂one**) shown in Figure 2.2.²⁰⁻²² This product is then reacted with an excess of $[\text{Ru}(\text{phen})_2(\text{phendiamine})]^{2+}$ which couples with the dione-functionalized periphery, forming the hexamer.²³

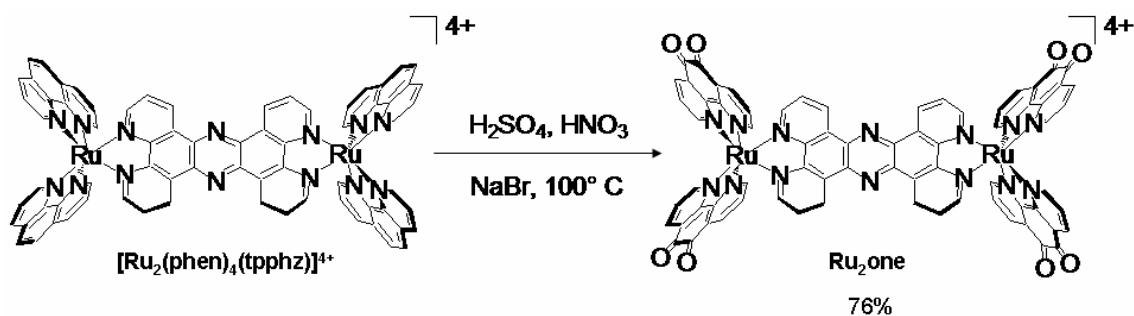


Figure 2.2 Synthesis of **Ru₂one**.

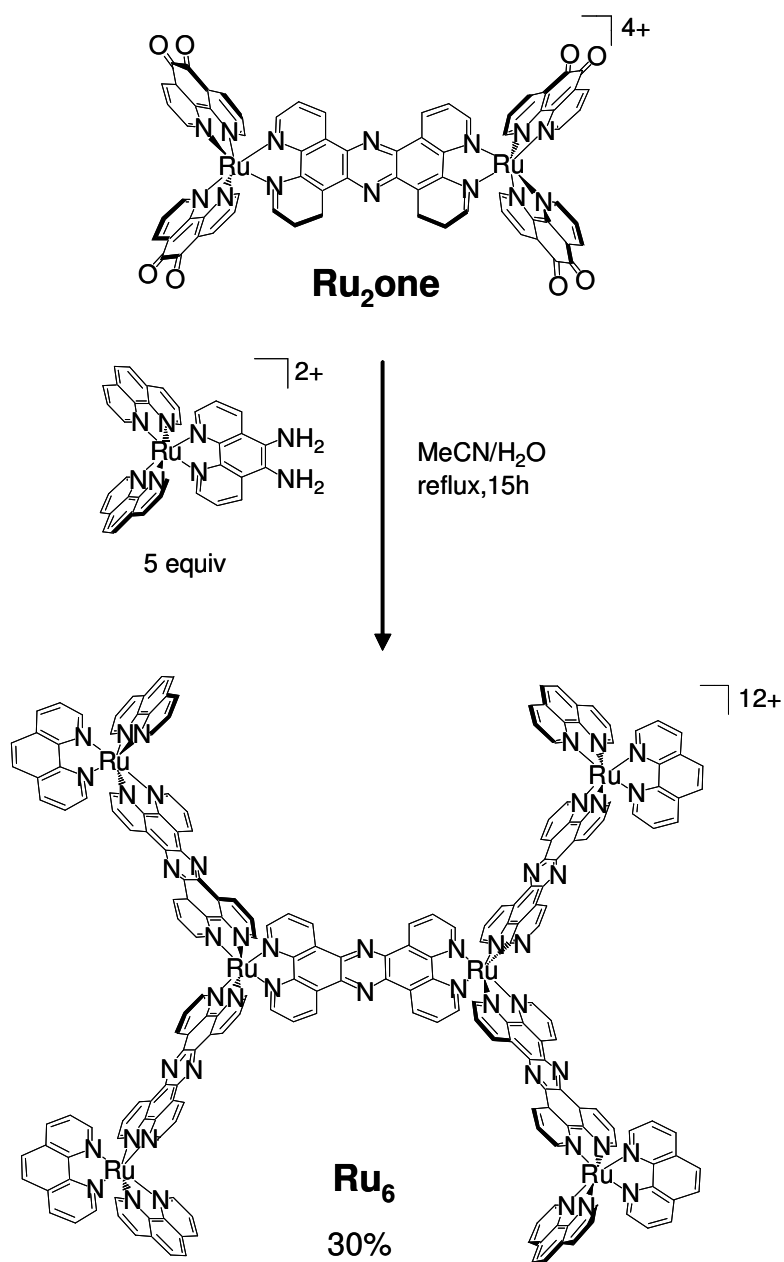


Figure 2.3 Synthesis of **Ru₆**.

2.1.2 Stereospecific Synthesis

Using enantiomerically-pure building blocks, hexamers can be synthesized in a stereospecific manner. Through careful selection of the starting materials, we can predetermine the primary structure of each complex. In the first step, the synthesis of the dimer core, $[\text{Ru}(\text{phen})_2(\text{phendione})]^{2+}$ and $[\text{Ru}(\text{phen})_2(\text{phendiamine})]^{2+}$ can be added as either their Δ or Λ forms. As a result, three different diastereomers can be generated: $\Delta\Delta\text{-Ru}_2$, $\Lambda\Lambda\text{-Ru}_2$, and the meso complex $\Delta\Lambda\text{-Ru}_2$. Each of these dimers can be oxidized to form their respective tetradione complex: $\Delta\Delta\text{-Ru}_2\text{one}$, $\Lambda\Lambda\text{-Ru}_2\text{one}$, and $\Delta\Lambda\text{-Ru}_2\text{one}$. Despite the harsh reaction conditions (sulfuric acid, nitric acid and NaBr at 100 °C), this reaction leaves the stereochemistry unchanged as determined using NMR with chiral lanthanide shift reagents.²²

In the final synthetic step, either Δ - or Λ - $[\text{Ru}(\text{phen})_2(\text{phendiamine})]^{2+}$ is added resulting in a total of six possible isomeric hexamers: $\Delta_4\Delta_2\text{-Ru}_6$, $\Lambda_4\Delta_2\text{-Ru}_6$, $\Lambda_4\Lambda_2\text{-Ru}_6$, $\Delta_4\Lambda_2\text{-Ru}_6$, $\Delta_4(\Delta\Lambda)\text{-Ru}_6$, and $\Lambda_4(\Delta\Lambda)\text{-Ru}_6$. This notation gives the stereochemistry of the peripheral rutheniums first, and then the core sites. Other diastereomers of the hexamer exist, but they are not directly accessible via this synthetic approach because we are not able to differentiate the chirality at each of the four peripheral sites. As a result, a structure consisting of, for example, a $\Delta\Delta$ dimer core surrounded by one Δ and three Λ building blocks cannot be formed directly. However, if all racemic starting materials are used, we can generate a statistical mixture of all possible diastereomers.

Previously, the hexamers with homochiral cores ($\Delta_4\Delta_2\text{-Ru}_6$, $\Lambda_4\Delta_2\text{-Ru}_6$, $\Lambda_4\Lambda_2\text{-Ru}_6$, and $\Delta_4\Lambda_2\text{-Ru}_6$) were generated.²⁴ However, problems with the synthesis of the

hexamers containing the meso $\Delta\Delta$ core still needed to be overcome. A side reaction prevented the synthesis of the requisite $\Delta\Delta$ -**Ru2** with sufficient optical purity.

2.2 Experimental

Instrumentation. ^1H NMR spectra were obtained on JEOL Eclipse Plus 500 MHz spectrometer using CD_3CN as the solvent unless otherwise noted. Chemical shifts were given in ppm and referenced to TMS. UV-visible absorption data were obtained using a Hewlett-Packard HP8453A spectrophotometer in MeCN. Circular dichroism spectra were recorded on a Jasco-710 spectrophotometer in MeCN. Electric birefringence measurements were obtained on a locally constructed instrument which has been described previously.²⁵

Computational modeling was carried out using the SPARTAN suite of programs developed by Wave-function, Inc. The default optimization criteria was used in all cases.

Chemicals. The $[\text{Ru}(\text{phen})_2(\text{phendione})][\text{PF}_6]_2$ was prepared from the reaction of $\text{Ru}(\text{phen})_2\text{Cl}_2$ and 1,10-phenanthroline-5,6-dione and then resolved into Λ and Δ stereoisomers using previously published procedures.^{24,26} $[\text{Ru}(\text{phen})_2(\text{phendiamine})][\text{PF}_6]_2$, $\Lambda\Lambda$ - $[\text{Ru}_2(\text{phen})_4(\text{tpphz})][\text{PF}_6]_2$ ($\Lambda\Lambda$ -**Ru₂**), and $\Delta\Delta$ - $[\text{Ru}_2(\text{phen})_4(\text{tpphz})][\text{PF}_6]_2$ ($\Delta\Delta$ -**Ru₂**) were prepared as described previously.^{24,27} All other chemicals and solvents used were of reagent grade and used without further purification. All the reactions were carried out under N_2 gas and protected from direct light to avoid photochemical degradation.

$\Delta\Delta$ -[Ru₂(phen)₄(tpphz)][PF₆]₂ ($\Delta\Delta$ -Ru₂)

A solution of Δ -[Ru(phen)₂(phendione)][PF₆]₂ (150 mg, 0.156 mmol) and Λ -[Ru(phen)₂(phendiamine)][PF₆]₂ (150 mg, 0.156 mmol) in 50 mL of 4:1 MeCN:HOAc was refluxed under N₂ for 12 h. The solution was cooled to room temperature, transferred to an Erlenmeyer flask, and treated with 10 M NaOH (aq) until the pH = 10. The solution was then allowed to stand for 2 h. After neutralization to pH = 7 with HCl, the product was precipitated by the addition of 10 mL of a saturated aqueous solution of NH₄PF₆. The precipitate was filtered, washed with H₂O (3 x 10 mL) and purified via alumina column chromatography using 1 % NH₄PF₆ in MeCN as an eluent. The product was then dried *in vacuo* at 60°C for 12 h. Yield: 215 mg (73%). ¹H NMR (δ , 500 MHz, MeCN-d₆) 10.11 (d, *J* = 14.0 Hz, 4H), 8.54 (d, *J* = 8.8 Hz, 8H), 8.43 (s, 8H), 8.35 (d, *J* = 8.6 Hz, 4H), 8.03 (dd, *J*₁ = 14.0 Hz, *J*₂ = 9.1 Hz, 4H), 8.02 (d, *J* = 13.4 Hz, 8H), 7.83 (m, 8H). Mol. CD [MeCN, $\lambda_{\text{max/min}}$, nm ($\Delta\epsilon$, M⁻¹cm⁻¹): 477 nm (2), 419 nm (-4).

$\Delta\Delta$ -[Ru₂(phendione)₄(tpphz)][PF₆]₄ ($\Delta\Delta$ -Ru₂one)

$\Delta\Delta$ -[Ru₂(phen)₄(tpphz)][PF₆]₄ (0.27 g, 0.13 mmol) was dissolved in 3 mL of concentrated sulfuric acid chilled in an ice-water bath. After dissolution was complete, 0.125 g of sodium bromide and 2.5 mL of nitric acid were added and the solution was heated to 100°C for 20 minutes. The solution was then cooled to room temperature and poured into 50 mL of ice water containing 5 g of sodium perchlorate. The solution was refrigerated for 12 h and then filtered and washed with water. The precipitate was then redissolved by stirring with 10 g of DOWEX 21K anion exchange resin (Cl⁻ form) in 30

mL of H₂O. The mixture was then filtered, and the product was precipitated by treating the filtrate with 10 mL of a saturated aqueous solution of NH₄PF₆. The precipitate was filtered, washed with H₂O (3 x 10 mL) and reprecipitated from MeCN using additional aqueous NH₄PF₆ solution. The product was then filtered, washed with H₂O, dried *in vacuo* at 60°C for 12 h. Yield: 0.21 g (76%). ¹H NMR (δ, 500 MHz, MeCN-d₆) 10.04 (d, *J* = 7.8 Hz, 4H), 8.63 (d, *J* = 8.1 Hz, 4H), 8.52 (d, *J* = 16.1 Hz, 4H), 8.44 (d, *J* = 10.3 Hz, 4H), 8.23 (d, *J* = 9.8 Hz, 4H), 8.07 (dd, *J*₁ = 16.2 Hz, *J*₂ = 10.8 Hz, 4H), 8.01 (d, *J* = 10.8 Hz, 4H), 7.74 (dd, *J*₁ = 16.2 Hz, *J*₂ = 11.2 Hz, 4H), 7.52 (dd, *J*₁ = 15.6 Hz, *J*₂ = 11.2 Hz, 4H).

Λ₄(ΔΛ)-[Ru₆(phen)₈(tpphz)₅][PF₆]₁₂ (Λ₄(ΔΛ)-Ru₆)

A mixture of ΔΛ-[Ru₂(phendione)₄(tpphz)][PF₆]₄ (35 mg, 0.017 mmol) and Λ-[Ru(phen)₂(phendiamine)][PF₆]₂ (77 mg, 0.076 mmol) were dissolved in 10 mL of 2:1 MeCN:H₂O and refluxed under N₂ for 12 h. The product was precipitated by the addition of 5 mL of a saturated aqueous solution of NH₄PF₆. The precipitate was filtered, washed with H₂O (3 x 5 mL) and dried *in vacuo* at 60°C for 12 h. The product was purified via alumina column chromatography using 1 % NH₄PF₆ in MeCN as an eluent. The first dark orange band was collected and reduced to a volume of 2 mL which was then loaded onto a Sephadex LH-20 size exclusion column and eluted with 1:1 MeCN:THF. Yield: 30 mg (30%). ¹H NMR (δ, 500 MHz, MeCN-d₆) 10.04 (d, 4H), 10.01 (d, *J* = 8.6 Hz, 8H), 9.95 (d, *J* = 8.0 Hz, 8H), 8.63 (d, *J* = 8.1 Hz, 16H), 8.47 (d, *J* = 5.1 Hz, 12H), 8.28 (s, 16H), 8.24 (s, 16H), 8.04 (d, *J* = 4.6 Hz, 8H), 7.96 (dd, *J*₁ = 8.3 Hz, *J*₂ = 5.4 Hz, 12H), 7.89 (dd, *J*₁ = 7.9 Hz, *J*₂ = 5.6 Hz, 8H), 7.67 (dd, *J*₁ = 13.7

Hz, $J_2 = 8.6$ Hz, 16H). UV/vis: [MeCN, $\lambda_{\text{max/min}}$, nm (ϵ , $\text{M}^{-1}\text{cm}^{-1}$): 440 nm (136000), 371 nm (162000), 302 nm (279000), 279 nm (436000), 264 nm (472000), 220 nm (346000). Mol. CD [MeCN, $\lambda_{\text{max/min}}$, nm ($\Delta\epsilon$, $\text{M}^{-1}\text{cm}^{-1}$): 477 nm (70), 419 nm (-57), 271 nm (1154), 258 nm (-876).

2.3 The Meso Ru₂ Problem

2.3.1 Side Reaction

Synthesis of the homochiral ruthenium dimers, $\Delta\Delta\text{-Ru}_2$ and $\Lambda\Lambda\text{-Ru}_2$, proceeded via the condensation reaction shown in Figure 2.1. However, synthesis of meso $\Delta\Lambda\text{-Ru}_2$ was not as straightforward. The reaction of $\Delta\text{-[Ru(phen)}_2\text{(phendione)]}^{2+}$ and $\Lambda\text{-[Ru(phen)}_2\text{(phendiamine)]}^{2+}$ under the same conditions generated two products: $\Delta\Lambda\text{-Ru}_2$ and $\Lambda\Lambda\text{-Ru}_2$. An analysis of the CD spectra of this product mixture compared to a sample of $\Lambda\Lambda\text{-Ru}_2$ (Figure 2.4) revealed that the homochiral impurity composed approximately 23% of the sample. Alternatively, if $\Lambda\text{-[Ru(phen)}_2\text{(phendione)]}^{2+}$ and $\Delta\text{-[Ru(phen)}_2\text{(phendiamine)]}^{2+}$ were used, the minor product formed was $\Delta\Delta\text{-Ru}_2$. The homochiral impurity was always found to have the same stereochemistry as the diamine precursor.

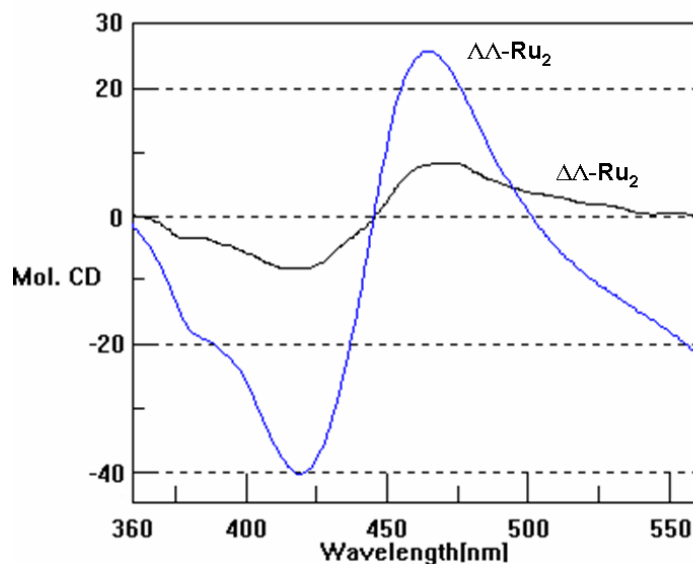


Figure 2.4 Partial circular dichroism spectra of $\Lambda\Lambda\text{-Ru}_2$ and impure $\Delta\Lambda\text{-Ru}_2$ in MeCN.

This phenomenon is explained by the presence of a redox side-reaction shown in Figure 2.5. In this alternate pathway, some of the diamine complex is oxidized by the quinone to generate a diimine. This species can react with remaining $[\text{Ru}(\text{phen})_2(\text{phendiamine})]^{2+}$ to form the homochiral tpphz -bridged dimer and eliminate NH_3 . In essence, the diamine complex couples with itself so a reaction containing $\Lambda\text{-}[\text{Ru}(\text{phen})_2(\text{phendiamine})]^{2+}$ results in the formation of homochiral $\Lambda\Lambda\text{-Ru}_2$. This is not a problem when synthesizing $\Delta\Delta\text{-Ru}_2$ or $\Lambda\Lambda\text{-Ru}_2$ since both the main and side-reaction pathways result in formation of the same product.

It should also be noted that this side reaction manifests itself in other reactions such as the final step in the formation of the hexamer (Figure 2.3). Since the quinone functionality of the **Ru₂one** is also capable of generating the diimine, a mixture of the

dimer and hexamer is formed during synthesis. Fortunately, it has been possible to remove this dimer side-product using size exclusion chromatography.

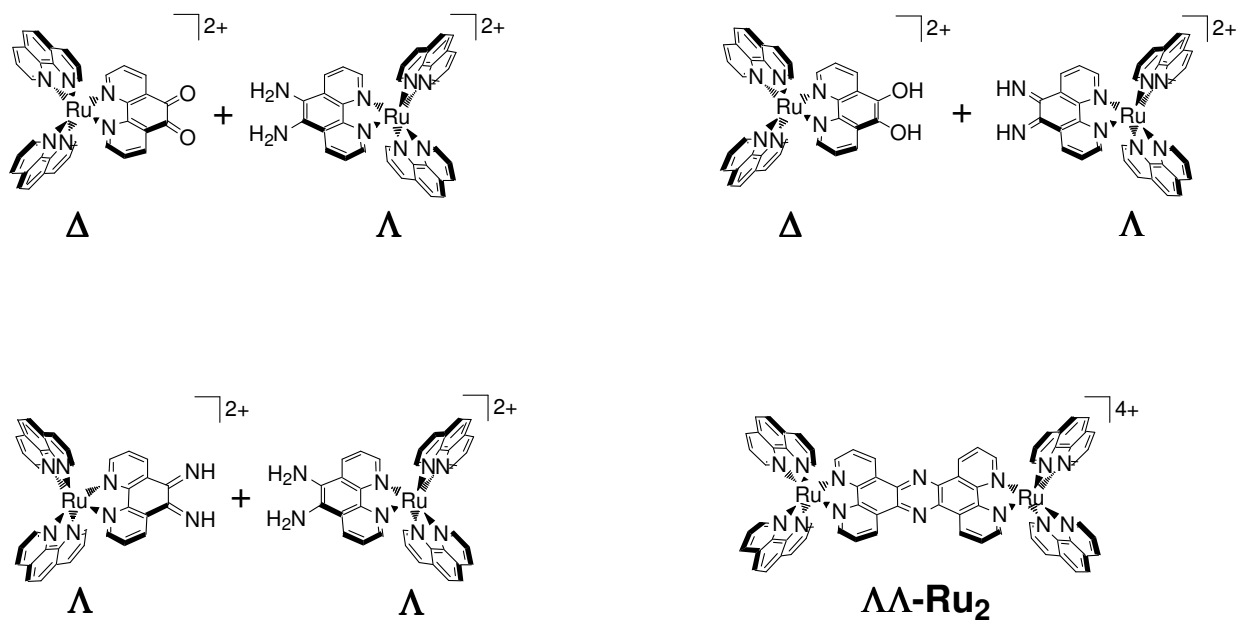


Figure 2.5 Redox side reaction showing diimine formation (top) and diimine/diamine coupling to form **Ru₂** (bottom).

2.3.2 Synthesis of Meso Ru₂

Several different strategies were employed in efforts to minimize this side reaction, but ultimately it was found that a simple modification of the reaction solvent proved most effective. Addition of acetic acid to the solvent sufficiently inhibited the redox side reaction resulting in a reduction of the formation of the unwanted homochiral impurity. As shown in Figure 2.6, the circular dichroism spectra revealed the presence of only 5% of the homochiral contaminant. This improvement was considered satisfactory and allowed continuation and completion of the hexamer synthesis.

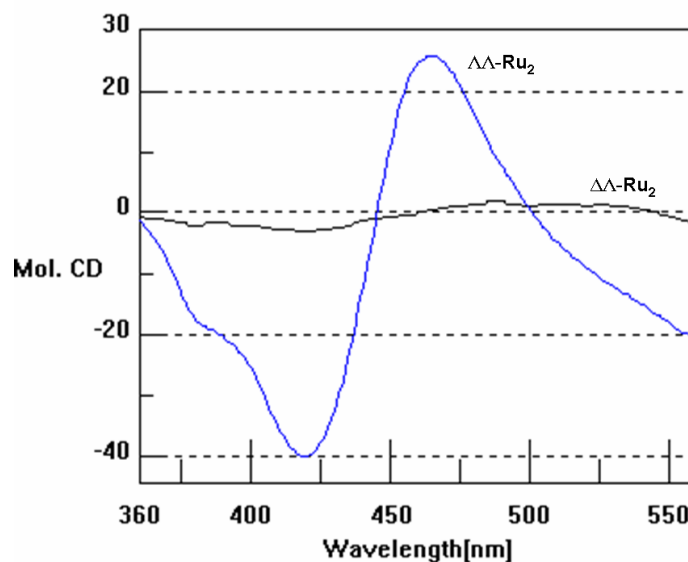


Figure 2.6 Partial circular dichroism spectra of $\Delta\Delta\text{-Ru}_2$ and $\Delta\Lambda\text{-Ru}_2$ (made in the presence of HOAc) in MeCN.

2.4 Hexamer Tertiary and Quaternary Structure

2.4.1 Tertiary Structure of Hexamer

The significance of the successful synthesis of the meso $\Delta\Lambda\text{-Ru}_2$ is that it provides the resulting hexamer with an additional unique tertiary structure. As shown in Figure 2.7, the hexamer can exhibit a total of three different global shapes. These structures were determined from crystallographic data for the $[\text{Ru}(\text{phen})_3][\text{PF}_6]^{2+}$ building block and molecular modeling.^{13,28} Depending on the chirality (primary structure) specifically at the dimer core from which each complex extends, the three-dimensional shape of the molecule can either be twisted (72° right or left) or planar.

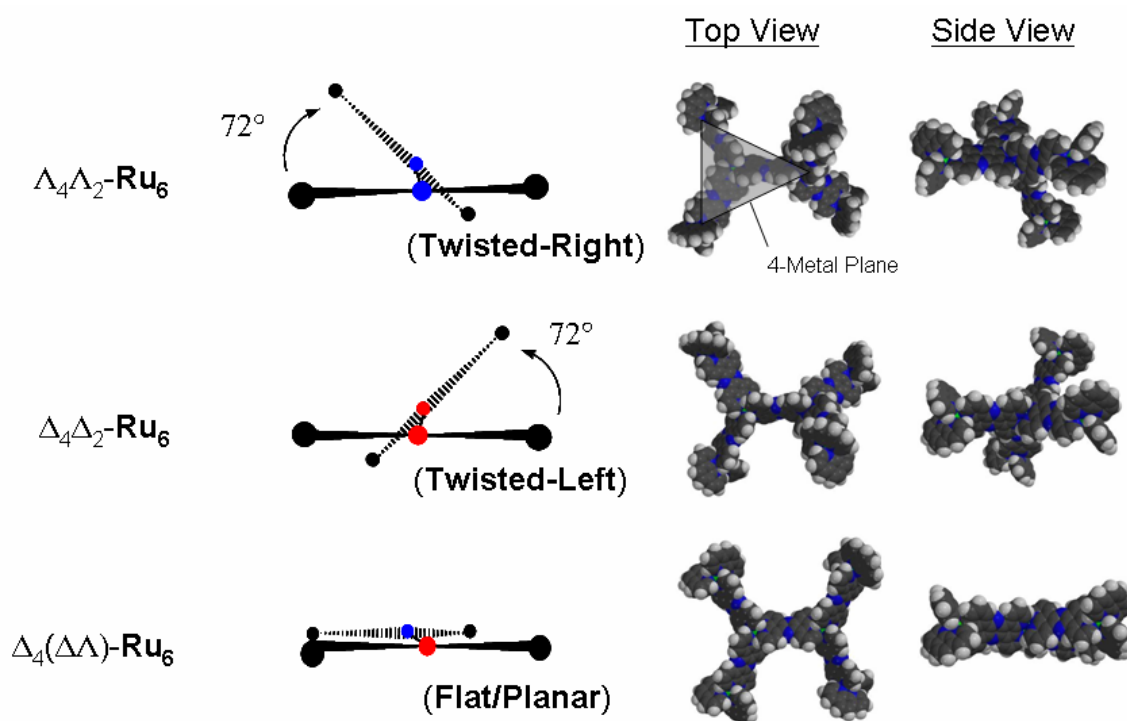


Figure 2.7 Tertiary structures of Ru_6 containing dimer cores of $\Lambda\Lambda$ (top), $\Delta\Delta$ (middle), and $\Delta\Lambda$ (bottom).

These differences directly arise from the spatial positioning of the peripheral phenanthrolines of the central dimers. When each dimer is viewed along the Ru-Ru axis as in Figure 2.8, we observe that when the Ru stereocenters are heterochiral ($\Delta\Lambda$) the terminal phenanthroline rings are eclipsed. However, for the homochiral dimer, the front and back phenanthroline rings are staggered. Since these phenanthroline units are the attachment points (via oxidation and diamine addition) for the additional stereocenters, this conformation is maintained upon synthesis of the hexamer. In essence, the shape is a summation of the chirality at the core, where $\Delta\Delta$ (or $\Lambda\Lambda$) building blocks constructively add to generate the overall twist. The 72° torsional angle nicely illustrates this concept, for the pitch angle of each phenanthroline relative to the

$[\text{Ru}(\text{phen})_3]^{2+}$ C_3 axis is 36° . In the meso case, the chirality of the Δ and Λ building blocks cancel out and the overall **Ru**₆ shape is planar.

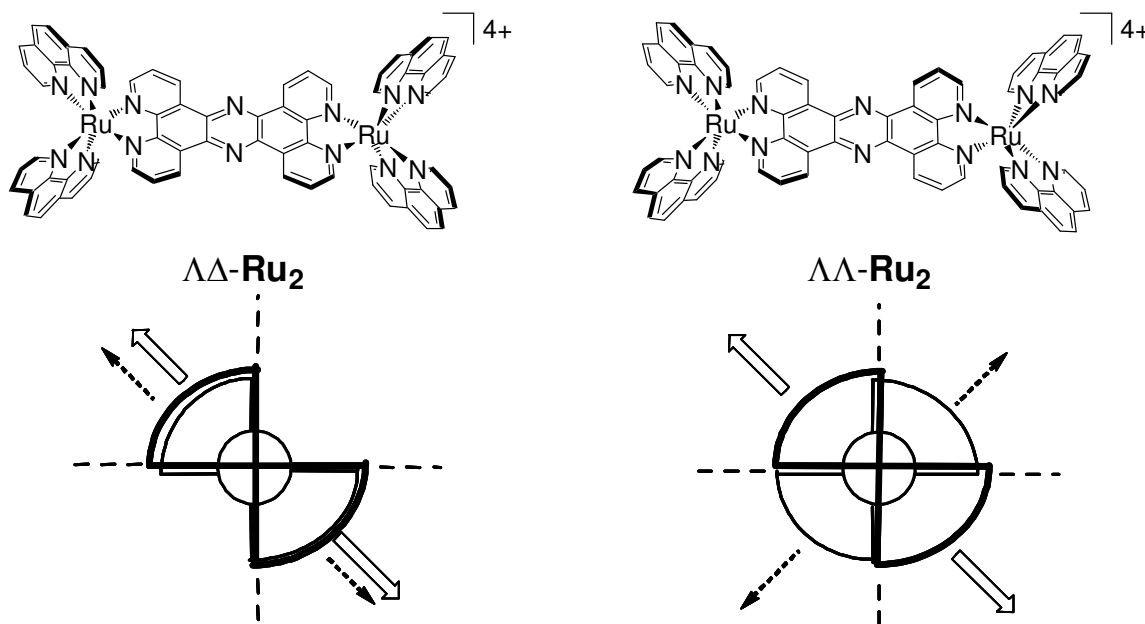


Figure 2.8 Newman projections of **Ru**₂ showing chirality-dependent eclipsed or staggered peripheral phenanthrolines.

Interestingly, this mechanism of summation and cancellation of the chirality of the building blocks manifests itself in the circular dichroism spectra of these complexes as well. A comparative plot of the CD spectra is shown in Figure 2.9. The magnitude of the CD spectra in the MLCT region (420-480 nm) is approximately proportional to the number of individual chromophores in enantiomeric excess within each structure. For the homochiral isomer, $(\Lambda_4\Lambda_2)$ -**Ru**₆, an intense molar CD of +117 (477 nm, MeCN) is observed, which is roughly a 6-fold increase of the molar CD of Λ - $[\text{Ru}(\text{phen})_3]^{2+}$ (+21 at 471 nm in MeCN). This phenomenon was also observed with $\Delta_4\Lambda_2$ -**Ru**₆ and $\Lambda_4\Delta_2$ -

Ru_6 . The net enantiomeric excess of these complexes is two (e.g., four Δ minus two Λ = two Δ) and the molar CD in the MLCT region are roughly twice of the Λ - $[\text{Ru}(\text{phen})_3]^{2+}$ or Δ - $[\text{Ru}(\text{phen})_3]^{2+}$. The newly-synthesized planar hexamer ($\Lambda_4(\Delta\Delta)$ -**Ru₆**) continues this trend with a molar CD of approximately +75 (470 nm, MeCN), roughly equal to a 4-fold increase of the molar CD of Λ - $[\text{Ru}(\text{phen})_3]^{2+}$.

The enantiomers chosen in the final synthetic step do not affect the tertiary structure. Although $\Delta_4\Delta_2$ -**Ru₆** and $\Lambda_4\Delta_2$ -**Ru₆** have different primary structures, their overall shapes are essentially identical with a left twisted conformation. While the peripheral phenanthroline ligands are oriented in different directions (analogous to four conjoined **Ru₂** units), this does not affect the topology of the complex. However, these differences would certainly affect the tertiary structure of a larger, theoretical complex containing 14 Ru centers.

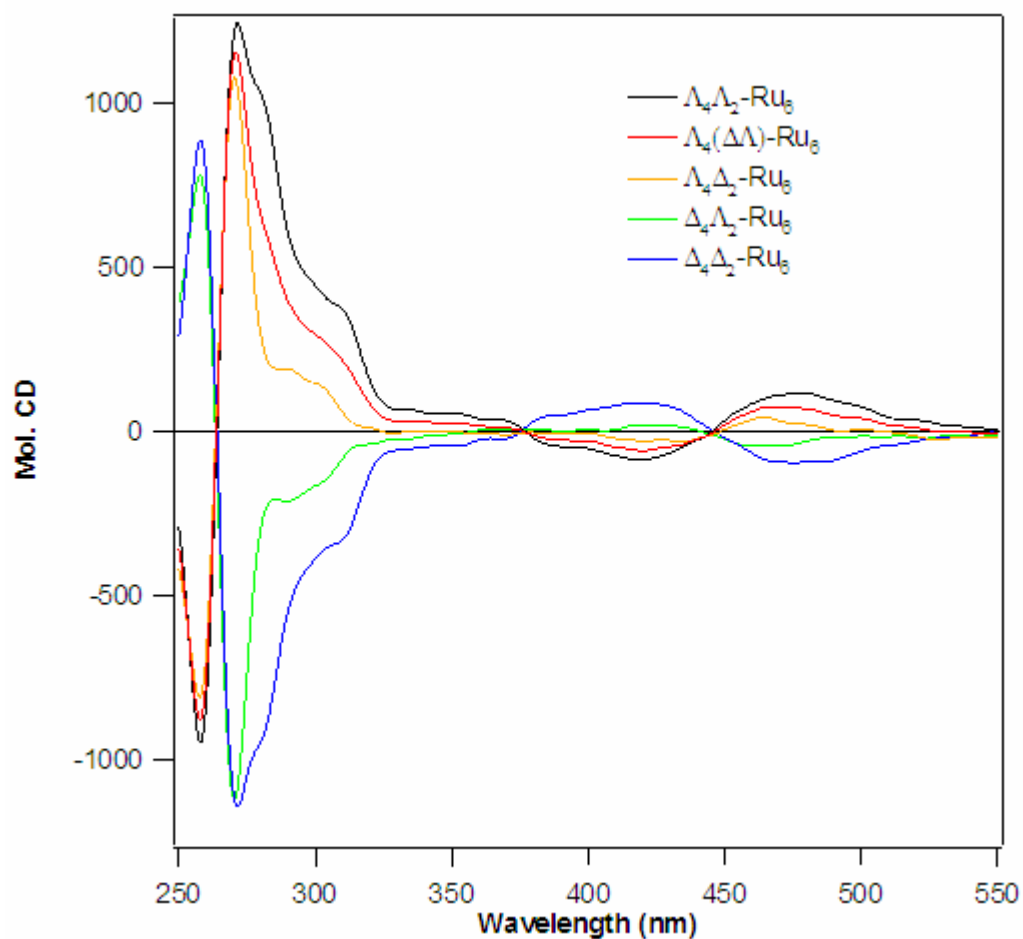


Figure 2.9 Molar Circular Dichroism Spectra of **Ru₆** Complexes.

2.4.2 Quaternary Structure of Hexamer

As discussed in Chapter 1, previous experiments performed on the decamer revealed the effects of tertiary structure on their quaternary assembly.¹³ These experiments have now been repeated for the hexamer, further demonstrating the presence of quaternary structure in this system.

Aqueous solutions of the chloride salts of $\Lambda_4(\Delta\Lambda)$ -**Ru₆** and $\Lambda_4\Lambda_2$ -**Ru₆** were examined using electric birefringence which provides a measure of the degree to which

the colloidal molecules are perturbed by an electric field. As shown in Figure 2.10, the responses were remarkably different, yet echo the behavior observed in the decamer experiments. After the electric pulse begins, the planar ($\Lambda_4(\Delta\Lambda)$ -**Ru**₆) isomer quickly (~0.5 ms) aligns with the electric field. At the end of the 3 ms pulse, the relaxation time is similarly fast. However, the twisted ($\Lambda_4\Lambda_2$ -**Ru**₆) isomer exhibits much slower alignment/relaxation periods whereby the signal does not return to the ground state during the measurement window. (However, the fact that the measurement was reproducible indicates complete relaxation does occur, on the order of seconds).

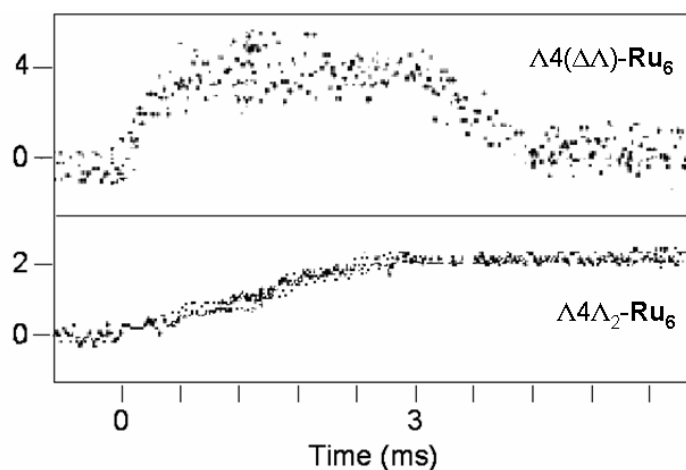


Figure 2.10 Plot of electric field-induced birefringence signals of $\Lambda_4(\Delta\Lambda)$ -**Ru**₆ (top) and $\Lambda_4\Lambda_2$ -**Ru**₆ (bottom). ($E = 6.4 \text{ kV cm}^{-1}$, pulse length = 3 ms.)

The sluggish response of $\Lambda_4\Lambda_2$ -**Ru**₆ suggests that the aggregate may be more ordered than that of the planar $\Lambda_4(\Delta\Lambda)$ -**Ru**₆ complex. It appears to be both harder to perturb and more difficult to reassemble. This may be a result of the twisted shape allowing a more-favorable (or stronger) interlocking-type interaction. The complexity of the aggregate of the planar species appears to be comparatively low since it is able to quickly reform after the electric pulse.

These data show that there is a distinct difference in the aggregate structures of these hexamers. Since the hexamer is the smallest polynuclear species of ours to exhibit tertiary structure, this is a clear indication of its importance. The colloidal structure of these complexes depends dramatically on their tertiary structure. By selecting the primary structure of each complex during synthesis, we can tune the structure of the complex up to the quaternary level.

2.5 Summary and Conclusion

With the study on the hexamer, we now have a complete picture of the hierarchical structure of this abiotic set of robust nanostructures. Beginning with the primary structure (the stereochemical sequence), it is possible to synthesize precisely defined nanostructures with specific global topology. Since the aggregate behavior of this hexamer closely matches that of the larger decanuclear complex, we can confidently say that the quaternary arrangement is directly related to the tertiary, molecular shape.

CHAPTER 3

SCANNING TUNNELING MICROSCOPY IMAGING OF RUTHENIUM POLYPYRIDYL COMPLEXES

3.1 Introduction

In the pursuit of new materials and devices, one synthetic strategy is to mimic nature's bottom-up approach via molecular self-assembly. Working within a system of hierarchical assemblies, it is possible to form a variety of nanoscopic complexes. As discussed previously, ruthenium polypyridyl complexes constructed from chiral building blocks exhibit a tendency to aggregate and assemble into larger structures. Earlier studies have focused primarily on the nature of these assemblies in solution, but the properties of the intermolecular interactions in the solid state had not been investigated. To further characterize these complexes, we have employed scanning tunneling microscopy to study the native packing arrangements of several different complexes and ligands on graphite surfaces in the absence of solvent.

Scanning tunneling microscopy (STM) is a suitable technique for imaging molecules on the atomic scale, and allows visualization of the topographical and electronic properties of surfaces. STM is very versatile and in recent years, has been used to successfully image large molecules including carbon nanotubes,²⁹⁻³⁴ DNA,^{35,36} and polycyclic organic molecules.³⁷⁻⁴⁰

While STM has also been used to obtain images of various coordination complexes,⁴¹⁻⁴⁵ there are relatively few examples of ruthenium polypyridyl complexes observed via this technique.⁴⁶⁻⁴⁹ Examples of published STM images of $[\text{Ru}(\text{terpy})(\text{terpy-py})](\text{PF}_6)_2$ and a heptanuclear ruthenium (II) dendritic complex are shown in Figures 3.1 and 3.2. The size and bulkiness of these molecules present a unique set of challenges. The fact that the complexes are not flat and cannot interact with the surface at more than a handful of contact points makes STM imaging very difficult under ambient conditions.

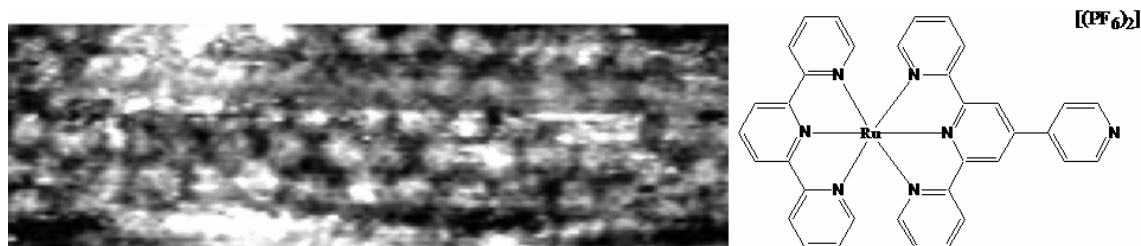


Figure 3.1 14 x 45 nm STM image of a $[\text{Ru}(\text{terpy})(\text{terpy-py})](\text{PF}_6)_2$ monolayer on Pt(100). $I = 30 \text{ pA}$, Bias = 200 mV, constant current mode.⁴⁸

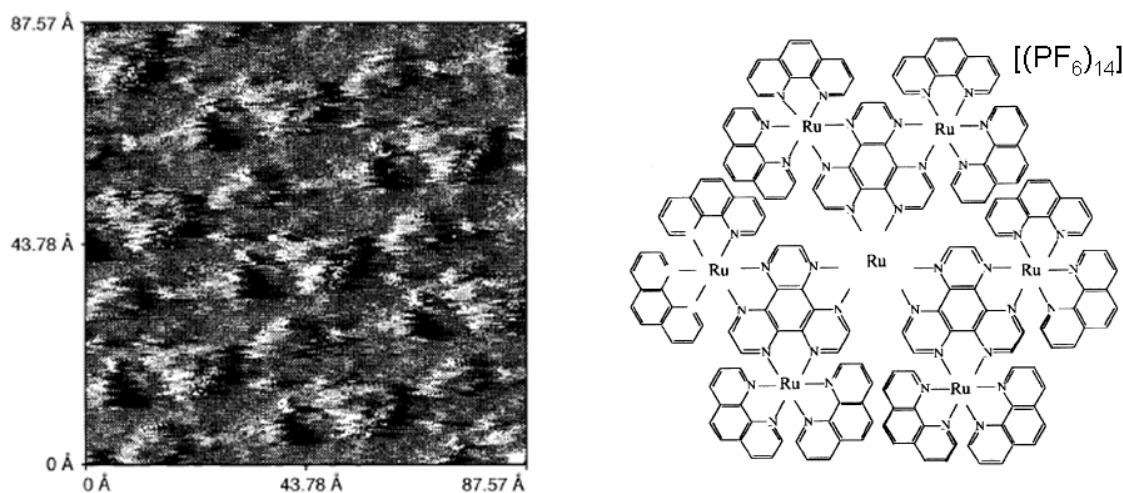


Figure 3.2 90 x 90 Å STM image of an ordered monolayer of Ru_7 on HOPG. $I = 0.5 \text{ nA}$, Bias = -0.55 V, constant height mode.⁴⁷

Herein, we report our attempts to image several different ruthenium polypyridyl complexes as well as their component ligands. Generally, the approach was to minimize tip-sample interactions by keeping the tip as far from the surface as possible. To accomplish this, high bias voltages and low tunneling currents were applied and maintained.

3.2 Experimental

Materials. The compounds tatpp,⁵⁰ [Ru(bpy)₂(pyz)₂](PF₆)₂,⁵¹ [Ru₂(phen)₄(tpphz)](Cl)₄,¹⁹ [Ru₂(phen)₄(tatpp)](CF₃SO₃)₄,⁵⁰ and [Ru₆(phen)₈(tpphz)₅](CF₃SO₃)₁₂⁵² were prepared according to published procedures. All other chemicals and solvents used were of reagent grade and used without further purification.

The CF₃SO₃⁻ salts were prepared from the Cl⁻ salts of their respective complexes. The Cl⁻ salt (0.5 g) was dissolved in H₂O (25 mL). Dropwise addition of a saturated aqueous NH₄CF₃SO₃ solution (5 mL) afforded precipitation of the CF₃SO₃⁻ salt. The precipitate was then isolated via filtration, washed with H₂O and dried *in vacuo* at 60°C for 12 h. Yield: 80%.

The Zn-tatpp adduct was generated by suspending the bridging ligand, tatpp (8 mg), in acetonitrile (5 mL) with Zn(BF₄)₂·xH₂O, x ~ 6.0 – 7.0 (50 mg) in a 10.00 mL volumetric flask. The solution was warmed until the solid completely dissolved and was diluted up to 10.00 mL volume with acetonitrile. After the solution (Z⁴⁺) was prepared, it was filtered through a 0.2 µm filter disk to remove any undissolved solids.

Scanning Tunneling Microscopy. A Digital Instruments (Santa Barbara, CA) Nanoscope E with a picoAmp (pA) boost stage low current converter was used under ambient conditions (room temperature in air). Highly oriented pyrolytic graphite (HOPG) was purchased from SPI Supplies (West Chester, PA) as grade SPI-2. Scanning probes (80% Pt / 20% Ir) were purchased from DI and electrochemically sharpened using a 20% aqueous KCN etching solution. The probe tip was suspended in the etching solution, encircled by a Pt counter electrode. Tips were etched in two stages. First, the tip was submerged 1-2 mm and AC voltage (12 V) was applied for approximately 15 seconds. Secondly, the probe was raised so that only the very tip (< 1 mm) was submerged, and a lower voltage was applied (2-3 V) for a period of approximately 20 seconds. The second step was repeated as necessary to produce a sufficiently sharp probe tip.

Sample Preparation. Films of Zn-tatpp were prepared electrochemically by repetitive potential cycling HOPG in 120 μM tatpp and 1.0 mM $\text{Zn}(\text{BF}_4)_2$ with 0.15 M TBAPF_6 in CH_3CN . Approximately 15 to 20 cycles were completed in the 0.5 to -0.8 V vs. Ag/AgCl potential window at a scan rate of 0.1 V/s.

STM samples of the ruthenium complexes were prepared from either MeCN for complex salts with PF_6^- and CF_3SO_3^- counterions or methanol solutions for complex salts with Cl^- counterions. The complex concentration was between 100 and 200 μM . Just prior to using, the solution was filtered through a 0.1 μm filter and one drop was applied to the freshly cleaved HOPG surface. The samples were allowed to dry slowly

in the presence of either MeCN or MeOH vapor in a covered Petri dish. Once dry, the samples were imaged immediately.

3.3 Results and Discussion

3.3.1 Tatpp Bridging Ligand

Prior to examining the ruthenium complexes, we decided to examine the tatpp ligand. Related aromatic heterocycles such as pyridine,⁵³ pyrazine,⁵³ triazine,⁵³ bipyridine,⁵⁴ and phenanthroline⁵⁵ have successfully been imaged using STM, providing a detailed glimpse into their surface organization. Generally, these molecules tend to stand vertically or tilted with their nitrogen atoms oriented towards the surface of the substrate. The individual molecules are observed to align into parallel chains, forming two-dimensional lattices.

In the absence of bulky Ru-phenanthroline endgroups, we anticipated that tatpp would either lie flat and provide clearly-defined images or stand on one end such that two of the pyridyl nitrogens could maximally interact with the HOPG. Unfortunately, tatpp is insoluble in all common solvents and could not be examined in its 'native' state. Complexation of tatpp with Zn^{2+} forms a soluble adduct (Zn^{2+} -tatpp) as described in the experimental section. The exact formulation of this adduct is unknown but it is presumed that both ends are complexed as excess Zn^{2+} is present and required to completely dissolve the tatpp. We therefore postulate that the adduct is a dinuclear zinc complex of the formula, $[\text{L}_n\text{Zn}(\text{tatpp})\text{ZnL}_n]^{4+}$ (Z^{4+}) where L_n are a combination of solvent and water ligands. The presence of a small amount of water (<1% v/v) is required to form a soluble species. This further complicates the resulting complex

formulation as the resulting aquo complexes could easily deprotonate to form hydroxo complexes with smaller overall charge. It suffices to say that this Zn-tatpp adduct, which we refer to as \mathbf{Z}^{4+} , brings the tatpp ligand into solution and polymeric chains of Zn and tatpp are unlikely under these conditions of a large molar excess of Zn^{2+} .

Ordered thin films of \mathbf{Z}^{4+} (as the BF_4 salt) could be obtained by electrochemical deposition onto the surface of an HOPG substrate. Interestingly, the film that is formed has a deep blue color and demonstrates electrochromic behavior showing blue and yellow color in the reduced and oxidized states, respectively. If the blue film is removed from the electrochemical cell, it slowly degrades to a yellow color (1-2 days), presumably by air oxidation. Notably, there is a marked difference in conductivity between the blue and yellow films. The yellow film was nonconductive and could not be imaged using STM.

STM images of the blue film show well-organized assemblies on the surface of HOPG and two contrasting regions of the surface are shown in Figures 3.3 and 3.4. In both images, we observe bright, oblong spots with an average length of 1.8 nm. We propose that these bright spots correspond to one \mathbf{Z}^{4+} complex, as these dimensions are very close to the theoretical value of 1.75 nm for the length of the tatpp ligand. Proposed unit cells for the imaged regions are indicated in Figures 3.3 and 3.4. In Figure 3.3, the lateral distance between adjacent molecules (a) is 1.2 nm while the distance between stacks (b) is 1.7 nm. The α angle is measured to be 40° . For Figure 3.4, the value of a is larger at 1.7 nm indicating increased intermolecular spacing. The b distance is 1.5 nm which is slightly smaller than that of the arrangement in Figure 3.3

which we attribute to thermal drift in the slow direction. The α angle is measured to be 50° .

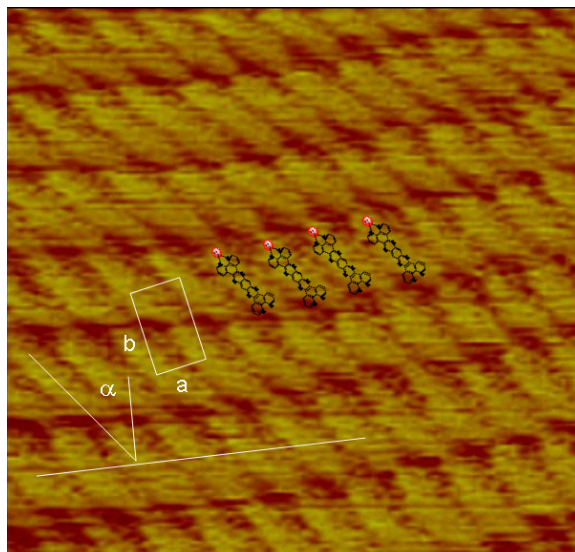


Figure 3.3 15 nm x 15 nm STM image of electrochemically assisted self-assembly of a Zn-tatpp complex on HOPG with a dense packing arrangement. $I = 2.0$ nA, Bias = 700.0 mV, constant height mode.

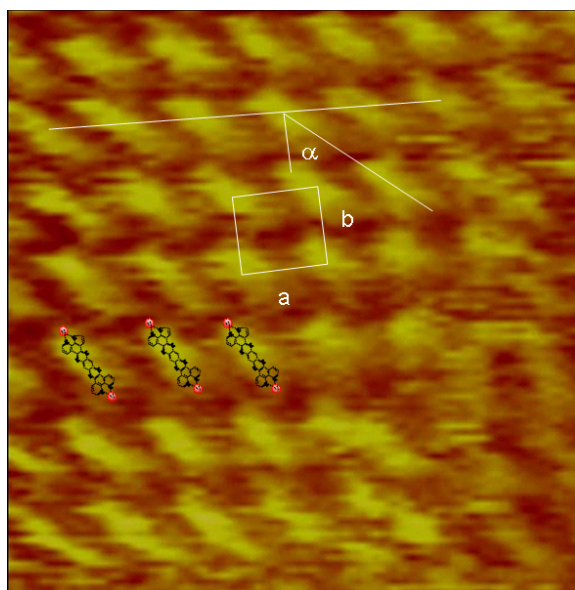


Figure 3.4 12 nm x 12 nm STM image of electrochemically assisted self-assembly of a Zn-tatpp complex on HOPG with a loose packing arrangement. $I = 2.0$ nA, Bias = 700.0 mV, constant height mode.

The packing arrangement in Figure 3.3 shows long columns of tatpp which are tilted at an angle of 40 degrees relative to the column axis. These tatpp ligands are closely packed and the columns are in register such that tatpp's line up across columns. The other surface configuration, shown in Figure 3.4, is similar in that again columns are formed with a slightly larger tilt angle, however this time there is a larger gap between tatpp ligands in a column.

The reasons for these two surface packing modes are not clear. We note that the Z^{4+} complex has both labile and deprotonatable ligands and differences in coordination sphere and/or charge could lead to the observed difference in surface structures. In both cases, however, it is apparent that the tatpp ligand lies on its side (along its long axis). While the resolution is insufficient to draw definite conclusions, it appears that the bright spots in Figure 3.4 are wider than those observed in Figure 3.3 and thus the tatpp ligands in the former image may be lying flat on the surface. In Figure 3.3, the tatpp ligands appear to form a more tightly packed array, as evidenced by the smaller a value of the unit cell.

The UV-Vis absorption spectrum of this blue film (formed on a transparent conductive oxide (TCO) film on a glass substrate) is shown in Figure 3.5. It resembles that of the spectrum obtained after addition of two equivalents of cobaltocene (Figure 3.6); however, a slight shift in energy is observed. This energy shift in the spectrum of Figure 3.5 is attributed to the fact that the Zn-tatpp is bound to the TCO film. The shift in energy indicates that there is only weak electronic interaction between TCO and the Zn-tatpp. This behavior is in fair agreement with the reported slight spectral shift in the

electronic spectra of *cis*-bis(4,4'-dicarboxy-2,2'-bipyridine)-bis(isothiocyanato)ruthenium(II) dye (N3) in solution and bound to TiO₂.⁵⁶

Although there is a small broad peak centered around 450 nm, the most significant spectral feature in Figure 3.5 is the three-peak band centered around 650 nm. Based on comparison to the spectra in Figure 3.6, we believe that the blue film is primarily composed of the doubly reduced complex, with the 450 nm peak due to some incompletely reduced fraction of the sample. General broadening of the solid state absorption spectra in relation to the solution spectra has also been observed in thin films of poly (5,12-dihydro-5,7,12,14-tetraazapentacene),⁵⁷ which is structurally similar to the tatpp ligand.

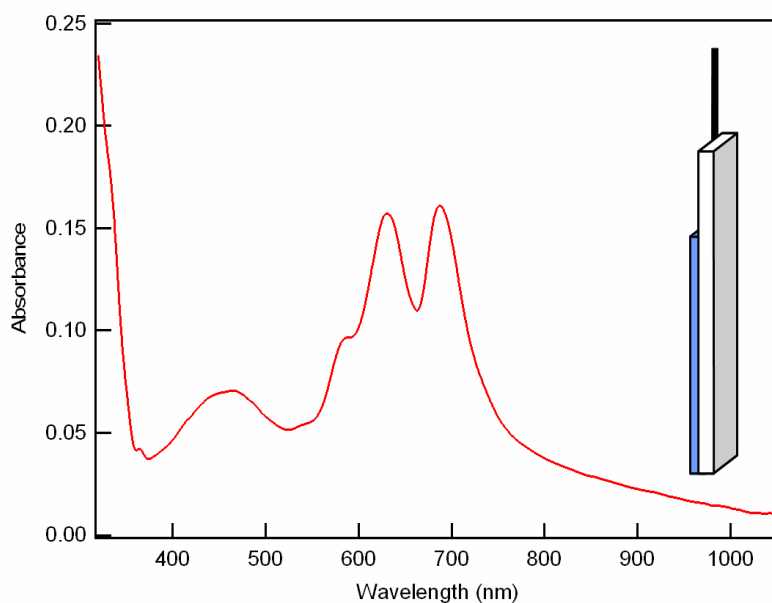


Figure 3.5 UV-Vis absorption spectrum of the blue film formed by potential cycling in 120 μM tatpp(Zn) $_x\text{Y}^+$ with 0.15 M TBAPF₆ in CH₃CN. A sketch of the film on the TCO electrode is also shown.

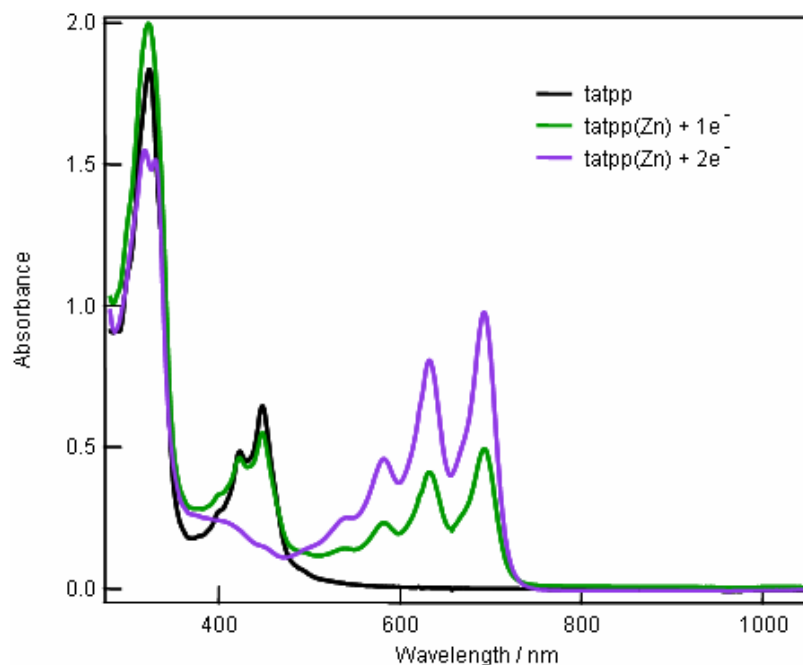


Figure 3.6 UV-Vis absorption spectra of tatpp(Zn) in acetonitrile after adding 1 (—) and 2 (—) equivalents of cobaltocene.

3.3.2 Ruthenium Complexes: Monomers

Much of the published work regarding STM imaging of metal complexes shows that the complexes must have some molecular functionality to adhere to the substrate such that STM imaging under ambient conditions is possible. For example, work by Figgemeier et. al. reveals self-assembled monolayers of $[\text{Ru}(\text{terpy})(\text{terpy-py})]^{2+}$ on a Pt(100) substrate.⁴⁸ Apparently, the pendant 4-pyridyl substituent provides an anchor point between the molecule and the metal surface, which helps to hold the complex in place during scanning. In fact, pendant pyridyl groups have been used to direct the orientation of molecules adsorbed on surfaces. Self-assembled tetranuclear cobalt complexes have been observed by STM in configurations both parallel and orthogonal to an HOPG surface depending on the positions of pyridyl nitrogen atoms in their bipyridyl backbone ligands.⁵⁸

Not surprisingly, our attempts to obtain meaningful STM images of the basic $[\text{Ru}(\text{phenanthroline})_3]^{2+}$ complex proved to be very difficult. In the absence of anchoring functionalities, it seems likely that the STM tip simply pushes the complex around, preventing image acquisition. Even under gentle scanning parameters with high bias and low tunneling current, this complex appeared to be too mobile for imaging under these conditions.

With this in mind, we decided to study a related complex, $[\text{Ru}(\text{bipyridine})_2(\text{pyrazine})_2][\text{PF}_6]_2$ **1**(PF₆)₂ which has two uncoordinated pyrazine nitrogens to provide anchor points to the HOPG. Figure 3.7 shows a 50 nm x 50 nm image of the HOPG showing clusters of **1**(PF₆)₂. At this resolution, individual

molecules are not observed, but the presence of material on the surface is confirmed based on comparison to the bare HOPG shown in Figure 3.8(A).

For comparison, STM images of the bare HOPG substrate are presented in Figure 3.8. The 50 nm x 50 nm scan (A) is relatively featureless, showing the clean surface of the substrate. As the scan size is reduced, the atomic structure of the graphite is revealed. In the 3 nm x 3 nm window of Figure 3.5(C), the honeycomb, hexagonal symmetry can be observed. The C-C bond distance can be measured and matches the expected value of 1.4 Å.

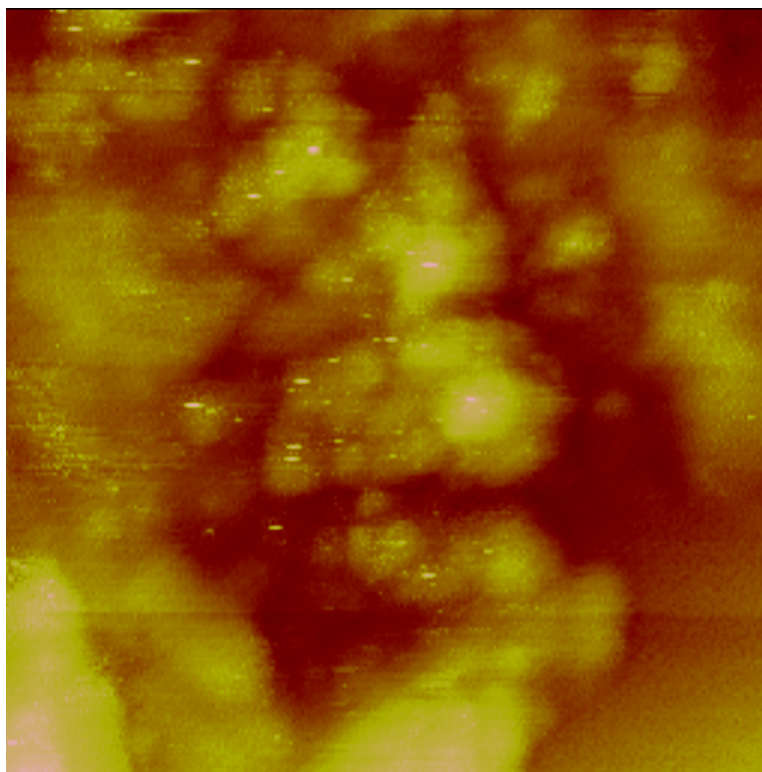


Figure 3.7 A 50 nm x 50 nm STM image of $\mathbf{1(PF_6)_2}$ on HOPG. $I = 1.0$ pA, Bias = 500.0 mV, constant current mode.

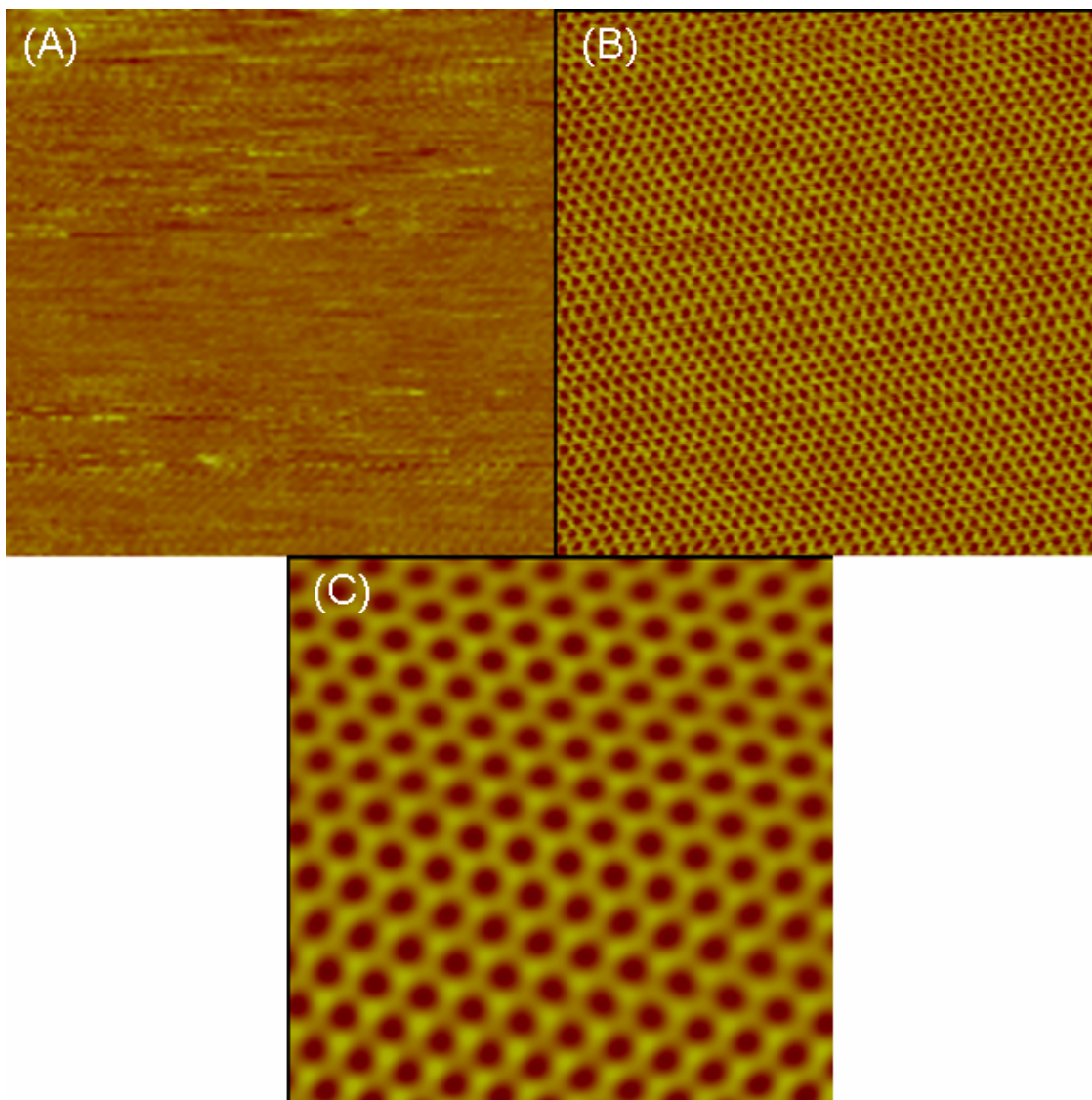


Figure 3.8 STM images of HOPG at (A) 50 nm x 50 nm, $I = 1.0$ nA, Bias = 200.0 mV, constant height mode; (B) 10 nm x 10 nm, $I = 1.5$ nA, Bias = 80.0 mV, constant height mode; and (C) 3 nm x 3 nm, $I = 3.0$ nA, Bias = 20.0 mV, constant height mode.

A different region of the surface is shown in Figure 3.9. In this image we observe a row of bright, circular spots which appears to be a molecular-resolution image of the complex. The diameter of each spot is approximately 1.0 nm which closely matches the anticipated size of one $1(\text{PF}_6)_2$ molecule. The appearance of the molecules as bright circular spots is consistent with the published image of $[\text{Ru}(\text{terpy})(\text{terpy-py})]^{2+}$ (Figure 3.1). Unfortunately, since only one row of molecules is visible in the image, it is difficult to draw conclusions regarding its two-dimensional packing behavior.

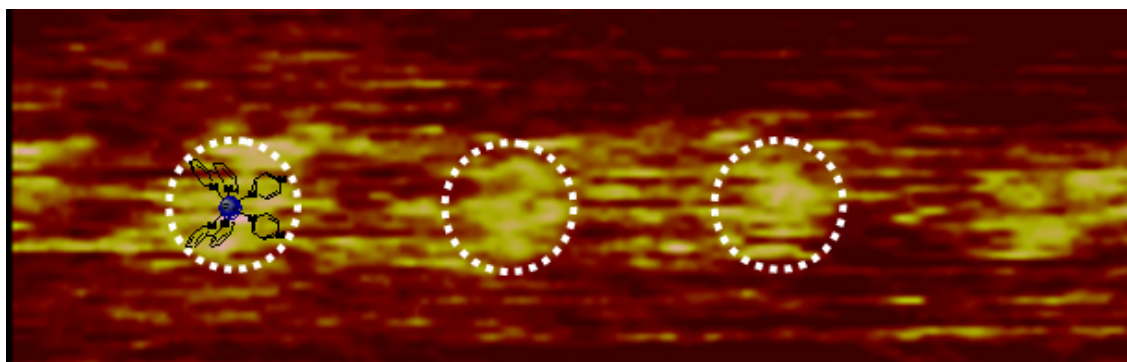


Figure 3.9 8.75 nm x 2.75 nm STM image of $1(\text{PF}_6)_2$ on HOPG. $I = 1.0$ pA, Bias = 77.38 mV, constant current mode.

3.3.3 Ruthenium Complexes: Dimers

We found that moving to larger complexes allowed for successful imaging without the need for surface-tethering functionality. Presumably, this is simply a result of the larger complexes having more surface interactions and therefore being less sensitive to interactions from the scanning probe. In fact, as mentioned previously, Latterini et. al. were able to image a dendritic heptamer on HOPG without modification.⁴⁷

Initially, we looked at $[\text{Ru}_2(\text{phen})_4\text{tpphz}](\text{Cl})_4$ [$\mathbf{2}^{4+}$] which is shown in Figure 3.10. In Figure 3.11 we can clearly see a domain boundary signifying the edge of a region where the $\mathbf{2}^{4+}$ molecules have self-assembled into an ordered pattern. The width of each bright line is approximately 1.2 - 1.5 nm which agrees with the calculated width of $\mathbf{2}^{4+}$ (1.3 nm between metal centers). This image suggests that the preferred packing arrangement for this complex is an ordered pattern in which the molecules line up along their bridging ligand into long columns.

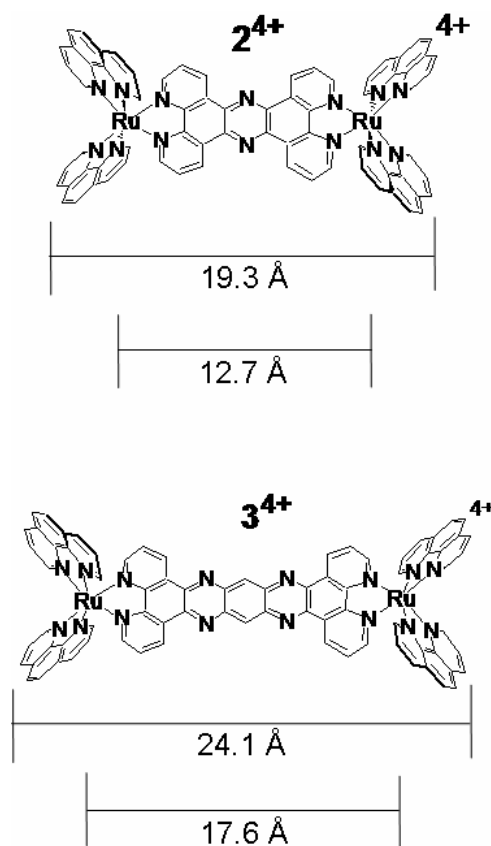


Figure 3.10 Complexes $[\text{Ru}_2(\text{phen})_4\text{tpphz}]^{4+}$ [$\mathbf{2}^{4+}$] and $[\text{Ru}_2(\text{phen})_4\text{tatpp}]^{4+}$ [$\mathbf{3}^{4+}$].

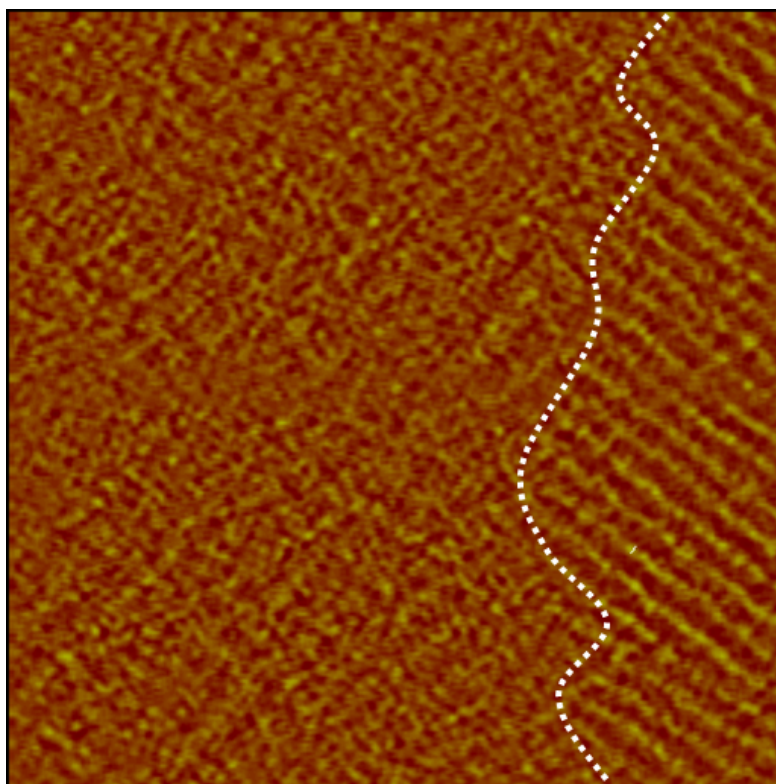


Figure 3.11 100 nm x 100 nm image of $[2(\text{Cl})_4]$ on HOPG showing a domain boundary.
 $I = 1.0 \text{ pA}$, Bias = 200.0 mV, constant current mode.

While scanning, the sample was magnified and an image was collected in the 50 nm square window shown in Figure 3.12. ChemDraw figures of **2** have been superimposed on the image to indicate the scale of the observed features. As expected, the apparent width of each column increased, but the measured width remained constant at about 1.5 nm. This provided confirmation that the observed image was real and not an artifact due to noise or interference. The distance between columns is quite uniform with an average width of 1.8 nm. Unfortunately, the quality of the image is not sufficient to achieve molecular resolution. As a result, the columns of molecules appear as continuous bands and it is not possible to measure the vertical distance between

molecules. Upon further magnification, the tip-sample interactions prevented imaging at higher resolution.

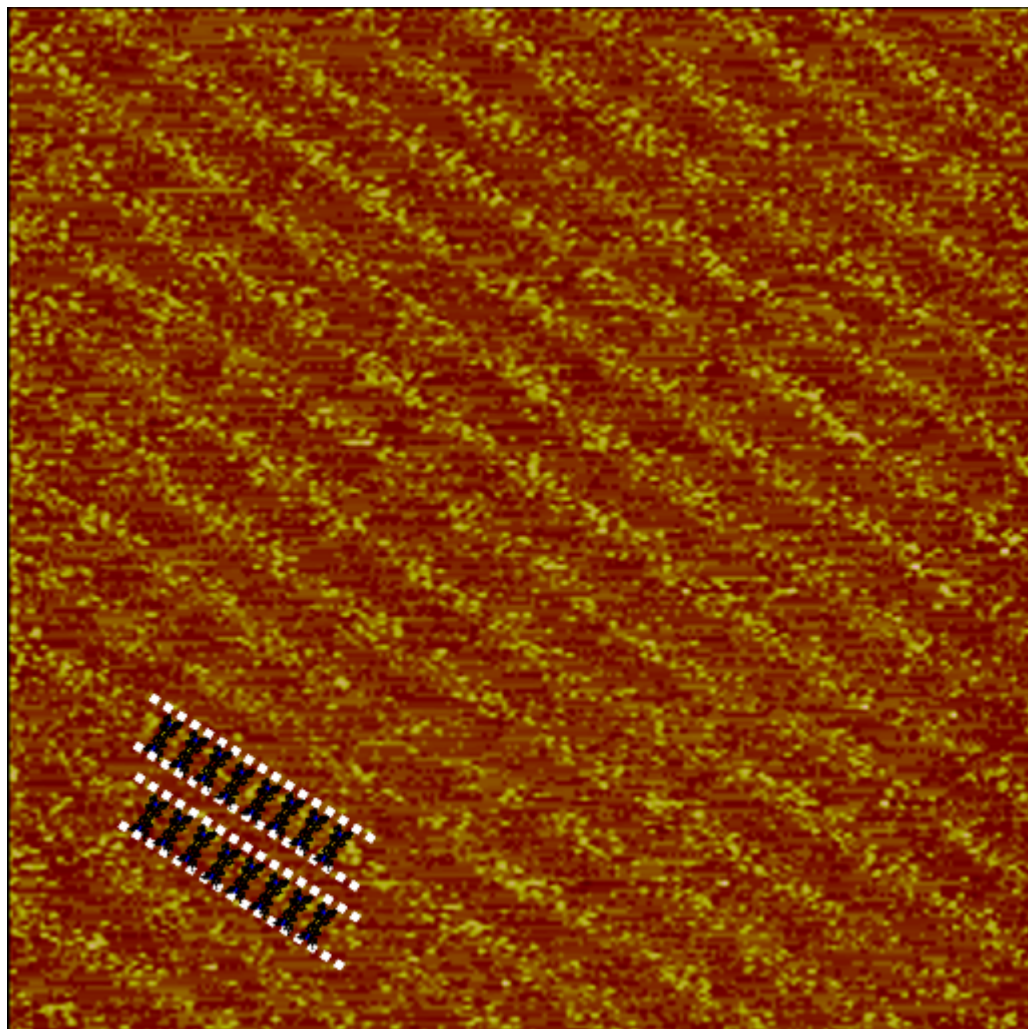


Figure 3.12 50 nm x 50 nm image of $[2(\text{Cl})_4]$ on HOPG. $I = 5.0$ pA, Bias = 500.0 mV, constant current mode. Molecular models indicate scale only, not packing density.

Imaging of the complex $[\text{Ru}_2(\text{phen})_4\text{tatpp}](\text{CF}_3\text{SO}_3)_4$ $[\mathbf{3}(\text{CF}_3\text{SO}_3)_4]$ (Figure 3.10) proved much more successful. Figure 3.13 shows a 23 nm x 10 nm scan of $\mathbf{3}(\text{CF}_3\text{SO}_3)_4$ on HOPG. The general self-assembled behavior of these complexes is consistent with that for $\mathbf{2}(\text{Cl})_4$ in that we observe bright bands with a measured width of 1.7 - 2.0 nm, where the theoretical width of complex $\mathbf{3}^{4+}$ is 1.8 nm (between metal centers). This result suggests that $\mathbf{3}^{4+}$ also arranges into columns stacked along the central bridging ligand. Unfortunately, some streaking is evident in the image in the fast-scanning direction. This is due to molecular motion occurring on the time scale of imaging. The reason for the alternating light and dark bands is unknown but one possibility is that this is where the anions reside and being much smaller and more mobile species, these remain unresolved.

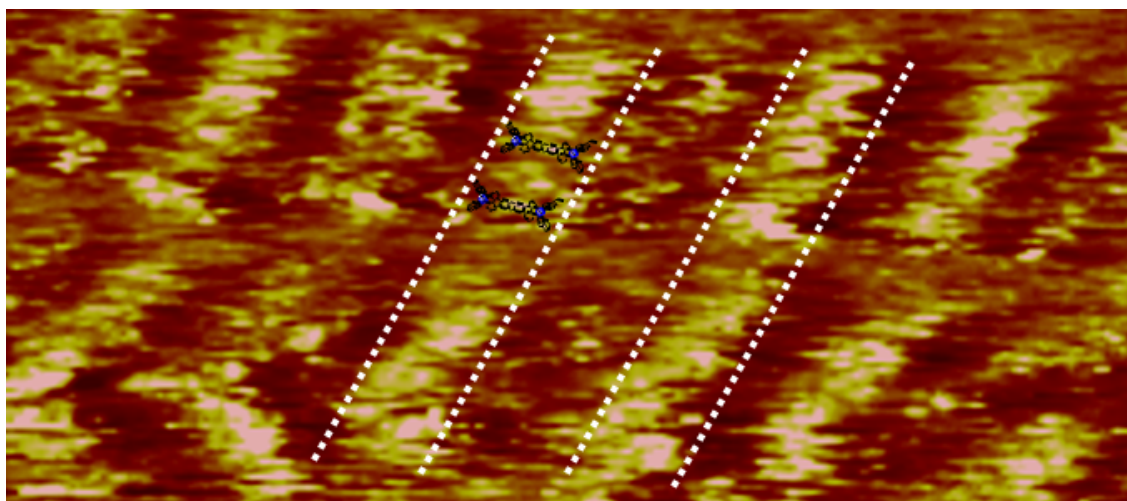


Figure 3.13 23 nm x 10 nm image of $[\mathbf{3}(\text{CF}_3\text{SO}_3)_4]$ on HOPG. $I = 50.0$ pA, Bias = 750.0 mV, constant height mode.

Notably, we were able to obtain molecular-resolution images of this complex as shown in Figures 3.14 and 3.15. At this scale, we can clearly see stacks of “dumbbell-shaped” molecules, just as we would expect for complex 3^{4+} . The bright spots at the ends of each “dumbbell” are 1.8 nm apart (measured from each center), exactly matching the expected value. We observe a much closer packing within each stack than between adjacent columns. The average horizontal spacing between molecules is measured to be 1.1 nm (2.1 nm between metal centers). Vertically, the intermolecular distance is an average of about 0.2 nm (1.2 nm between metal centers).

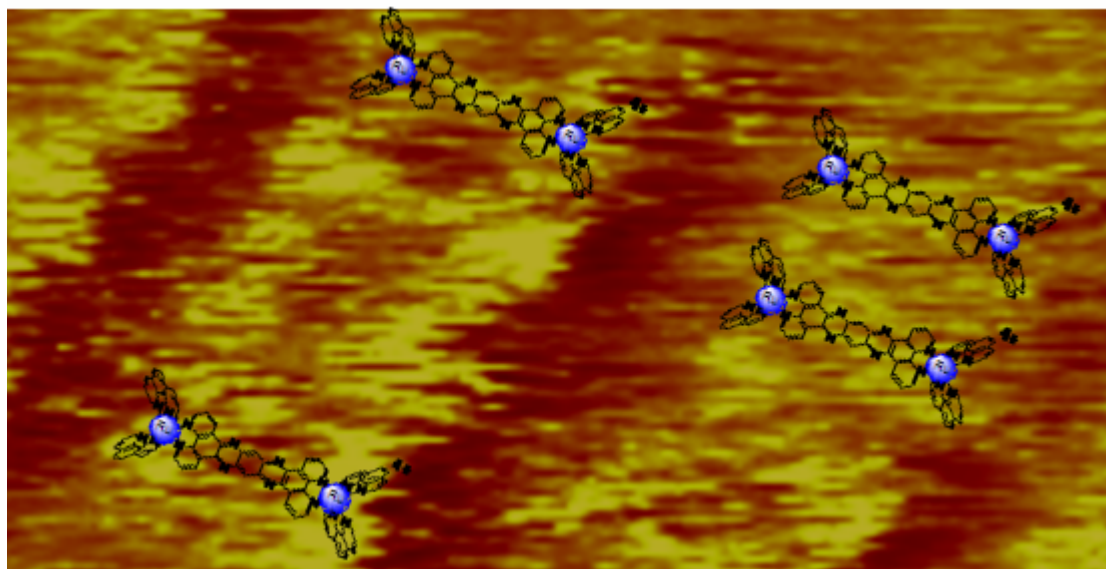


Figure 3.14 STM image of $[2(\text{CF}_3\text{SO}_3)_4]$ on HOPG. 2-D Surface plot, 11 x 5 nm, $I = 64$ pA, Bias = 750 mV.

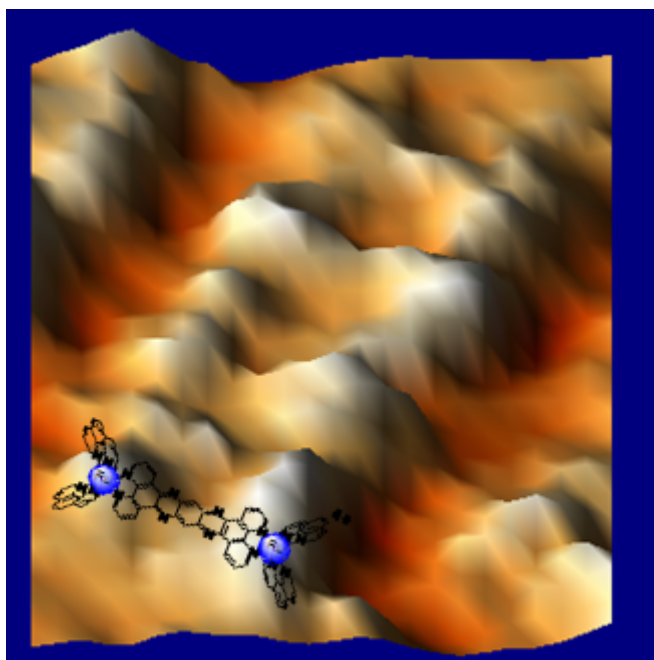


Figure 3.15 3-D Contour plot of $[2(\text{CF}_3\text{SO}_3)_4]$ on HOPG 5 x 5 nm, $I = 64$ pA, Bias = 750 mV.

The images of both 2^{4+} and 3^{4+} demonstrate that these complexes self assemble into columns, aligning along their central bridging ligands. However, the fact that all these columns lie parallel also indicates a preferred orientation with respect to the substrate. The molecules exhibit a preference to be in register with one axis along the hexagonal symmetry of the HOPG surface.

3.3.4 Ruthenium Complexes: Hexamers

Continuing the trend toward larger complexes, we also took images of the hexamer, $[\text{Ru}_6(\text{phen})_8(\text{tpphz})_5](\text{CF}_3\text{SO}_3)_{12}$ $[4(\text{CF}_3\text{SO}_3)_{12}]$ (Figure 3.16). Figure 3.17 shows what appears to be a bundle of columnar stacks of molecules. Within the image, there are a series of light bands, each with a width of 4.5 nm, the approximate diameter of a Ru_6 molecule. Even though these complexes are much larger than 2^{4+} and 3^{4+} , they

continue to demonstrate the linear stacking behavior. In this instance, the stack height is very regular, at about 28-30 nm. Although we were unable to achieve molecular resolution for this sample, we can estimate that each column represents a relatively short stack of complexes. Depending on how closely they are packed, a 30 nm column would be composed of no more than 6 to 10 4^{12+} molecules.

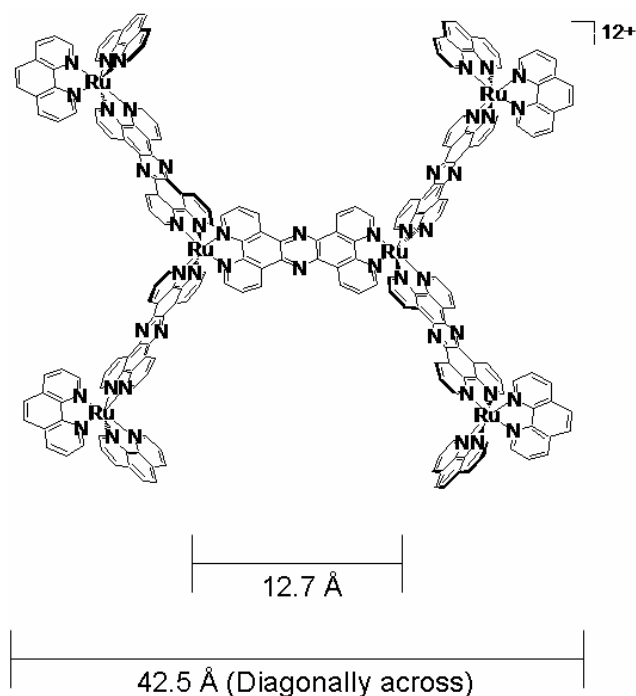


Figure 3.16 $[\text{Ru}_6(\text{phen})_8(\text{tpphz})_5]^{12+} [4]^{12+}$

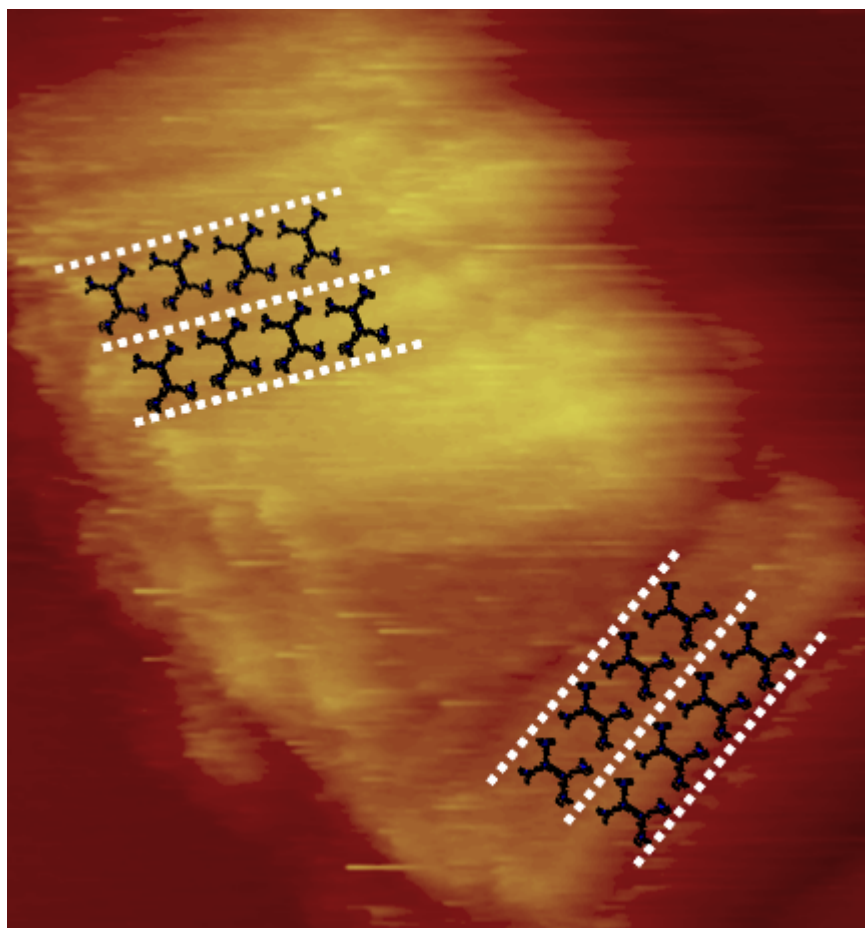


Figure 3.17 56 x 56 nm STM image of $[4(\text{CF}_3\text{SO}_3)_{12}]$ on HOPG. $I = 74.0 \text{ pA}$, Bias = 500.0 mV , constant current mode. Molecular models indicate scale only, not packing density.

In contrast to the images of the dimers, the hexamer stacks do not all align in the same direction with respect to the substrate. As seen in Figure 3.17, stacks are observed oriented in two different directions. This is not surprising, for large molecules are expected to be less susceptible to surface corrugation effects.⁴³

3.4 Summary and Conclusion

In this chapter, we report the first STM images of Zn-tatpp, $[\text{Ru}(\text{phen})_2(\text{pyz})_2]^{2+}$, $[\text{Ru}_2(\text{phen})_4\text{tpphz}]^{4+}$, $[\text{Ru}_2(\text{phen})_4\text{tatpp}]^{4+}$, and $[\text{Ru}_6(\text{phen})_8(\text{tpphz})_5]^{12+}$. Submolecular resolution of $[\text{Ru}_2(\text{phen})_4\text{tatpp}]^{4+}$ was achieved under ambient conditions.

Molecularly resolved images of electrochemically-prepared films of the Zn-tatpp adduct were obtained. These images reveal the presence of regions of different packing densities in the same film. These films could only be imaged in their reduced state. Once oxidized by prolonged exposure to air, the films were no longer conductive and unviewable using STM.

Previous solution studies of these species indicated the presence of aggregates. We suspected that a π - π stacking interaction was driving these complexes to align along their bridging ligands. The STM images of the dimers and hexamers presented here provide visual evidence for the existence of these columns. Considering the fact that these stacks are evident under solventless conditions, we believe that there is even greater potential for achieving long-range ordering with the solubilized species.

CHAPTER 4

ELECTRICAL CONDUCTIVITY

4.1 Introduction

In the world of modern electronics, silicon-based technologies are reaching their theoretical limits. As a result, there has been considerable interest in the idea of utilizing single molecules to construct new electronic devices. Some believe that the next generation of computing technology lies within the field of molecular electronics. Through the design and synthesis of functional nanoscopic molecules and their arrangement into electrical circuits, fundamentally new, high-speed processors may be produced.⁵⁹

The prospect of developing single-molecule electronics began with Aviram and Ratner,⁶⁰ who proposed a device featuring electron transfer between donor and acceptor molecules. This concept inspired a flurry of research into the development of molecular devices, including devices based on bulk organic materials such as soft plastic transistors, dye lasers, and light-emitting diodes.⁶¹ More recently, significant progress has been made in the development of electronic devices based on nanometer-sized molecules such as carbon nanotubes and semiconductor nanowires.^{62,63} In particular, these have drawn interest due to their rigid, robust structures and high conductivity.

However, in the development of electronics on the molecular scale, it will be crucial to find ways to incorporate the energy levels of a single molecule or several molecules.^{64,65} As the miniaturization of microelectronic circuits continues, components of atomic or molecular size will be required. Organic molecules with stable, rigid, well-defined, nanometer-scale structures may be well-suited to fill this role, with the added benefit of being able to tune their energy levels through chemical synthesis.⁶⁶

The range of possibilities for new components and properties constructed from organic molecules is very promising. For example, researchers have established that organic single-molecule (or few-molecule) devices can function as electrical components including diodes,⁶⁷ switches,⁶⁸ and memory.⁶⁹ It has also been shown that single molecules of metal-organic complexes demonstrate a field effect wherein transistor-like behavior is observed when a gate voltage is applied.^{70,71}

Ruthenium polypyridyl complexes may have applications in this area. Their inherent redox^{72,73}, and photophysical^{74,75} properties coupled with chemical stability⁷⁶ and structural rigidity^{52,77} has garnered a great deal of attention. In addition, the polypyridyl ligands used are structurally similar to many of the organic aromatic compounds investigated in this application. In particular, we were interested in the potential applications of the ruthenium dimers, [(phen)₂Ru(tpphz)Ru(phen)₂]⁴⁺ [**1**⁴⁺] and [(phen)₂Ru(tatpp)Ru(phen)₂]⁴⁺ [**2**⁴⁺], as materials for molecular electronics (Figure 4.1). The bridging ligands in these complexes are similar to some well-know organic

molecular electronic materials including pentacene, phenazine and tetraazapentacene.⁷⁸⁻

80

Previous studies have shown that ruthenium polypyridyl complexes can have applications in the field of molecular electronics including molecular wires,^{81,82} electroluminescent devices,⁸³⁻⁸⁵ and field-effect transistors.⁷¹ We suspected these tatpp and tpphz complexes of ruthenium may have unusual properties given the number of interesting components within each complex. In addition, we anticipated that the size of these complexes, particularly the hexamer $[\text{Ru}_6(\text{phen})_8(\text{tpphz})_5]^{12+}$ [**3**¹²⁺] (Figure 4.2) with a diagonal distance of 4.2 nm, would enhance the efficiency of electron transfer due to its ability to bridge larger gaps.

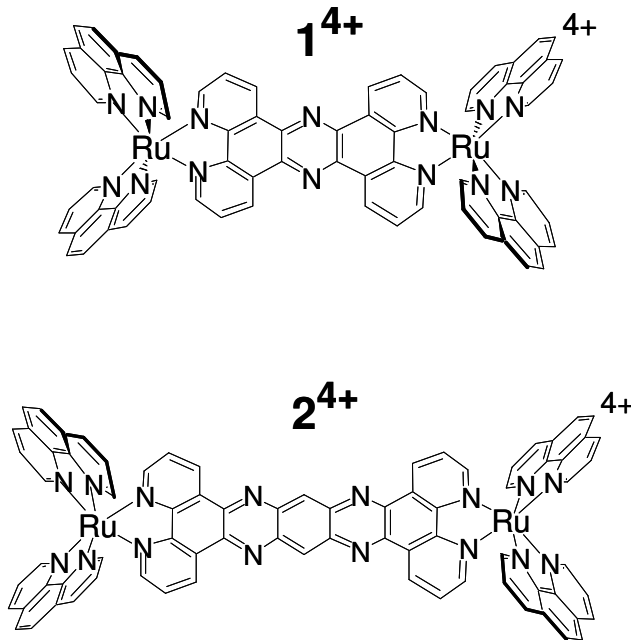


Figure 4.1 Complexes $[\text{Ru}_2(\text{phen})_4\text{tpphz}]^{4+}$ [**1**⁴⁺] and $[\text{Ru}_2(\text{phen})_4\text{tatpp}]^{4+}$ [**2**⁴⁺].

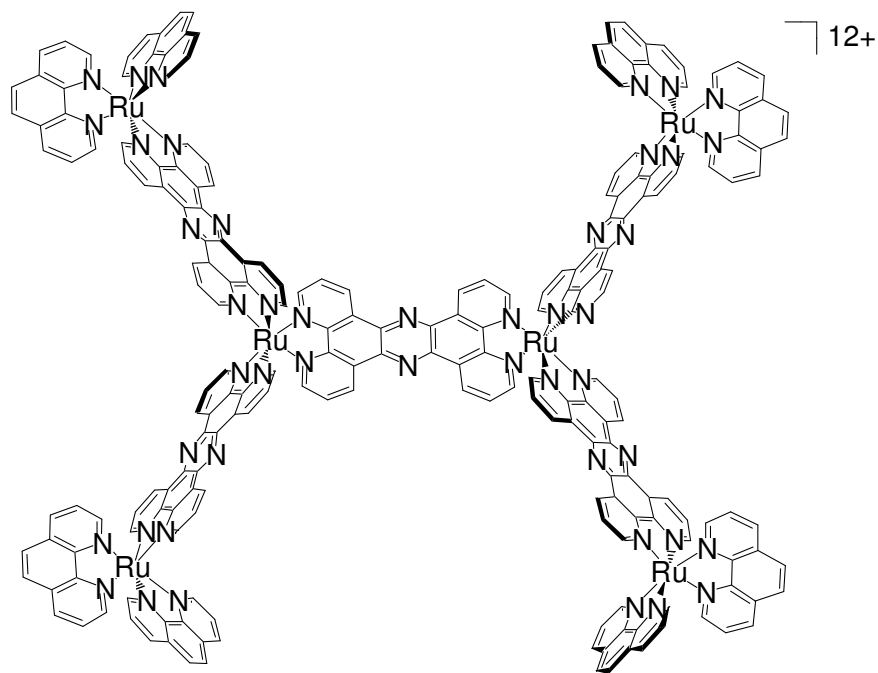


Figure 4.2 $[\text{Ru}_6(\text{phen})_8(\text{tpphz})_5]^{12+}$ [**3**¹²⁺]

Herein we report our efforts to characterize the observed conductivity behavior for thin films of several ruthenium dimers and hexamers bridged by the tpphz and tatpp ligands. The effects of changes to the counterions, temperature, and molecular shape will be discussed.

4.2 Experimental

Materials. The compounds $[\text{Ru}_2(\text{phen})_4\text{tpphz}](\text{Cl})_4$,¹⁹ $[\text{Ru}_2(\text{phen})_4\text{tpphz}](\text{PF}_6)_4$,¹⁹ $[\text{Ru}_2(\text{bpy})_4(\text{oxalato})_2\text{tpphz}]$,⁸⁶ $[\text{Ru}_2(\text{phen})_4\text{tatpp}](\text{Cl})_4$,⁵⁰ and $[\text{Ru}_6(\text{phen})_8(\text{tpphz})_5](\text{Cl})_{12}$ ⁵² were prepared as described previously. All other chemicals and solvents used were of reagent grade and used without further purification.

Sample Preparation. All sample preparation, manipulation, and measurements were carried out in a class 1000 cleanroom. Solutions of ruthenium complexes were prepared with concentrations between 0.1 and 0.5 mM in either MeCN (PF_6^- and CF_3SO_3^- salts) or MeOH (Cl^- salts). Each sample was filtered using a 0.1 μm syringe filter during sample preparation. The thin films were prepared either by applying a drop of solution to the microcontact pad substrate and letting it evaporate or by spin-casting at 2000 rpm for 3 minutes using a Headway Spinner. After film preparation, samples were baked at 100°C for 2 h.

The microcontact pads were constructed on either glass or silicon (with a SiO_2 top layer) substrates and patterned in gold. The contact spacing was 1.0 μm , with a contact width of 5.0 μm (see Figure 4.3).

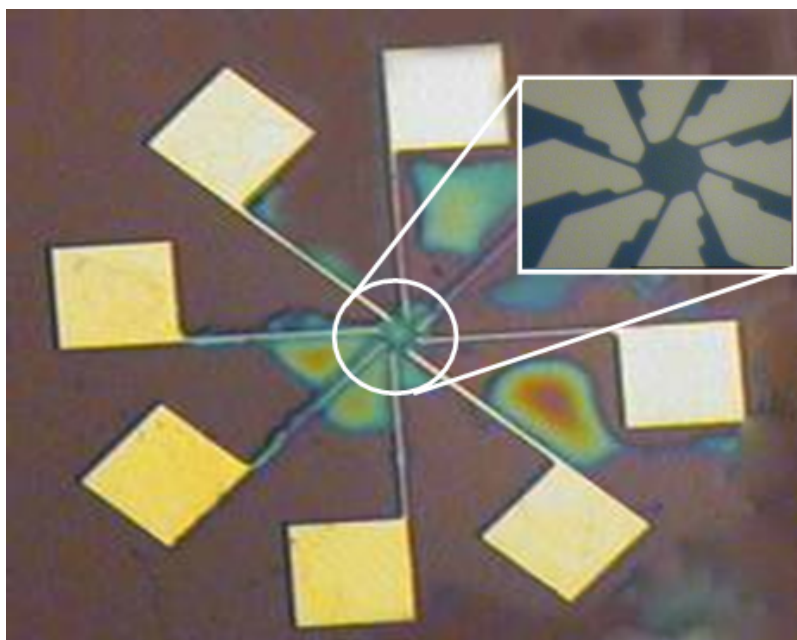


Figure 4.3 Gold microcontact pattern on the silicon substrate. The spacing between pads is 1 μm . An identical pattern on a glass substrate was also used.

Instrumentation. Samples were mounted on a Micromanipulator 6000 probe station. The I-V curves were measured using an HP 4145A Semiconductor Parameter Analyzer.

4.3 Results and Discussion

4.3.1 Conductivity of Ruthenium Polypyridyl Complexes

We have examined the conductive properties of thin films of several ruthenium polypyridyl complexes, studying complexes with different structures, of different sizes, with different counterions and with different overall charge. Assuming that conduction occurs along the shortest distance, we view the conduction as occurring through the material immediately between the two electrode as shown in Figure 4.4. On average, films prepared by the dropcast method had measurable currents on the order of nanoamps (nA) whereas films prepared by the spincoat method showed measurable currents in the picoamp (pA) range.

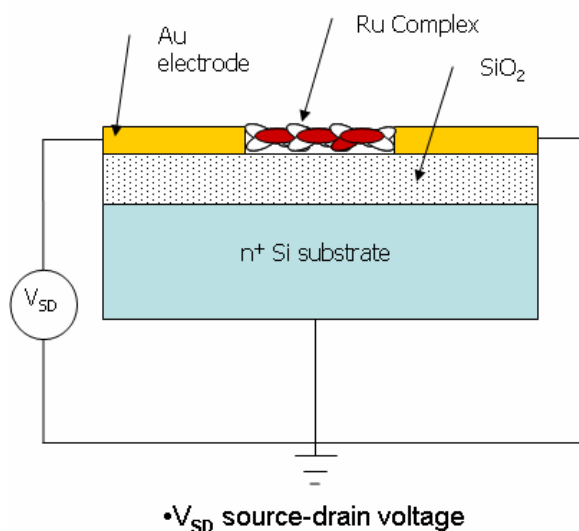


Figure 4.4 Cartoon representation of the ruthenium complex as measured with the gold microcontact pattern on the silicon substrate.

Figure 4.5 shows a current (in A) versus potential (in V) curve (IV curve for short) for a $[\text{Ru}_2(\text{phen})_4(\text{tpphz})]\text{Cl}_4$ sample dropcast on a glass substrate. As the voltage was ramped from -6 to +6 volts, the measured current across the film was found to increase from -80 nA to +72 nA. The current is approximately equal at both negative and positive potentials. Current saturation was not observed for any of these complexes up to potentials of +/- 100 V. The general shape of the I-V curves recorded is similar to published data for other thin films containing ruthenium and osmium polypyridyl complexes.^{85,87,88} The IV curve in Figure 4.5 shows three distinct regions of conduction as noted by the breakpoints at ~-0.8 V and +1.8 V. We will first address the conduction mechanism at the negative and positive region and then we will address the likely conduction mechanism for the central region.

The dual organic/inorganic structure of ruthenium polypyridyl complexes provides several distinct mechanisms by which conduction may occur. The well-defined and reversible redox properties of ruthenium polypyridyl complexes allow both electron donor and acceptor functionality.⁸¹ In electroluminescent films of such complexes, proposed emission mechanisms invoke different methods of electron-hopping processes depending on bias polarity.^{85,89} Similarly, we expect the conductivity mechanism of our complexes to differ with respect to the polarity of the applied voltage.

The redox couples, as determined by solution cyclic voltammetry, for $\text{tpphz}/\text{tpphz}^-$ and $\text{Ru}^{2+}/\text{Ru}^{3+}$ in complex **1**⁴⁺ are -0.78 V and +1.35 V respectively, relative to SCE.^{90,91} As indicated in Figure 4.5, we propose two different conduction pathways

for these ruthenium polypyridyl complexes. Under negative bias, the likely conduction pathway involves ligand reduction, i.e., (the $\text{bpy}^{0/-1}$ couple). Given that the tpphz fragment is the easiest component to be reduced, we assign conduction in this region as occurring by electron-hopping from tpphz fragment to tpphz fragment between adjacent complexes. At positive potentials, we believe conduction is occurring via a hole hopping mechanism centered on the metal ions (the $\text{Ru}^{2+/3+}$ couple).

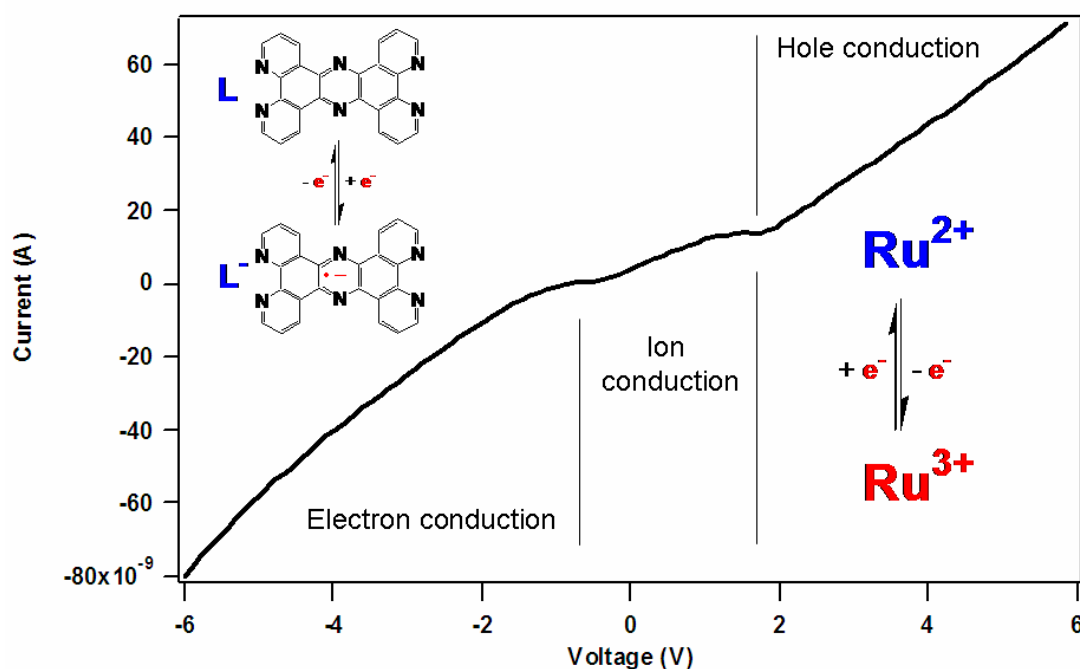


Figure 4.5 Current vs. voltage plot of a $\mathbf{1}(\text{Cl})_4$ sample on a glass substrate. Sample preparation: 0.5 mM $\mathbf{1}(\text{Cl})_4$ in MeOH, drop cast, cycled until stable.

The central region of the IV curve in Figure 4.2 shows a third conduction phenomenon occurring in these films. Since these species are charged, chloride or hexafluorophosphate counterions are present in the films as well. As reported for

related charged metal complexes,^{71,83,89} there is also a contribution to the conductivity due to ion mobility within the film. In this case, there are four negatively charged chloride counterions per ruthenium dimer in these films and we postulate that the conductivity in this region is primarily due to ion conduction.

4.3.2 Ionic Conduction

In Figure 4.5, ionic conduction manifests itself as a rise in the current observed around 0 volts. The two plateaus in the IV curve frame the central region where this process is observed. We believe that the observed current in this region of low potential arises from the movement of the counterions. It should be noted that while this additional current around zero volts is clearly observable for the sample in Figure 4.5, it is not as apparent in every scan. The degree of counterion effects is dependent on several variables such as film thickness, film dryness, temperature, and scan rate.⁸⁸ Although all samples were oven-dried, ionic currents were still sometimes observed due to the presence of small traces of solvent within the films. In fact, traces of water absorbed from the atmosphere have been shown to be sufficient to produce these ionic mobility effects.⁸³

A consequence of this ionic contribution is that we observe that the measured current decreases after repeated scans as the film ages. An example of this phenomenon is shown in Figure 4.6, where taking successive IV measurements on a film of $[\Lambda_4\Lambda_2-3](\text{Cl})_{12}$ reveals a decrease in the maximum current observed during each run. Eventually, the current stabilizes after approximately 25 scans. For this spin-coated $[\Lambda_4\Lambda_2-3](\text{Cl})_{12}$ sample, the current drops from about -300 pA to -120 pA as it was

scanned successively from 0 to -10 V. Initially, the drop in current is rapid, but after several scans, it begins to stabilize and level off. We believe that the counterions present in the films are causing a responsible for this behavior. Changes in current flow as a function of the number of scans has also been reported for films of poly (*N*-vinylcarbazole) doped with LiClO₄.⁹² These changes were attributed to the accumulation of ionic charges at the electrode/film interface. With respect to the ruthenium complexes, movement of the chloride counterions present in the film is likely responsible for the observed charging effect. The film changes over time as a result of the electronic interactions between the counterions and the electrodes. As the anions are attracted to the positive electrode (or repelled by the negative electrode) a charge is built up within the film. If the film is allowed to rest, the film discharges and the measured current increases once again. In Figure 4.6, one additional scan (dashed line) is shown representing a current increase of approximately 20% after the film was allowed to rest for three hours.

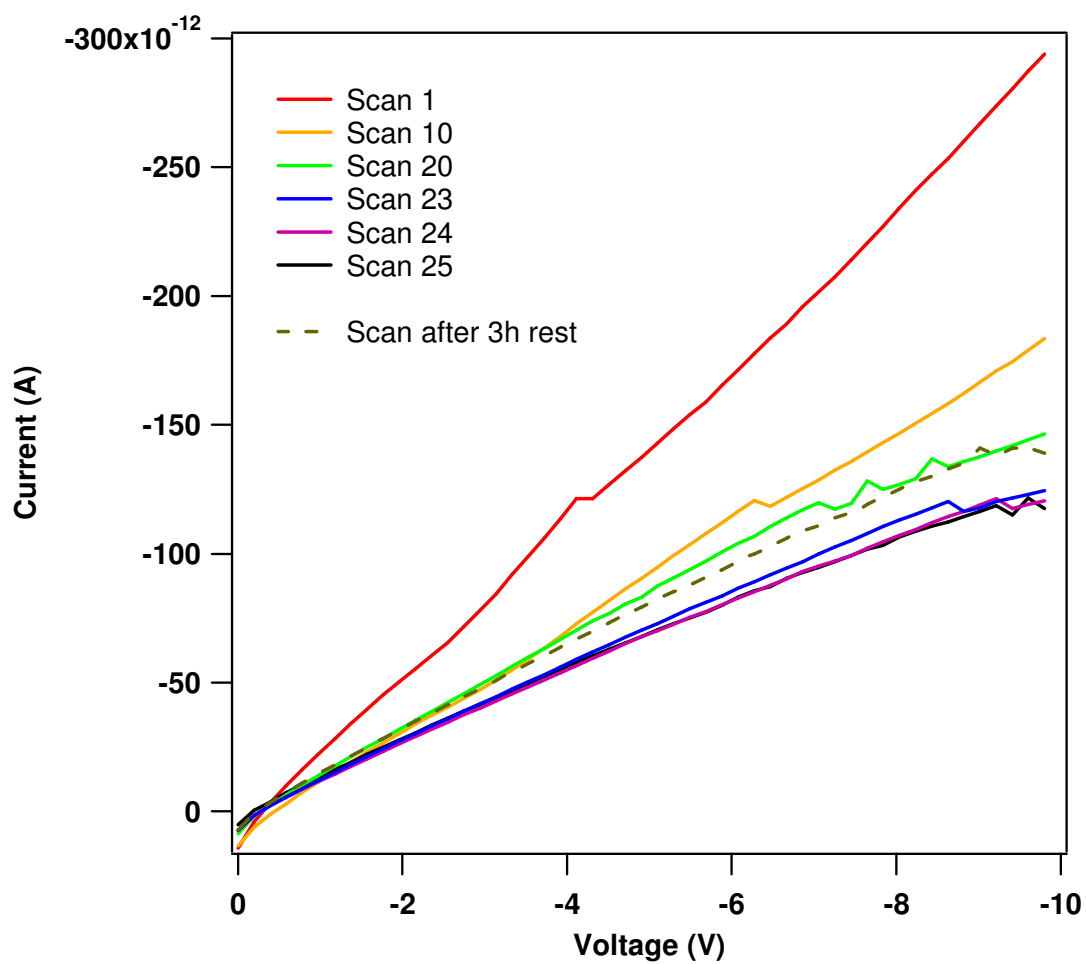


Figure 4.6 Repeat current vs. voltage scans of $[\Lambda_4\Lambda_2\text{-}\mathbf{3}](\text{Cl})_{12}$ on a glass substrate. A scan after a 3 hour resting period is also shown (dashed line). Sample preparation: 0.1 mM $\mathbf{3}(\text{Cl})_{12}$ in MeOH, spin cast.

4.3.3 Effect of Changing the Counterion

The nature of the counterions in these salts affects the conductive properties in different ways. Figure 4.7 compares the current versus voltage plots for $\mathbf{1}^{4+}$ as both the chloride and hexafluorophosphate salts. Measurements were made on dried, filtered drops of solutions of the two samples at equal concentration (0.4 mM).

The chloride sample is more conductive than that of the hexafluorophosphate counterion. Over the -6 to +6 V range, the average measured current for the chloride salt ranges from -78 to +66 nA while the hexafluorophosphate salt falls within +/- 13 nA. In addition, the hexafluorophosphate salt requires higher voltages before it becomes conductive. Figure 4.8 shows a magnified plot of the hexafluorophosphate sample. We observe that the sample is only significantly conductive at potentials greater than approximately +/-4 V.

We attribute these differences to the relative sizes of the counterions. The smaller chloride anions (volume = 24.8 \AA^3)⁹³ allow for a tighter packing where the electron can easily hop between molecules. However, the presence of the much larger hexafluorophosphate anions (volume = 73.0 \AA^3)⁹⁴ results in a film with greater spacing between cations. This reduces the efficiency of the electron hopping mechanism between neighboring molecules. As a result, we see both a diminished level of conductivity and a higher energy requirement (i.e., voltage) to achieve conduction.

Finally, we also looked at samples with the triflate (CF_3SO_3^-) counterion. Interestingly, these samples were completely non-conductive within the voltage ranges tested (+/-20 V). This is consistent with respect to the size of the anion (volume = 86.9

\AA^3),⁹⁴ but it is still somewhat surprising to see complete loss of conductivity considering the modest size difference between the triflate and the hexafluorophosphate anions. However, solution conductivity studies comparing LiPF_6 and LiCF_3SO_3 -based electrolytes have shown that the PF_6^- and CF_3SO_3^- salts produce some of the highest and lowest equivalent conductivities respectively.⁹⁵ In fact, LiCF_3SO_3 salts, in general, are known for their low conductivities.⁹⁶ In thin films of the ruthenium triflate salts, the known tendency of CF_3SO_3^- to self-associate⁹⁵ as well as the oblate ellipsoid shape of the anion (both Cl^- and PF_6^- are spherical)⁹⁵ appears to affect the self-assembly in such a way as to produce similarly poor conduction behavior.

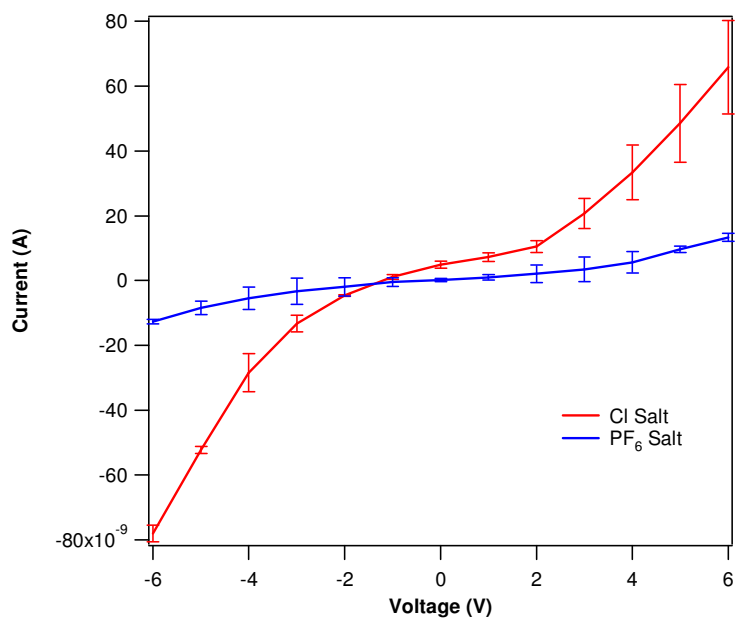


Figure 4.7 Current vs. voltage plots of both the Cl and PF₆ salts of **1**⁴⁺ on a glass substrate. Sample preparation: 0.4 mM **1**(Cl)₄ in MeOH, 0.4 mM **1**(PF₆)₄ in MeCN, drop cast, cycled until stable.

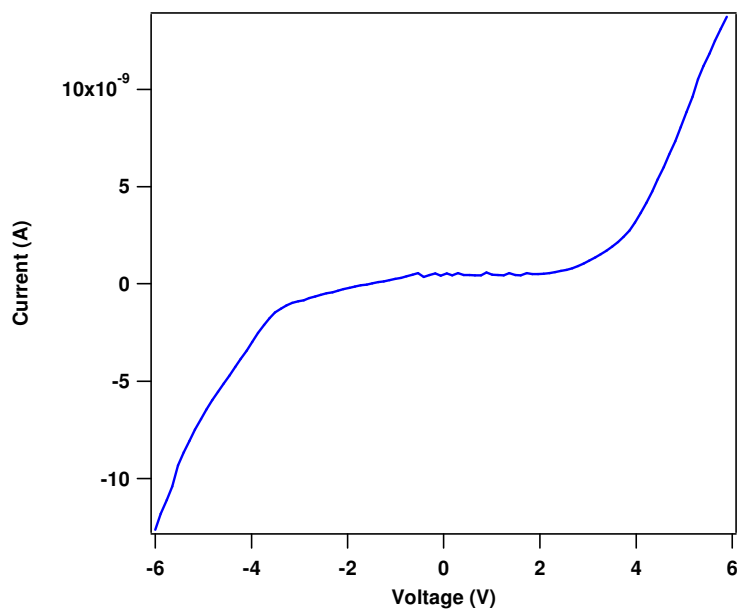


Figure 4.8 Enlarged current vs. voltage plot of **1**(PF₆)₄ on a glass substrate. Sample preparation: 0.4 mM **1**(PF₆)₄ in MeCN, drop cast, cycled until stable.

4.3.4 Conductivity of a Neutral Complex

In an effort to further investigate the significance of the counterions, a neutral ruthenium complex was studied. The complex $[\text{Ru}_2(\text{bpy})_4(\text{oxalato})_2\text{tpphz}]$ [**4**] (Figure 4.9) was available and due to the -2 charge on the oxalato ligands, the overall complex is neutral. As a result, there are no counterions present to alter the film or conduction properties.

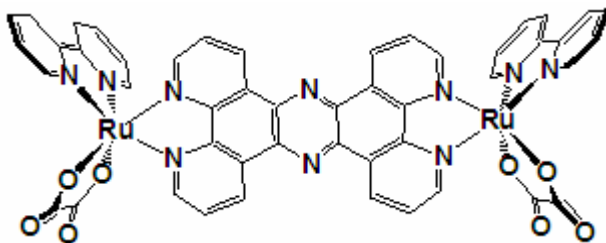


Figure 4.9 $\text{Ru}_2(\text{bpy})_2(\text{oxalato})_2\text{tpphz}$ [**4**]

A sample of **4** was spin-coated onto a glass substrate and its conductivity was measured. As shown in Figure 4.10, the neutral complex is still conductive with current reaching -365 pA as the voltage range is ramped to -20 V. Interestingly, no plateau is observed in the full scan (Figure 4.10, inset), likely due to the fact that the lack of counterions allow for close packing and therefore maximum efficiency of the intermolecular electron hopping.

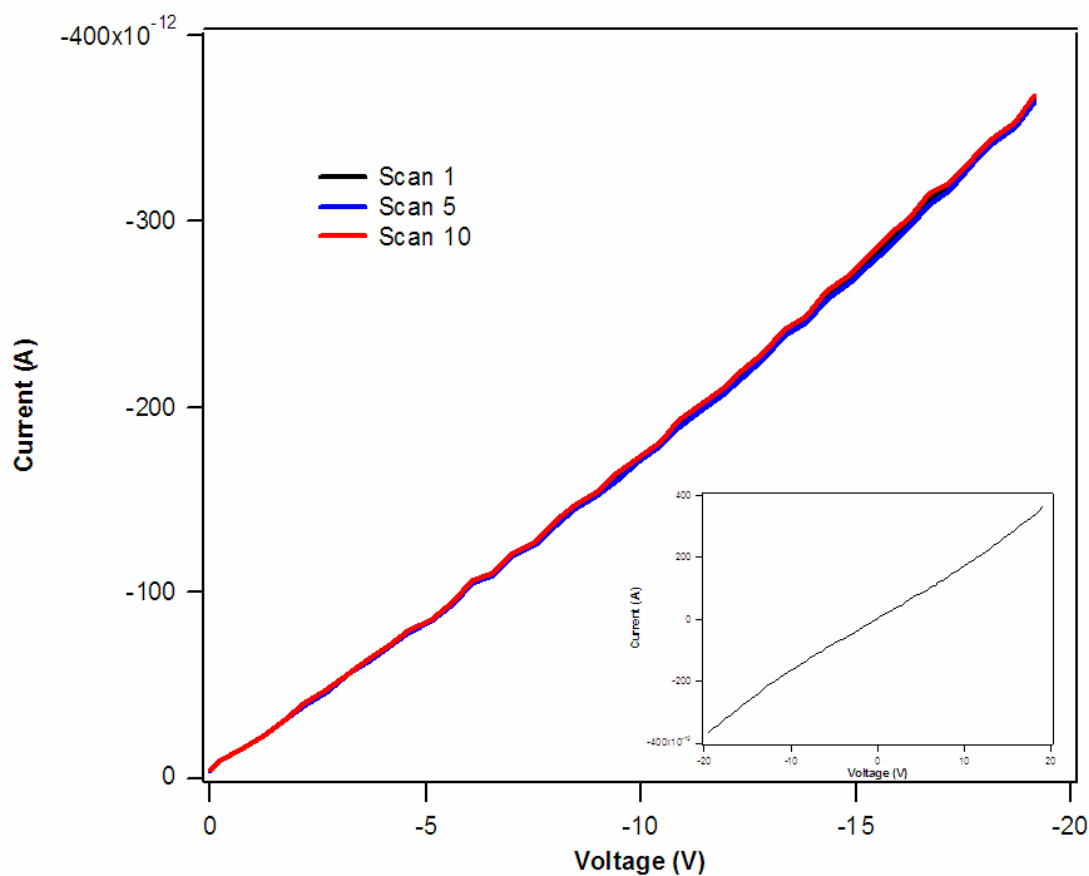


Figure 4.10 Current vs. voltage plot of **4** on a glass substrate; Inset: Full scan from -20 to +20 V. Sample preparation: 0.3 mM **4** in MeOH, spin cast.

Most importantly, the measurement is very reproducible. Successive scans overlap nicely, confirming that the charging effect we observe is related to the counterions. There is also no change in the conductivity if the film is allowed to rest between scans. In the absence of the mobile anions, the film properties remain stable and we do not see the build-up of charge that affects the current measurement.

4.3.5 Temperature Dependence of Conductivity

The effect of temperature on the conductivity of these thin films was also examined. For these experiments, films of [2(Cl₄)] were studied.

As heat is introduced into the system, we expect the ability of electrons to hop from complex to complex to increase. We were interested to see what effect, if any, this would have on the conductivity of the thin films.

The temperature of the system was controlled via both a heating coil and a liquid nitrogen flow. As shown in Figure 4.11, the observed current is much greater at higher temperatures than at lower temperatures. The experiment was conducted on a well-cycled film, measuring the conductivity from low to high temperature in order to minimize any effects related to ion mobility.

Figure 4.12 plots the maximum observed current (at -40V) as a function of temperature. As the temperature was varied between -110 and +85 °C, we measured conductivity ranging between only a few pA up to 30 nA. There is a marked increase in conductivity above room temperature, where the current rises rapidly with increasing temperature. However, below room temperature, the current decreases and by -100 °C, the film is essentially non conductive with an observed current of less than a tenth of a pA. This semiconductor-like behavior is in agreement with published temperature dependent conductivity data of other films of ruthenium and osmium polypyridyl complexes.^{87,89}

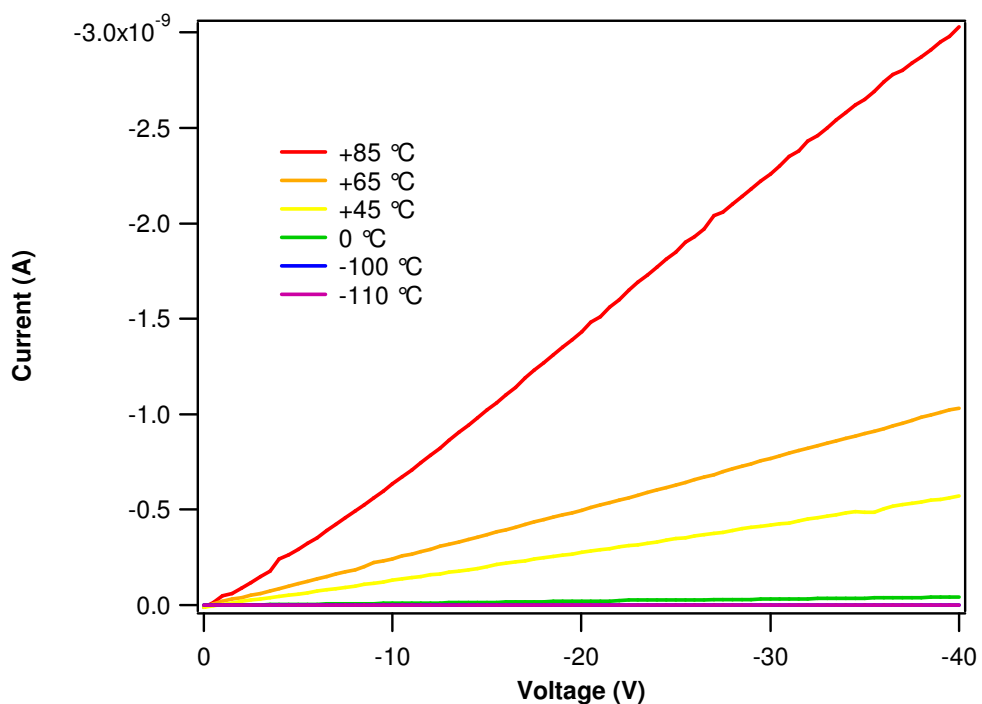


Figure 4.11 Temperature dependence of $[2(\text{Cl}_4)]$ conductivity between temperatures of -110 and +85 °C. Sample preparation: 0.3 mM $2(\text{Cl})_4$ in MeOH, spin cast, cycled until stable.

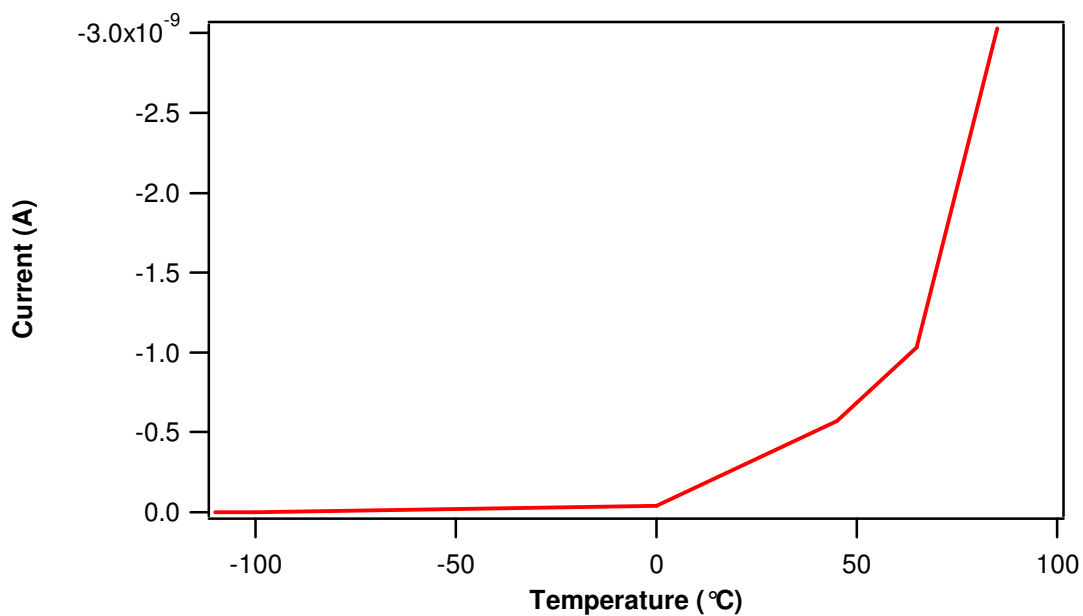


Figure 4.12 The current measured at -40 V for $[2(\text{Cl}_4)]$ as a function of temperature. Sample preparation: 0.3 mM $2(\text{Cl})_4$ in MeOH, spin cast, cycled until stable.

4.3.6 Tertiary Structure and Conductivity

One important goal of this work is to develop the ability to fine tune the macroscopic properties of these complexes via control of the molecular interactions and arrangements. With this in mind, the molecular conductivities of thin films of two diastereomers, $[\Lambda_4(\Delta\Lambda)\text{-}\mathbf{3}]\text{Cl}_{12}$ and $[\Lambda_4\Lambda_2\text{-}\mathbf{3}]\text{Cl}_{12}$ (Figure 4.13) were compared.

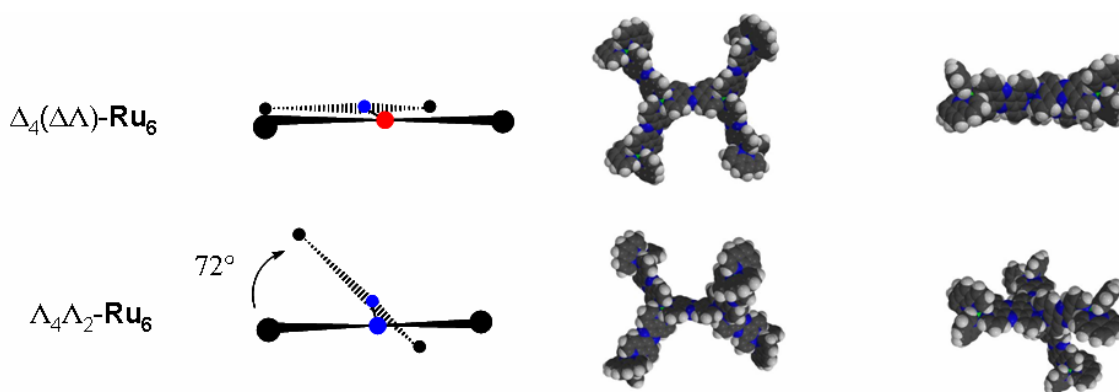


Figure 4.13 Ball and stick and space-filling diagrams of $[\Lambda_4(\Delta\Lambda)\text{-}\mathbf{3}]\text{Cl}_{12}$ and $[\Lambda_4\Lambda_2\text{-}\mathbf{3}]\text{Cl}_{12}$.

As discussed in Chapter 2, these two complexes have identical chemical compositions, but have distinctly different spatial arrangements. Through a careful, stereospecific synthesis, two different tertiary structures are generated, one planar ($[\Lambda_4(\Delta\Lambda)\text{-}\mathbf{3}]\text{Cl}_{12}$) and one twisted ($[\Lambda_4\Lambda_2\text{-}\mathbf{3}]\text{Cl}_{12}$). This is accomplished solely by varying which enantiomers make up the core of the molecules.

Since electric birefringence experiments revealed differences in the aggregation properties in solution, we hoped to see differences in the packing arrangement in the

solid state as well. In this case, we looked at the thin films formed from spincoat 0.1 mM methanolic solutions on glass.

As shown in Figure 4.14, films of the planar $[\Lambda_4(\Delta\Lambda)\text{-}\mathbf{3}]\text{Cl}_{12}$ are more conductive than those made from $[\Lambda_4\Lambda_2\text{-}\mathbf{3}]\text{Cl}_{12}$. For the planar hexamer, we see an average measured current of approximately 213 pA at 10 V, whereas, in the other case, we see only an average of 112 pA under the same conditions.

We know from solution studies (as discussed in Chapter 2) that the aggregate forms of $[\Lambda_4\Lambda_2\text{-}\mathbf{3}]\text{Cl}_{12}$ and $[\Lambda_4(\Delta\Lambda)\text{-}\mathbf{3}]\text{Cl}_{12}$ are different. As dry, thin films, these differences of assembly appear to affect the intermolecular interactions with respect to electron hopping. This exciting observation demonstrates the ability to exert some control over a macroscopic property (electrical conductivity) by simply tuning the structural characteristics during synthesis. In other words, depending on the enantiomers chosen in the design of the molecule, the bulk properties of the material can be altered.

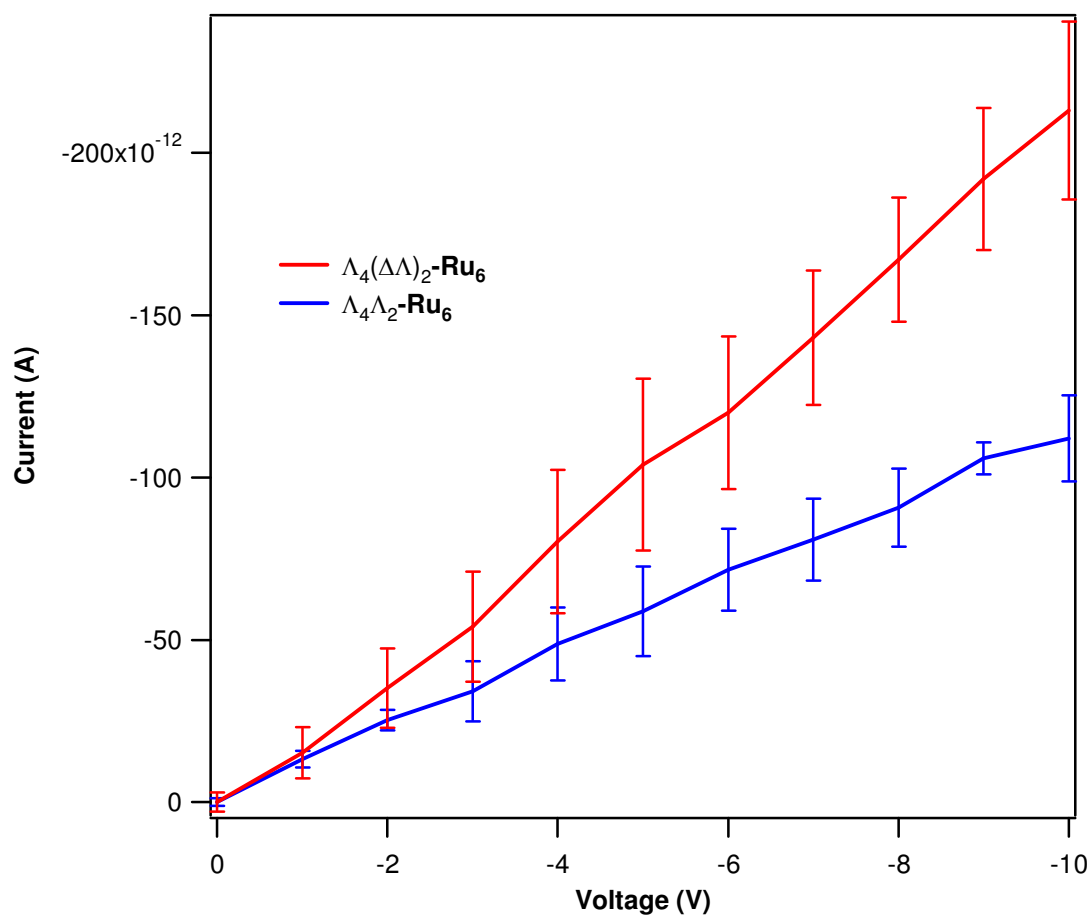


Figure 4.14 Current vs. voltage plots of $[\Lambda_4(\Delta\Lambda)\text{-}\mathbf{3}]\text{Cl}_{12}$ and $[\Lambda_4\Lambda_2\text{-}\mathbf{3}]\text{Cl}_{12}$ on a glass substrate. Sample preparation: 0.1 mM $[\Lambda_4(\Delta\Lambda)\text{-}\mathbf{3}](\text{Cl})_{12}$ in MeOH, 0.1 mM $[\Lambda_4\Lambda_2\text{-}\mathbf{3}](\text{Cl})_{12}$ in MeOH, spin cast, cycled until stable.

4.4 Summary and Conclusion

Thin films of ruthenium(II) polypyridyl complexes are conductive with measured currents varying depending on the amount of material present (usually in the pA to nA range). The conduction is a combination arising from electron/hole hopping between molecules as well as an underlying ionic conduction due to the presence of the counterions. The ionic component becomes negligible after repeated scans, but the nature of the counterion is important. The conduction is temperature dependent with higher temperature resulting in higher conductivity, consistent with semiconductor-like behavior. Importantly, the three-dimensional, tertiary structure of the complexes can be used to tune the observed conductivity, presumably due to differences in packing efficiency.

It should also be noted that other electronic effects were studied such as the effect of chemically doping the complexes with reducing/oxidizing agents and modulating the conductivity using an applied gate potential. The results from these studies were inconclusive due to limitations of the testing apparatus. Preliminary results were not sufficiently promising to warrant extensive efforts to improve the testing conditions and environment.

CHAPTER 5

PHOTOCHEMISTRY AND AGGREGATION

5.1 Introduction

It has previously been reported that complexes $[\text{Ru}_2(\text{phen})_4\text{tatpp}]^{4+}$ (**P**) and $[\text{Ru}_2(\text{phen})_4\text{tatpq}]^{4+}$ (**Q**) undergo up to 2 (for **P**) and 4 (for **Q**) sequential photoreductions of their central bridging ligands when irradiated with visible light in the presence of sacrificial reducing agents, such as TEA or TEOA in MeCN.⁹⁷ As shown in Figure 5.1, we refer to the fully reduced forms as **H₂P** and **H₄Q**. The distinguishing feature of these complexes is the fact that all of the electrons are stored on the same bridging ligand (tatpp or tatpq). Potentially, these complexes could be used to deliver multiple electrons (and protons) in a concerted fashion to a variety of small-molecule substrates.

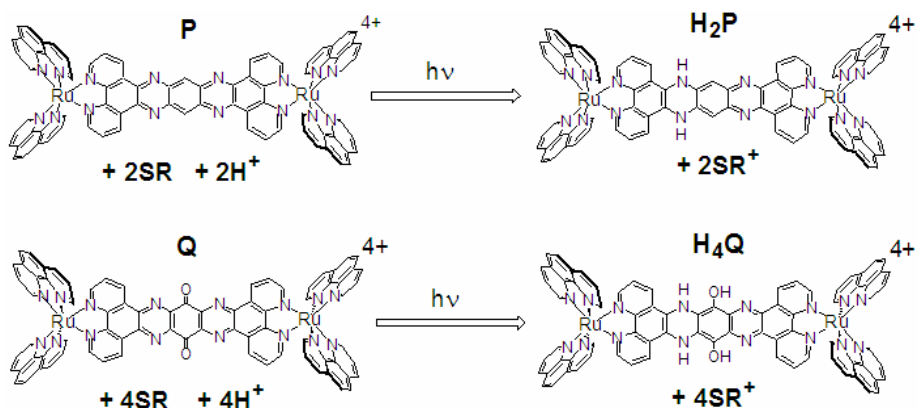


Figure 5.1 Dimers **P** and **Q** and their multi-electron photoreduction with a sacrificial reducing agent (SR).

The aim of this portion of the project is to begin to explore the possibilities of incorporating what we know about molecular organization with the interesting and unusual photophysical properties of these complexes. The primary focus of the research has been on **P**, so this discussion will principally concentrate on this complex.

5.1.1 Spectroscopic Characterization of **P**

Much work has previously been done concerning **P** in efforts to fully understand its photochemical behavior.⁹⁸ The photoreduction of the complex has been extensively studied in MeCN, H₂O, and mixed MeCN/H₂O solutions at varying pH. In addition, stoichiometric chemical reductions/protonations as well as spectroelectrochemical experiments have been conducted to determine the species involved in these processes. Figure 5.2 shows the various redox/protonation states exhibited by complex **P**. As shown in the figure, we use the shorthand notation of **P**, **P**^{•-}, **HP**^{•-}, etc. to refer to each intermediate species.

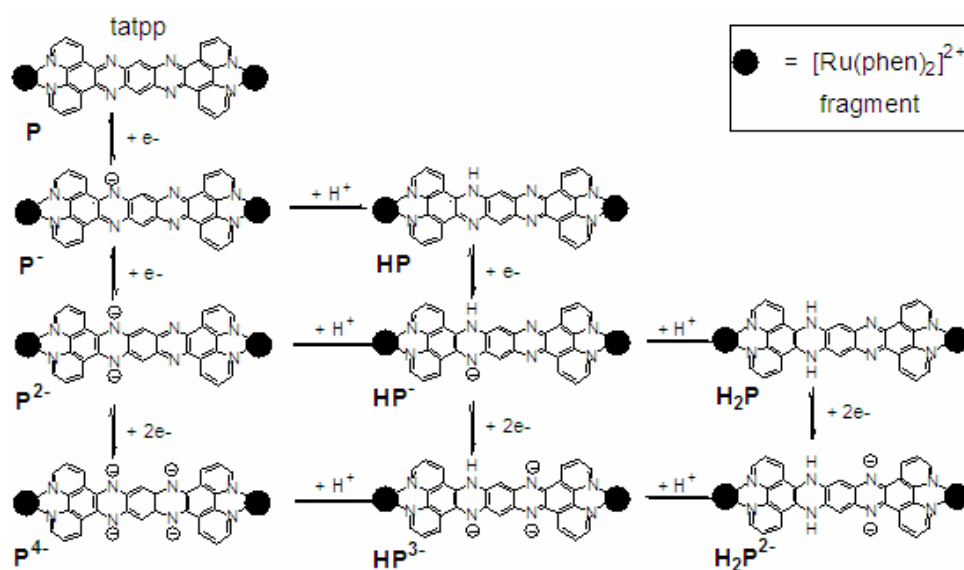


Figure 5.2 Ladder scheme of redox/protonation states of **P**.

5.1.2 UV-Vis Absorption Spectrum of **P**

UV-Vis spectroscopy is the primary method by which we identify the various species of **P**. One new contribution to the understanding of this project was the discovery that the UV-Vis absorption spectrum of **P** is actually a compound spectrum made up of the sum of the absorptions of two $[\text{Ru}(\text{phen})_3]^{2+}$ chromophores and the tatpp ligand (Figure 5.3). The ‘free’ tatpp ligand spectrum is actually that of a Zn(II) complex, for the ligand itself is insoluble in MeCN. There are no MLCT transitions observed for the Zn(II)-tatpp adduct, and the LC transitions are unlikely to be greatly affected by the presence of the Zn(II).

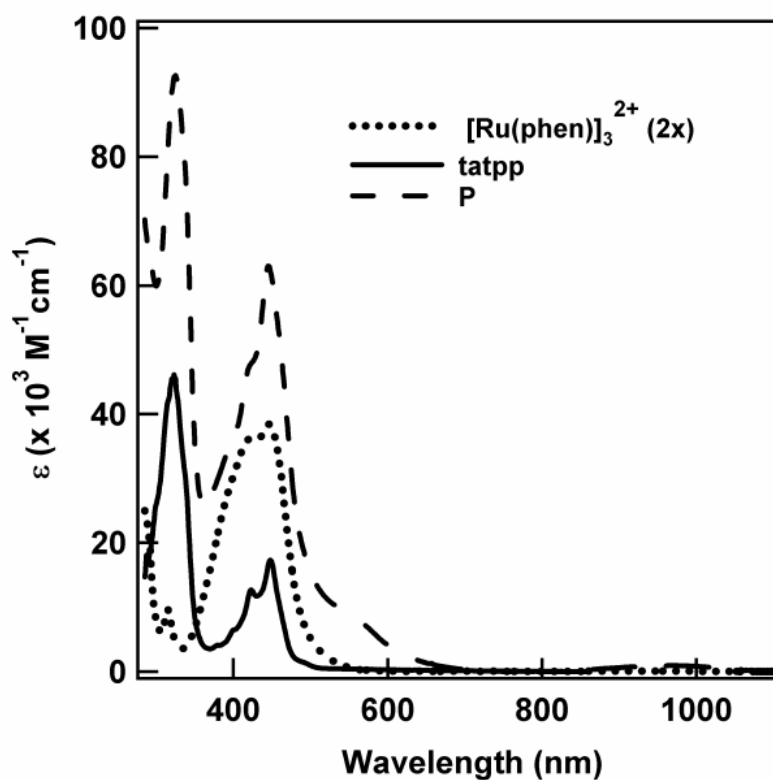


Figure 5.3 Overlaid UV-Vis absorption spectra of $[\text{Ru}(\text{phen})_3]^{2+}$, zinc(II)-tatpp adduct (tatpp), and **P** in MeCN.

The absorption spectrum for **P** can be understood as the sum of its components. Essentially, the complex can be envisioned as the combination of two $[\text{Ru}(\text{phen})_3]^{2+}$ subunits bridged by one tatpp unit. The molar extinction coefficients for $[\text{Ru}(\text{phen})_3]^{2+}$ and tatpp at 450 nm in MeCN are $19,200 \text{ M}^{-1}\text{cm}^{-1}$ and $17,300 \text{ M}^{-1}\text{cm}^{-1}$, respectively.^{22,99} The total molar extinction coefficient for **P** can be predicted via summation of the coefficients of two $[\text{Ru}(\text{phen})_3]^{2+}$ components and one tatpp component. This calculated value of $55,700 \text{ M}^{-1}\text{cm}^{-1}$ compares reasonably well with the observed extinction coefficient of **P** of $65,100 \text{ M}^{-1}\text{cm}^{-1}$ at 445 nm in MeCN.⁵⁰

5.1.3 Spectra of Reduced Species

Seven of the nine redox/protonation states for **P** have previously been characterized by UV-Vis spectroscopy, as shown in Figure 5.4. These spectra were obtained in dry MeCN using cobaltocene as a stoichiometric reductant and trifluoroacetic acid as a stoichiometric proton source.⁹⁸ As complex **P** is reduced, significant changes to its UV-Vis absorption spectrum are observed, particularly in the transitions at 335 and 445 nm. In addition, each species shows unique, characteristic transitions in the visible region. As a result, we are able to identify the redox/protonation state of any particular sample of **P** via its unique absorption “fingerprint”. It should be noted that **HP** is not observable due to a rapid disproportionation to **H₂P** and **P[•]**.

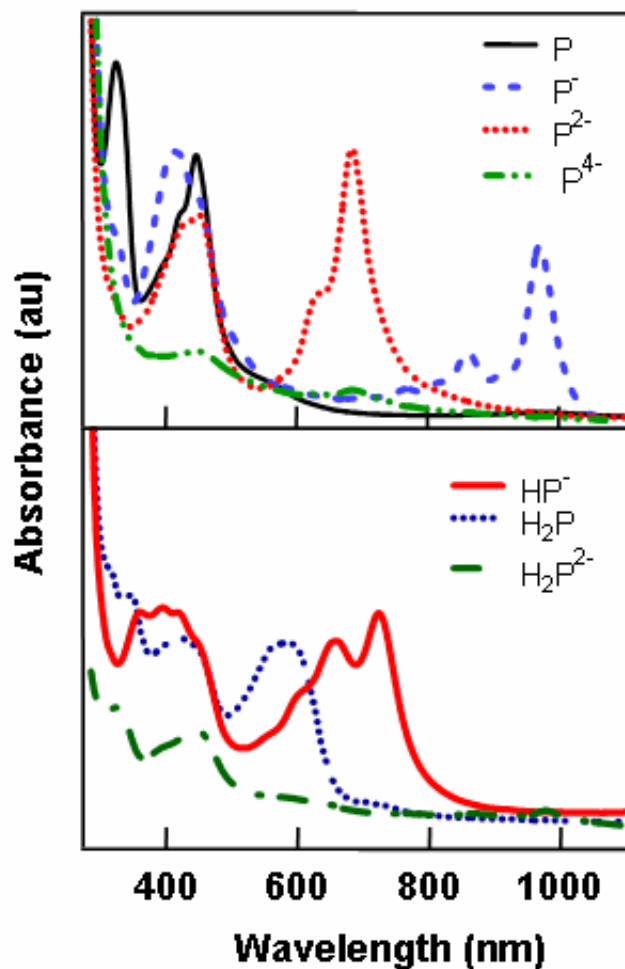


Figure 5.4 Absorption spectra in MeCN of **P** in various redox and protonation states.

5.1.4 Photochemistry of **P**

A solution of complex **P** undergoes two sequential reductions when exposed to light, in the presence of a sacrificial electron donor (either TEA or TEOA). At the low concentrations used in these experiments, these amines are not sufficiently reducing to react with the ground state of **P**. The species of **P** accessible photochemically parallel

those observed chemically (and spectroelectrochemically) in both MeCN and aqueous solution as a function of pH.

The photoreduction of **P** in MeCN is shown in Figure 5.5. The photoproducts generated were identified by comparison of their absorption spectra with those for **P[•]**, **H₂P**, **HP[•]**, and **P^{2•}** generated chemically. From this data, it has been determined that, in MeCN, **P** is first photoreduced to **P[•]** and then to **HP[•]**. **HP[•]** cannot be reduced further photochemically. Upon exposure to air, **P** is regenerated, and if the solution is degassed, the reduction process can be repeated.

In H₂O, **P** can also be photoreduced, but the products generated are strongly dependent on the solution pH. Under basic conditions, the reduction process echoes the reduction in MeCN with the initial formation of **P[•]** and then a second reduction to form **HP[•]**. While not strictly relevant to this project, it should be noted that the reduction at lower pH has been previously been studied extensively.⁹⁹

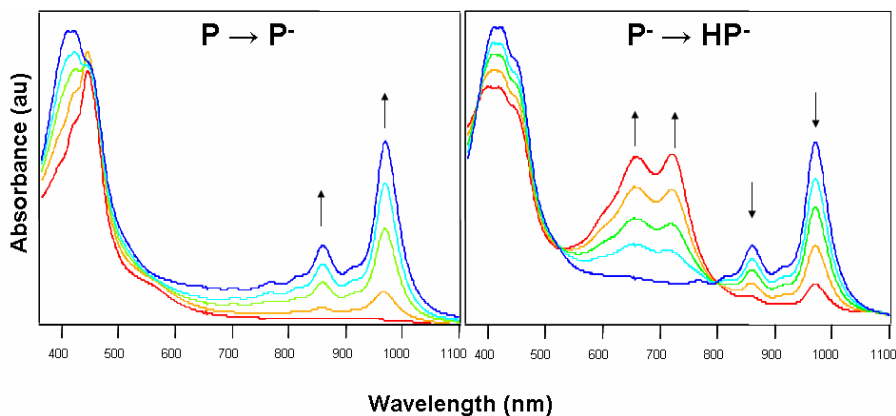


Figure 5.5 Photoreduction of **P** in MeCN after 0 to 2 minutes (left), and 3 to 12 minutes (right). 100 W tungsten bulb (light source), 360 nm cutoff filter, 16 μ M of **P**, 0.25 M Triethylamine.

5.1.5 The Mechanism of Photoreduction

Upon absorption of a photon, a charge-separated excited state is generated, denoted as **P*** (Figure 5.6). This MLCT transition can be expressed as $[(\text{phen})_2\text{Ru}^{2+}(\text{tatpp})\text{Ru}^{2+}(\text{phen})_2]^{4+} \rightarrow [(\text{phen})_2\text{Ru}^{3+}(\text{tatpp}^-)\text{Ru}^{2+}(\text{phen})_2]^{4+}$ wherein an electron is promoted from the metal center to the tatpp ligand.

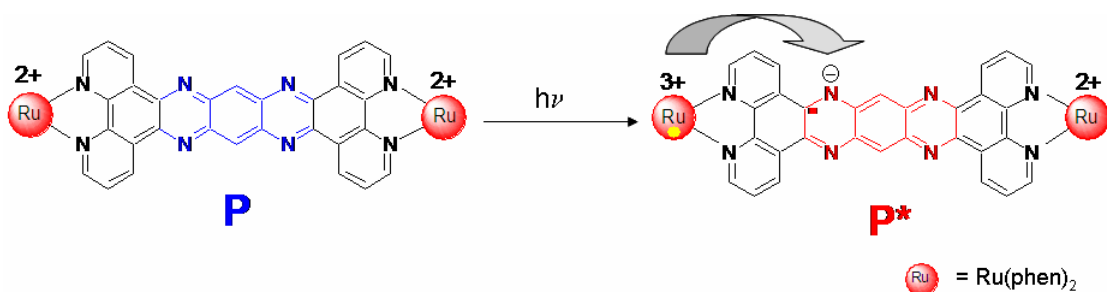


Figure 5.6 Photochemical formation of **P***.

This photoexcitation initially involves the formation of a singlet ($^1\text{MLCT}_1$) then rapidly, via intersystem crossing, a triplet excited state ($^3\text{MLCT}_1$) in which the electron is located on the phenanthroline-like portion of the bridging ligand. A state diagram for **P** is shown in Figure 5.7, illustrating the energy migration through the molecule. The $^3\text{MLCT}_1$ quickly (~20 ps) relaxes to the lowest lying triplet state ($^3\text{MLCT}_0$) via an intramolecular electron transfer from the phenanthroline portion to the pyrazine-benzene-pyrazine unit.⁵⁰

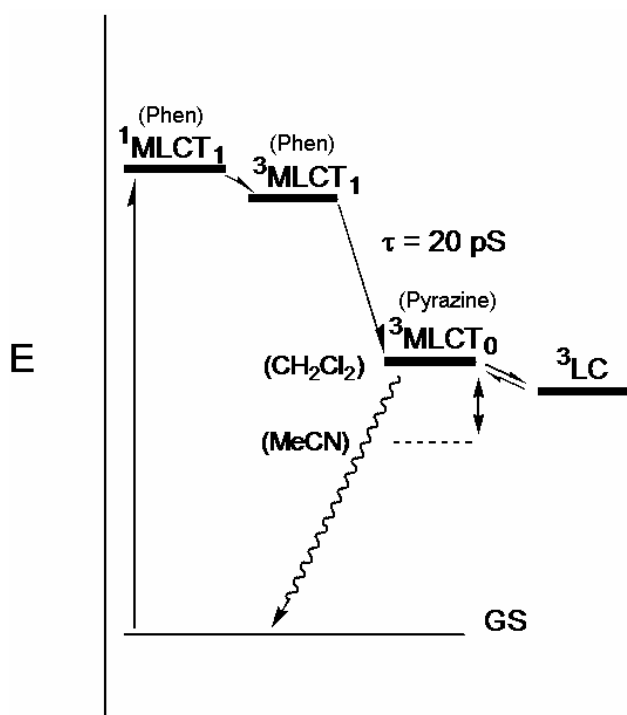


Figure 5.7 State diagram for **P** showing energy migration through the molecule.

In the absence of a sacrificial electron donor, this charge-separated excited state (**P**^{*}) undergoes charge recombination to return to the ground state (**P**) as shown in Figure 5.8. The lifetime of **P**^{*} has been measured using ultrafast transient absorption spectroscopy, and in CH₂Cl₂ was found to be 1.3 μs, which is exceptionally long.¹⁰⁰ In MeCN, this lifetime was dramatically shortened to ~5 ns. This behavior has been attributed to the presence of a ligand-centered triplet state (³LC) which is in rapid equilibrium with the ³MLCT₀ state, as shown in Figure 5.7.¹⁰¹

The ³MLCT₀ state is essentially a polar excited state due to the charge separation of the formal 3⁺ charge on the Ru atom and the 1⁻ charge on the central portion of the bridging ligand. However, the ³LC state has a considerably smaller

dipole moment with both excited electrons situated on the bridging ligand. As a result, solvent polarity affects these energy states unequally. In a polar solvent (MeCN), the $^3\text{MLCT}_0$ state is stabilized, thus making it the lowest energy state. Charge recombination from this low energy state is very rapid. However, in a non-polar solvent (CH_2Cl_2), the $^3\text{MLCT}_0$ state is destabilized, resulting in an equilibrium shift towards the ^3LC state. The charge recombination pathway from the ^3LC state is longer; therefore, as it becomes more populated, the overall lifetime of the excited state (P^*) is greater.

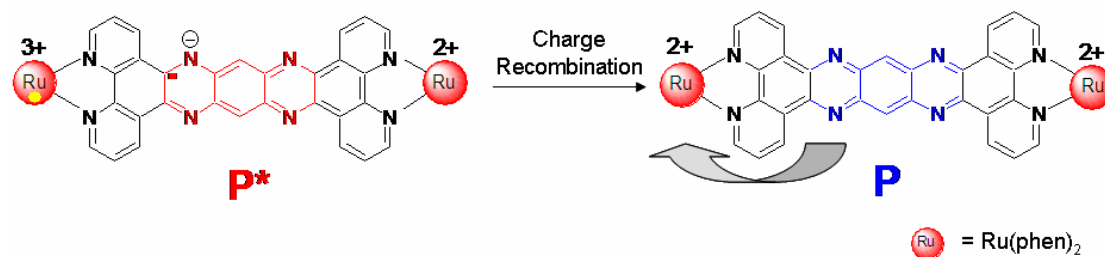


Figure 5.8 Return of P^* to the ground state.

In order to photochemically generate the reduced species of P , a sacrificial electron donor must be used, such as TEA or TEOA. As shown in Figure 5.9, the role of this species is to reductively quench the excited state, P^* . By donating an electron to the Ru^{3+} atom, it effectively fills the “hole” on the metal center, thus trapping the excited electron on the bridging ligand. This species, with one electron stored on the tatpp ligand is the singly-reduced complex, P^\bullet . This photochemical process can be repeated once more, generating a species with two electrons stored on the bridging ligand.

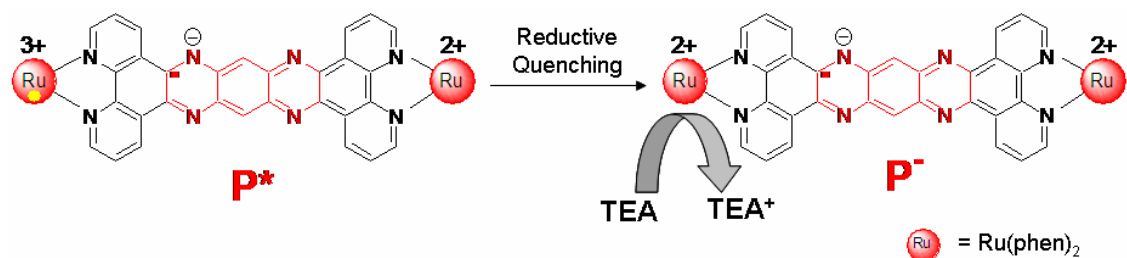


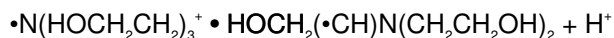
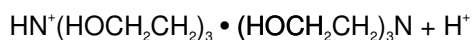
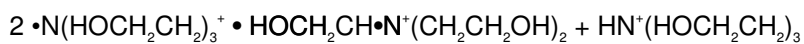
Figure 5.9 Formation of \mathbf{P}^- via reductive quenching of \mathbf{P}^* by TEA.

TEA (or TEOA) is considered to be a one electron donor and the fate of the resulting radical cation has been reported in literature.¹⁰² For TEOA, the resulting radical cation rapidly decomposes to give H^+ and other products as shown in the following reactions:

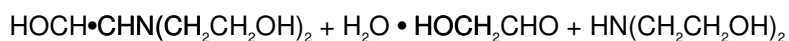
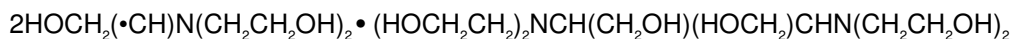
Initiation



Rearrangement/ Deprotonation



Termination/Decomposition



The photoreduction is a bimolecular process, and assuming first-order in both \mathbf{P}^* and TEOA, the rate of photoreduction ($\Delta[\mathbf{P}^*]/\Delta t$) is described by the expression $k[\mathbf{P}^*][\text{TEOA}]$. Therefore, the lifetime of \mathbf{P}^* is critically important, for the longer the excited state lives, the greater the effective concentration of \mathbf{P}^* in solution. In other words, the rate of the photochemical reduction of complex \mathbf{P} is dependent on the lifetime of \mathbf{P}^* .

With this in mind, we were interested in studying the effects of aggregation on the photochemistry of \mathbf{P} . Due to the fact that the lifetime of \mathbf{P}^* is affected by the polarity of its environment (*vide supra*), we postulated that the formation of π - π stacked aggregates of \mathbf{P} may effectively generate a relatively non-polar environment about the bridging moiety and thereby extend the lifetime of \mathbf{P}^* . NMR studies (*vide infra*) indicate that π - π aggregates of \mathbf{P} do form as a function of concentration in aqueous solution. This chapter reports on our attempts to examine the effect of this aggregation on the photochemical reduction of \mathbf{P} in aqueous solution.

5.2 Experimental

Materials. The compounds tatpp and $[\text{Ru}_2(\text{phen})_4\text{tatpp}]^{4+}$ were prepared according to published procedures.⁵⁰ The ligand tatpp was purified via the new method described below. All other chemicals and solvents used were of reagent grade and used without further purification.

Procedure for purification of tatpp

Crude tatpp (0.3 g, 0.6 mmol) was suspended in 150 mL of acetonitrile. Excess zinc tetrafluoroborate (0.86 g, 3.6 mmol) was added and the mixture was stirred while heating until all of the tatpp was dissolved. In a separate flask, disodium ethylenediamine tetraacetate (1.4 g, 3.8 mmol) was dissolved in 50 mL of hot H₂O. Once dissolution was complete, the EDTA solution was added to the Zn-tatpp solution and the mixture was heated while stirring for 10 minutes. The precipitated tatpp was removed immediately via filtration and washed with 10-20 mL of hot H₂O. The product was then dried *in vacuo* at 60°C. Yield: 0.14 g (47%).

Instrumentation. ¹H NMR spectra were obtained on a JEOL Eclipse Plus 500 or 300 MHz spectrometer using D₂O. Chemical shifts were given in ppm and referenced to the residual proton signal from the deuterated solvent. UV-Visible absorption data were obtained using a Hewlett-Packard HP84535A spectrophotometer under the given conditions. ESI Mass Spectra were obtained on a Thermo Electron LCQ Deca-XP mass spectrometer.

Methods. For the photochemical experiments, the 0.1 M TEOA stock solution was degassed using the freeze/thaw method (5 cycles). All samples were prepared in the glove box and were sealed in quartz cuvettes with either plastic caps or rubber septa and wrapped with parafilm prior to irradiation. For the concentration studies, one 160 μM solution was prepared and a portion was diluted by a factor of 10 to obtain the 16 μM solution. The 160 μM solution was sealed in a 1 mm cuvette while the 16 μM solution was sealed in a 10 mm cuvette to ensure equal absorption values. During

irradiation, the cuvettes were immersed in a water bath (18 ± 1 °C) and irradiated using a 100-W tungsten bulb. The source-to-sample distance was approximately 3 cm. The progress of the photochemical reaction was monitored by periodically removing the cuvette from the water bath and recording the absorption spectra. The light source was turned off while taking measurements. The samples were run sequentially and the second sample cuvette was wrapped in aluminum foil to shield it from light during the first measurement. Each experiment was repeated a total of three times, with a new, freshly-prepared 160 μ M solution of **P** used in each run.

For the ionic strength experiments, the same general procedure was followed, but a 16 μ M solution of **P** was made directly. The NaCl was weighed and degassed in Schlenk flasks prior to bringing them into the glovebox. Separate fractions of 20 mL each were removed from the stock solution to generate the 0.1 and 0.01 M NaCl solutions. All samples were placed in 10 mm cuvettes and sealed with plastic caps and parafilm.

Differential pulse voltammetry (DPV) experiments were performed using a PC-controlled potentiostat (CH Instruments, electrochemical analyzer). A glassy carbon (1.5 mm diameter disk) working electrodes from Cypress Systems was used. A Pt wire and a premium "no leak" Ag/AgCl reference electrode (Cypress, model EE009) were used as counter and reference electrodes, respectively, and potentials are quoted with respect to this reference. Experiments were conducted in dry acetonitrile (HPLC grade) with 0.1 M NBu₄PF₆ as the supporting electrolyte. All experiments pertain to the laboratory ambient temperature (20 ± 2 °C).

The mass spectroscopy data were obtained using ESI-MS. The samples were prepared with concentrations of 10 μ M **P** (Sample A) and 10 μ M **P** with 0.01 M NaCl (Sample B).

5.3 Aggregation of P

As discussed previously, this family of ruthenium polypyridyl complexes has a tendency to aggregate when in solution. Much effort has been invested into gaining a better understanding of the nature of the aggregation of complex **P**.

5.3.1 Crystals of Related Complexes

Growing crystals of these complexes has always been a tremendous challenge. In fact, despite extensive efforts, no crystal of **P** has ever been obtained. Ironically, we suspect that the very tendency of the complex to aggregate is preventing proper crystal formation. At this point, the best we can do is look to crystals of related complexes to form a model of what the aggregate structure might look like.

From literature, we have a crystal structure for $[\text{Ru}_2(\text{bpy})_4\text{tpphz}]^{4+}$ (**Z**).¹⁰³ This complex is very closely related to **P**, the major difference being the length of the bridging ligand. In Figure 5.10, we can see that the molecule stacks in a parallel fashion along its bridging ligand. The distance between molecules is approximately 3.4 angstroms, which suggests a π - π stacking arrangement. We think it is reasonable to assume that **P** aggregates into a similar arrangement. In fact, the longer bridging ligand of **P** may even serve to make the π - π interaction more favorable with more room for overlap.

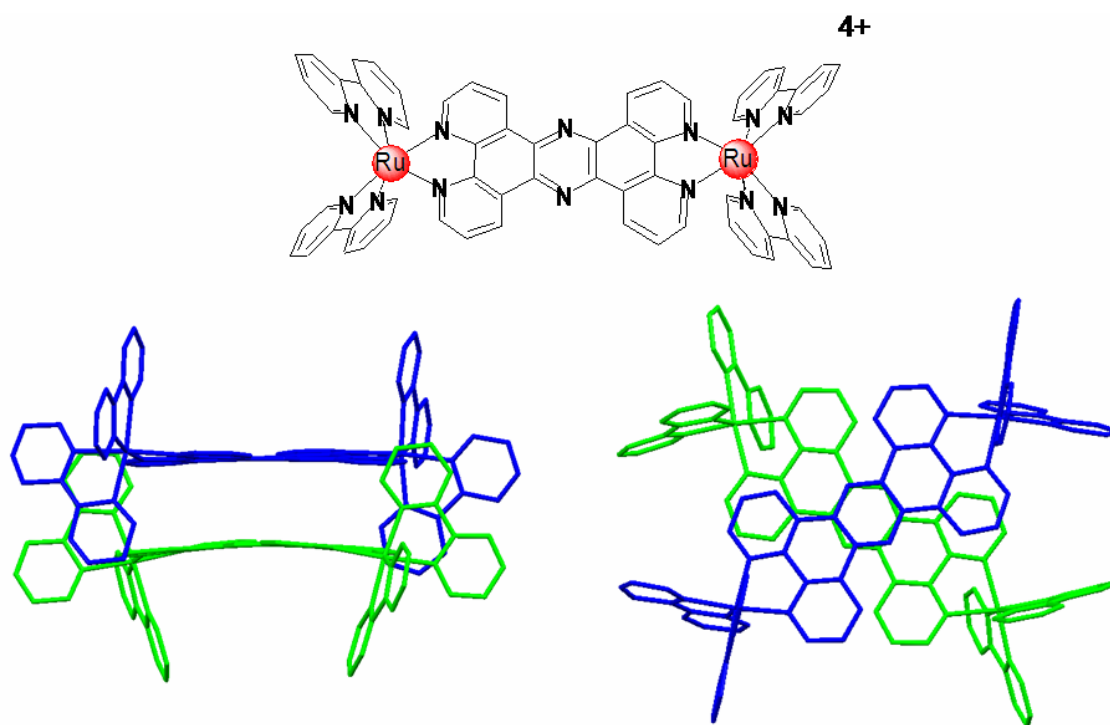


Figure 5.10 Chemdraw and crystal structures of **Z**.

Furthermore, a former colleague (Dr. Thamara Janaratne) was able to grow crystals of another related complex, $[Ru_2(bpy)_4tatpq]^{4+}$ (**Q**). This molecule is synthesized by oxidizing **P** to form a quinone on the central ring of the bridging ligand. While these structures shown in Figure 5.11 were only partially resolved, we can still gain some knowledge regarding the packing arrangement of the molecule. Like **Z**, we observe that **Q** stacks along its bridging ligand, further suggesting that **P** behaves similarly. Unfortunately, the presence of the quinone moiety prevents parallel stacking between complexes. While this perturbation may account for the ability of crystal formation, the intermolecular interaction is no longer a π - π arrangement. In this case, a PM3 calculation on the tatpq bridging ligand (Figure 5.12) shows a region of low

electron density on the central portion of the ligand with regions of high electron density on the periphery. As a result, a donor-acceptor interaction takes place where a quinone oxygen atom from one **Q** is oriented toward the phenanthroline portion of an adjacent **Q** molecule's tatpq ligand.

Furthermore, by repeating the unit cell, we can expand the crystal structure of **Q** to study its long range ordering. As shown in Figure 5.13, we observe that **Q** organizes into a stacked, columnar arrangement. Due to the structural similarities, we postulate that **P** follows this pattern, and also aggregates into a series of columns.

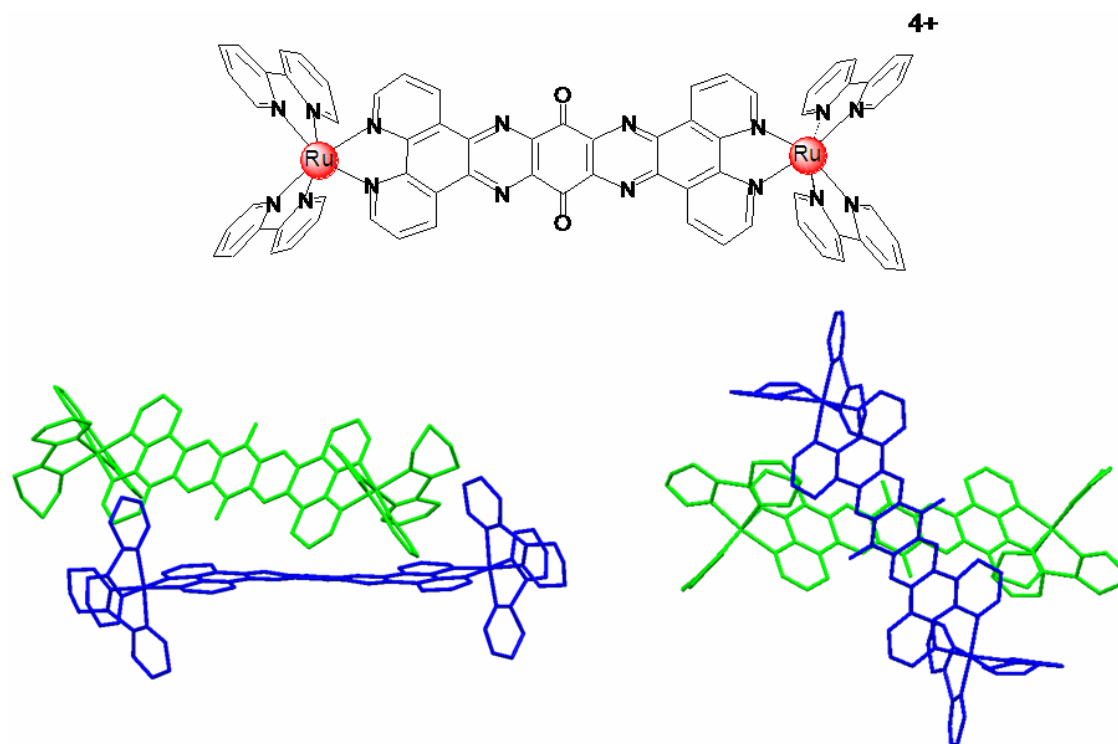


Figure 5.11 Chemdraw and crystal structures of **Q**.

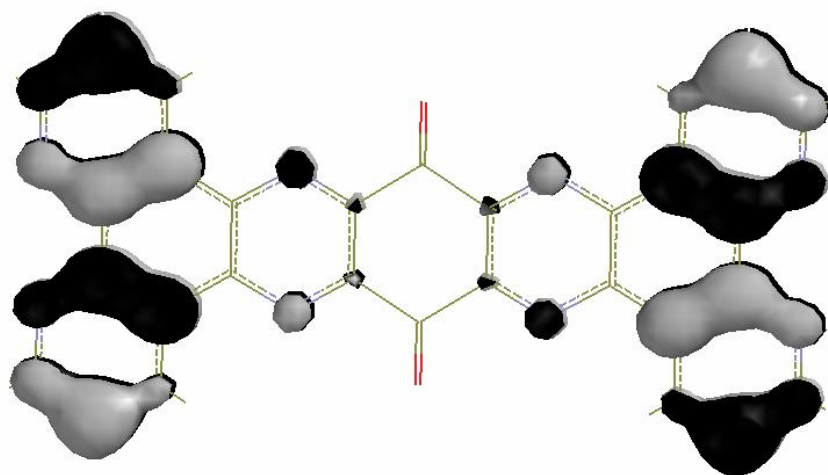


Figure 5.12 PM3 calculation of the HOMO of tatpq.

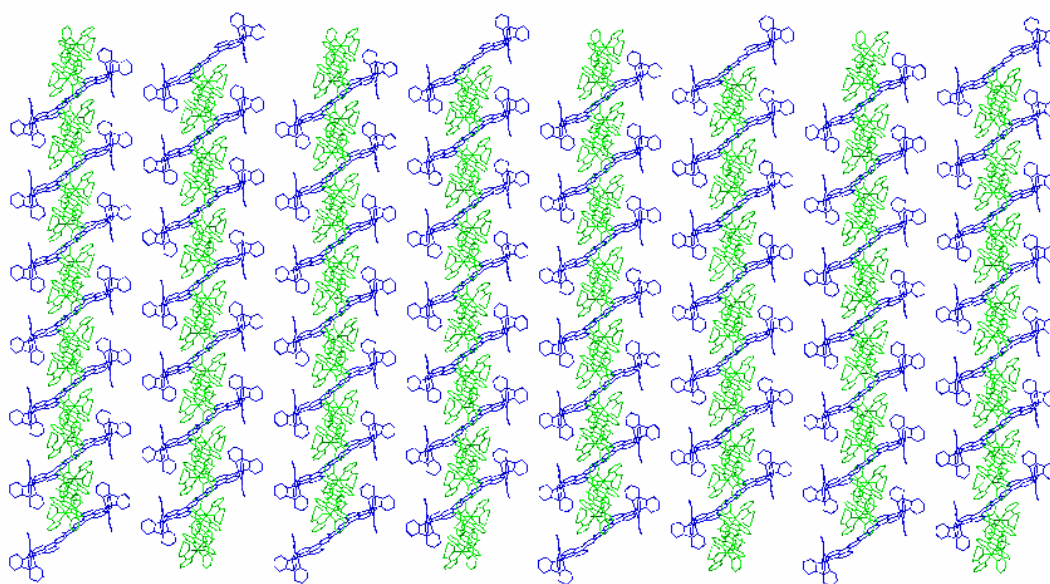


Figure 5.13 Expanded packing crystal structure of Q.

5.3.2 STM Evidence

As discussed in Chapter 3, we have obtained STM images of **P** on an HOPG substrate. These images were obtained in air under ambient conditions from a dried drop of a solution of **[P][CF₃SO₃]₄** in MeCN. As shown in Figure 5.14, even in the absence of solvent, there is clear evidence for the tendency of **P** to form columnar stacks. The parallel alignment along the bridging ligand is consistent with our π - π stacking model. Considering the fact that these stacks are evident under solventless conditions, we believe that there is even greater potential for achieving long-range ordering with the solubilized species.

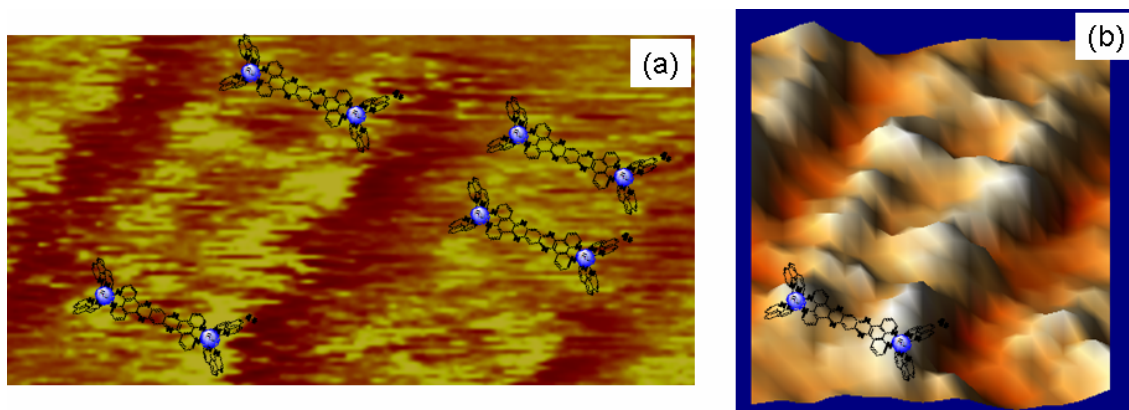


Figure 5.14 STM images of **P** on HOPG: (a) 2-D Surface plot, 11 x 5 nm, $I = 64$ pA, Bias = 750 mV; (b) 3-D Contour plot of the same image.

5.3.3 NMR Evidence

Additionally, the aggregation phenomenon is observable using NMR spectroscopy. As shown in Figure 5.15, the ^1H NMR spectra for **P** in D_2O has broad peaks, which is itself an indicator of aggregation. In addition, the spectra change with

respect to concentration. At higher concentrations, the peaks become increasingly broad, and some peaks shift upfield.

This behavior closely matches that described by Bolger, et. al. for mononuclear ruthenium complexes containing the tpphz ligand.¹⁰⁴ The concentration-induced chemical shifts have been attributed to aggregation of the species by π - π stacking along the tpphz ligand in solution. The local electron density in the vicinity of the tpphz ligand is modified as a result of aggregation, which must be very rapid with respect to the NMR time scale.

For complex **P**, the most pronounced shift is that of the furthest downfield peak, which varies in position from 9.47 ppm to 9.20 ppm between concentrations of 1 mM and 4 mM. This downfield peak corresponds to the protons found on the central portion of the tatpp bridging ligand. In other words, the protons that are the most perturbed by the aggregate formation are those located at the center of the complex. This further supports the π - π stacking model in that these are the protons whose environment is expected to be most affected by stacking along the bridging ligand.

Importantly, these NMR data clearly demonstrate a direct relationship between concentration and aggregation. We observe an increase in peak broadening and shifting as a function of concentration. Essentially, a more concentrated solution shows a more pronounced aggregation effect. As a result, we can use concentration as a method of controlling the degree of aggregation.

Interestingly, this behavior was not observed in acetonitrile. In MeCN, the peaks are sharp and there is no significant change in peak position due to concentration.

We attribute this to the effect of solvent polarity. A polar solvent (D_2O) promotes aggregation due to the presence of the aromatic bridging ligand in **P**. The organic backbone of the ligand is made up of a series of interconnected benzene rings. This non-polar segment will exhibit hydrophobic behavior and in order to compensate, the molecule stacks. This closely-packed, stacked aggregate excludes water from its structure, affording each molecule a less polar environment. In a less polar solvent like MeCN, this driving force is not present and we do not observe as significant an aggregation effect.

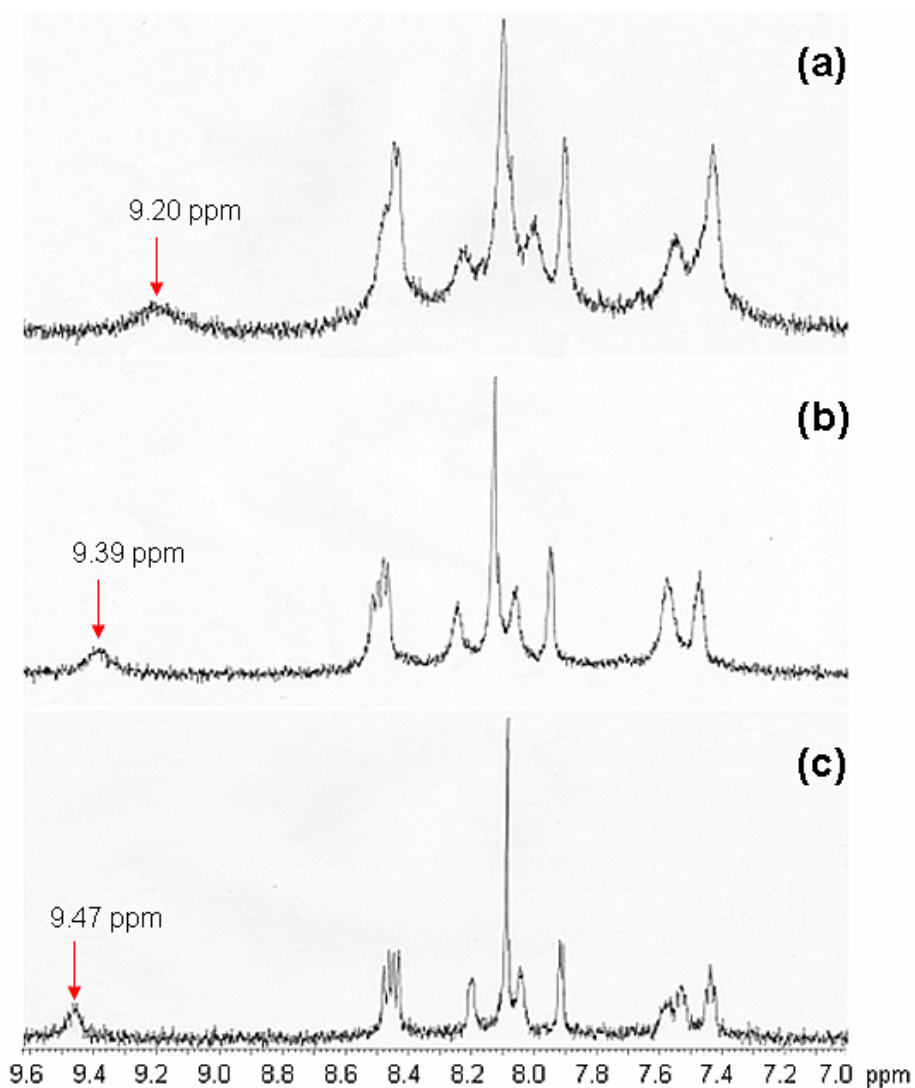


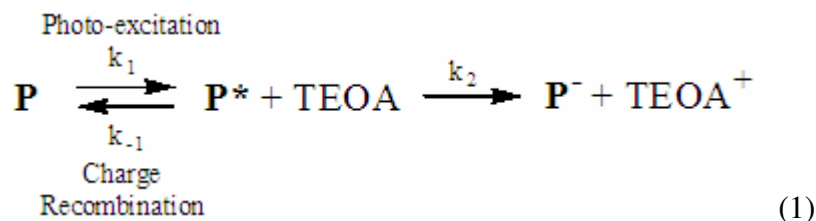
Figure 5.15 Partial proton NMR spectra (500 MHz, 298 K) of **P** in D₂O at concentrations of (a) 4 mM, (b) 2 mM, and (c) 1 mM.

5.4 Aggregation (Via Concentration) and Reduction

In order to examine the effect of aggregation on the kinetics of the photochemical reduction, we examined the rate of photoproduct formation (**P'**) in samples where the degree of aggregation was controlled by adjusting the concentration.

We expect these aggregation-induced effects to be evident in the *rate constants* for the reactions.

The rate constants of interest will be derived from the following overall reaction:



where the effective $[\text{P}^*]$ is related to the initial $[\text{P}]$, incident photon flux, the quantum efficiency of formation of the excited state, the rate of charge recombination and the rate of reductive quenching with TEOA. The rate law for the formation of P^- in equation 1 can be expressed most easily in terms of $[\text{P}^*]$ as shown below in equation 2:

$$\text{rate} = k_2[\text{P}^*][\text{TEOA}] - k_{-1}[\text{P}^*] \quad (2)$$

If we conduct our experiments such that the incident photon flux, the absorbance of the solution of P , and the quantum efficiency of generating the excited state P^* are constant, these factors can be expressed in a single constant, k_1 . We can also assume that $k_1 \gg k_{-1}$ and k_2 as the photon flux and optical density of the experiment are deliberately high and the quantum efficiency of generating the $^3\text{MLCT}$ state in ruthenium trisdiimine complexes is generally near unity. Given these assumptions, we can apply the steady-state hypothesis to express the $[\text{P}^*]$ in terms of $[\text{P}]$ as shown below:

$$\text{P} \leftrightarrow \text{P}^* \quad K = k_1/k_{-1} = [\text{P}^*]/[\text{P}] \quad (3)$$

If we are only concerned about relative rates, we can set k_1 to 1 and simplify and rearrange expression 3 to get:

$$[\mathbf{P}^*] = (1/k_{-1})[\mathbf{P}] \quad (4)$$

And substitution of this into expression 2 yields:

$$\text{rate} = k_2(1/k_{-1})[\mathbf{P}][\text{TEOA}] - k_{-1}(1/k_{-1})[\mathbf{P}] \quad (5)$$

which simplifies to:

$$\text{rate} = ((k_2/k_{-1})[\text{TEOA}] - 1) [\mathbf{P}] \quad (6)$$

Under conditions where the [TEOA] is present in large excess, pseudo-first order conditions apply and equation 6 further simplifies to:

$$\text{rate} = (k_2/k_{-1} - 1) [\mathbf{P}] \quad (7)$$

thus if the rate data can be fit to a first-order rate law, such as equation 8

$$\text{rate} = k_{\text{obs}}[\mathbf{P}] \quad (8)$$

then $k_{\text{obs}} = k_2/k_{-1} - 1$. If we assume the k_2 is unaffected by the aggregation, then any increase in the rate of photoreduction can be attributed to a decrease in the rate of charge recombination k_{-1} . As reported in our earlier studies using transient absorption spectroscopy, the charge recombination rate (k_{-1}) is strongly dependent on the solvent polarity and therefore is likely to be affected by aggregation effects. Aggregates of \mathbf{P} should experience a local environment that is less polar than that of pure water as the π - π stacking will effectively exclude an appreciable amount of water from the central tatpp bridging ligand and, we postulate, experience slower charge recombination (smaller k_{-1}). On the other hand, the site of TEOA oxidation is at the ruthenium ends of the complex which are not appreciably shielded due to aggregate formation. Thus we can assume that k_2 may be largely unaffected and most of any observed change in k_{obs} is due to changes in the value of k_{-1} (due to aggregation).

5.4.1 Kinetics of Photoreduction with Respect to Aggregation

The photoreduction of **P** in water by TEOA was examined at two concentrations of **P**, differing by a factor of 10 (16 μM and 160 μM). In order to maintain the same absorption level in both samples, the two photoreactions were performed in cells with pathlengths of 1 mm (for the 160 μM solution) or 10 mm (for the 16 μM solution). At these concentrations and pathlengths, the absorbance of both solutions at the MLCT peak (450 nm) was 0.87 AU. Although it would have been desirable, it was not possible to examine solutions at the concentrations examined in the NMR study, as these solutions would be opaque even in the 1 mm cell. Both solutions, were incubated in a water bath at 18 ± 1 °C and irradiated by the same lamp in the same geometry. The [TEOA] was 0.1 M for both. The formation of the **P**[•] was monitored by measuring the absorbance change of the solution as a function of time at 980 nm.

Plots of the natural log of absorbance versus time for both concentrations are shown in Figure 5.16. The error bars indicate the standard deviation of the data from a summation of three runs. A linear response would be indicative of a first-order (or pseudo first-order) reaction. While both sets of data show some small curvature, they can easily be fit with a line from which k_{obs} is extracted. The k_{obs} for the less concentrated solution (presumably less aggregated) is $3.94 \times 10^{-3} \text{ s}^{-1}$ whereas the k_{obs} for the more concentrated solution (160 μM) is $9.28 \times 10^{-3} \text{ s}^{-1}$. The absolute value of these rate constants is meaningless as they only report relative rates; however, the difference between the two is significant. The k_{obs} for the 160 μM solution is 2.35 times

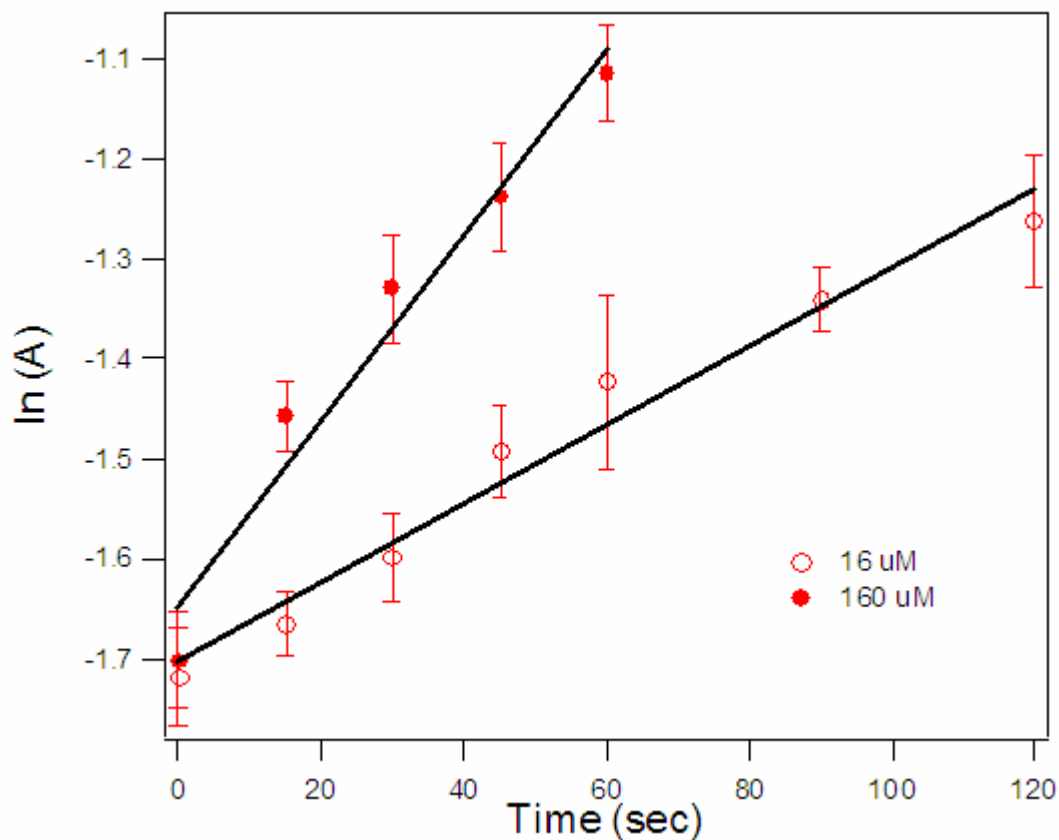


Figure 5.16 Plot of the kinetic data for photoreduction of **P** at concentration of 16 μM (open dots) and 160 μM (closed dots). Conditions: 100 W tungsten bulb (light source), 0.1 M Triethanolamine, 18 $^{\circ}\text{C}$.

larger than that for the 16 μM solution. The fact that there is a change in the rate constants is indicative of a change to the fundamental process of photoreduction. The observation of an increase in the rate constant for the more concentrated solution is in line with our predictions and thus supportive of our hypothesis that aggregation can enhance of the photochemical reactivity of this complex. This is an exciting result in that we can now show that a supramolecular phenomenon such as π - π stacking can be used to alter the photochemical reactivity of a photoactive species. Furthermore, it

suggests that self-assembly processes (such as π - π stacking) may allow certain types of functionality (photochemical reactivity) to exist under conditions that nominally would either kill or strongly attenuate this function. In this case, the photochemical reactivity of **P** is not as strongly attenuated in aqueous solution as studies of the excited state lifetime in polar and non-polar solvents would suggest. In fact, we observe that it is possible to enhance the photochemical activity simply by favoring aggregate formation.

5.4.2 Electrochemistry

Electrochemical experiments provide us with further evidence that aggregation facilitates the reduction of **P**. Differential pulse voltammetry scans of **P** at increasing concentrations were conducted studying the first electron reduction of the species, the formation of **P**^{•-}. As shown in Figure 5.17, as the solution concentration was increased from approximately 160 μ M to 250 μ M, the reduction potential decreased from -0.275 V to -0.235 V. These data suggest that as the degree of aggregation increases, complex **P** becomes easier to reduce. We attribute this effect to a delocalization of the reduction electron throughout the stacked aggregate.

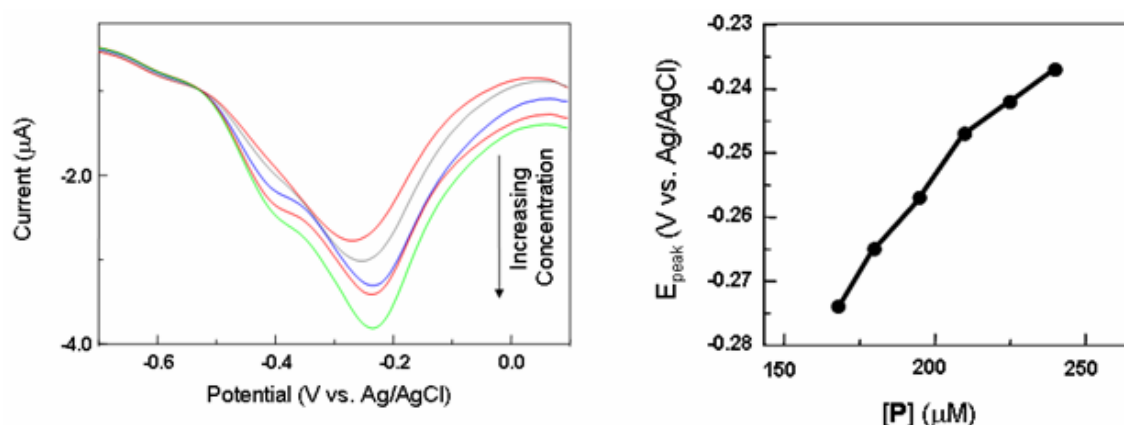


Figure 5.17 DPV of the first **P** reduction with increasing concentration (left); Plot of first reduction potential as a function of $[P]$ (right).

5.5 Aggregation (Via Ionic Strength)

To further study the effects of aggregation on the behavior of **P**, an alternate method of inducing aggregation was investigated. Ionic strength has been shown to be an important factor in molecular aggregation.¹⁰⁵ Solutions of increased ionic strength help to screen intermolecular electrostatic repulsions, which can be a barrier to aggregation. With respect to **P**, solutions of high ionic strength should compensate for the positive charges on the ruthenium atoms, making aggregation more favorable.

5.5.1 NMR

To verify that ionic strength promotes aggregation of **P**, a ^1H NMR spectrum was collected of a solution of **P** in D_2O , containing 0.1 M NaCl. As shown in Figure 5.18, the peaks appear extremely broad, which we know to be an indication of aggregation.

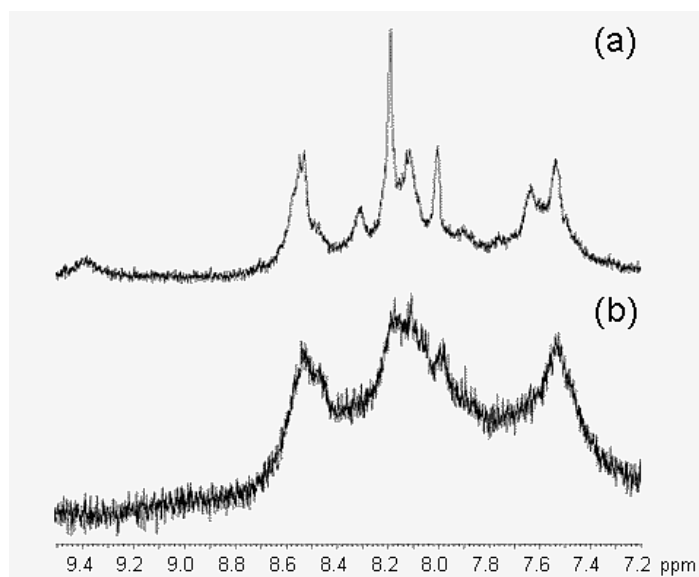


Figure 5.18 Partial proton NMR spectra (500 MHz, 298 K) of 2 mM **P** in D₂O with (a) no added NaCl and (b) 0.1 M NaCl.

5.5.2 Mass Spectroscopy

To verify the effect of ionic strength on the aggregation of **P**, two samples were submitted for mass spectroscopy. One sample contained **P** only, and the second sample was a mixture of **P** and NaCl. As seen in Figure 5.19, there is a distinct difference between the two spectra, where significantly more species of high mass were detected in the NaCl sample. For the **P** sample, the major peaks were detected at m/z ratios of 352 and 480, which correspond to the charged species of $[\text{Ru}_2(\text{phen})_4(\text{tatpp})]^{4+}$ and $[\text{Ru}_2(\text{phen})_4(\text{tatpp})]\text{Cl}^{3+}$ respectively.

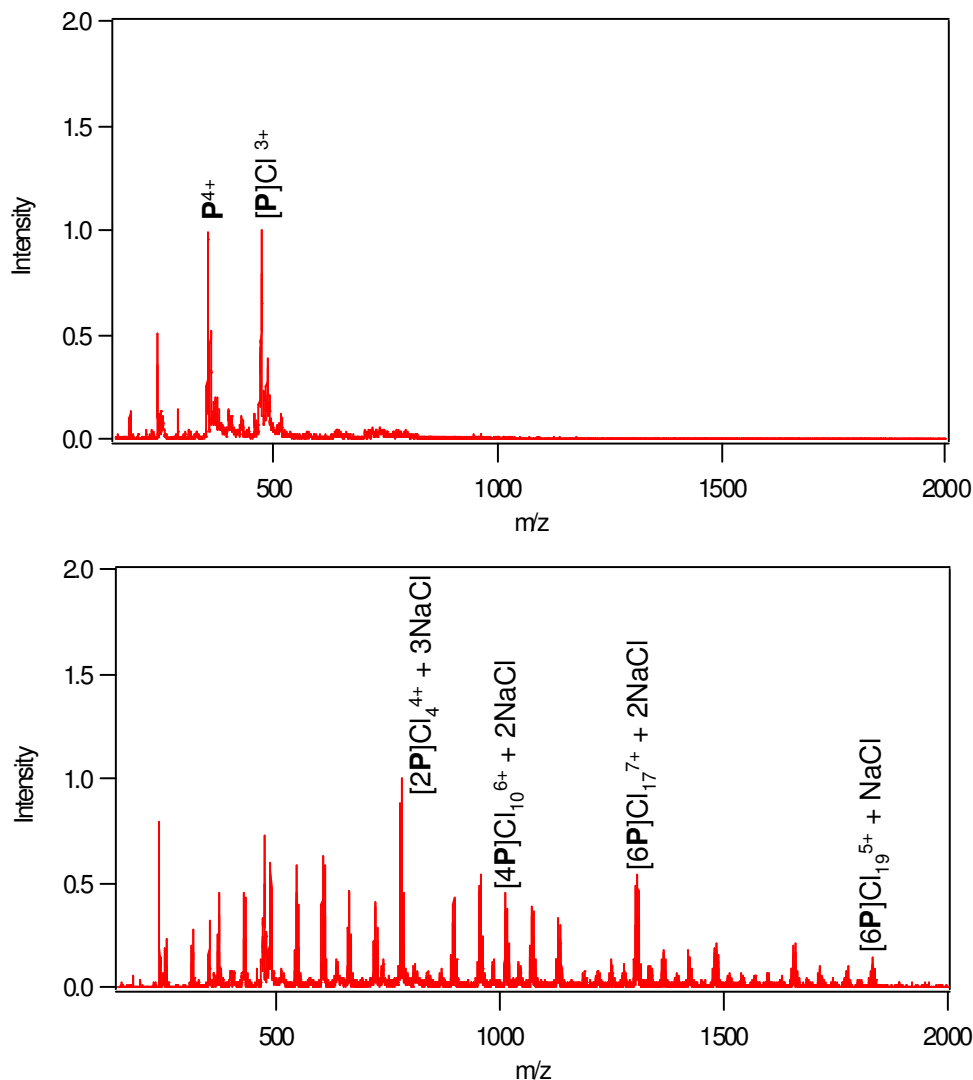


Figure 5.19 ESI-Mass Spectra for **P** (top) and **P** with NaCl (0.01 M) (bottom).

For the sample containing NaCl, many additional peaks are observed which presumably indicates the formation of aggregates. Mass spectra obtained for related ruthenium polypyridyl complexes (in the absence of salt) have never contained species with such high m/z values. The most abundant fragment is detected at an m/z ratio of 782. Interestingly, this matches a combination of two **P** molecules closely associated

with 3 molecules of NaCl, $([2 \text{ Ru}_2(\text{phen})_4\text{tatpp}]\text{Cl}_4^{4+} + 3\text{NaCl})^{4+}$. Other identifiable components include aggregates of 4 and 6 molecules of **P**.

5.5.3 Photochemistry

Using increased ionic strength to promote aggregation of **P**, its effect on the photochemical kinetics was determined. We expected to see a result that agreed with the previous study where concentration-directed aggregation resulted in a faster rate of reduction. However, this was not the case, and no appreciable effect was observed. As shown in Figure 5.20, the rate of reduction of **P** is virtually unchanged upon the addition of NaCl to the solution. The calculated rate constants for 0.0 M NaCl, 0.01 M NaCl, and 0.1 M NaCl were found to be $4.03 \times 10^{-3} \text{ s}^{-1}$, $3.98 \times 10^{-3} \text{ s}^{-1}$, and $3.89 \times 10^{-3} \text{ s}^{-1}$ respectively. With errors for each calculation approximately ± 0.0005 , the differences are not significant.

The lack of appreciable difference in k_{obs} for the three experiments suggests that not all the assumptions used in the concentration-induced aggregation study of **P** hold here. The NMR and ESI-MS data clearly show that aggregation is occurring upon addition of NaCl and, in fact, the ESI-MS data suggests these aggregates are intrinsically more stable when extraneous salt is added. We do not fully understand why the photochemistry is so insensitive to this change, however, we speculate that the bimolecular rate constant k_2 is being strongly attenuated due to restricted access to the transient Ru^{3+} site. In this case the build-up of counterions in the second and possibly even third coordination sphere about the Ru site is possibly limiting how closely the

TEOA can approach this site. If this is the case, our prior assumption that k_2 is unaffected by aggregation would not hold.

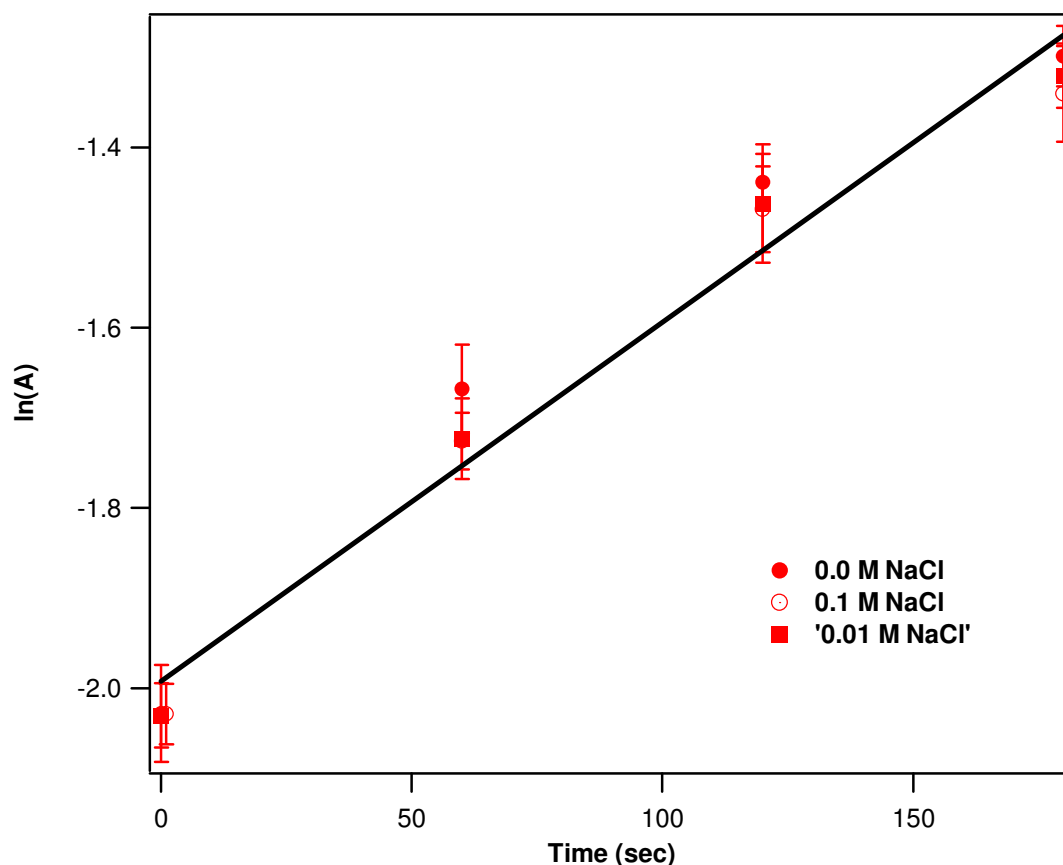


Figure 5.20 Plot of the kinetic data for the photoreduction of **P** at different ionic strengths. Conditions: 100 W tungsten bulb (light source), 16 μ M **P**, 0.1 M Triethanolamine, 18 $^{\circ}$ C.

5.6 Summary and Conclusion

Based on the known behavior of related complexes, we believe that the quaternary structure of complex **P** is a π - π stacked, columnar arrangement. The degree of this aggregation can be varied with changes in concentration or ionic strength. Since

the photochemistry of **P** involves a solvent-sensitive ^3LC state, aggregation may be able to affect the rate at which photoreduction occurs.

We expected to observe enhanced kinetics upon aggregation, but ultimately, the results proved inconclusive. For concentration-induced aggregation, the data support our hypothesis showing that the photoreduction is almost 2.5 times faster when the complex is more strongly aggregated. Electrochemical data also support this effect, showing a lowering of the first reduction potential as concentration (thus, aggregation) increases.

Unfortunately, ionic-strength-induced aggregation does not demonstrate the same behavior. We observed no change in the photoreduction between samples at varying ionic strengths. While NMR and mass spectroscopy data suggest the presence of aggregates, there is no observable affect on the photochemistry of **P**.

REFERENCES

- (1) Nogales, E.; Wolf, S. G.; Downing, K. H. *Nature* **1998**, *391*, 199-203.
- (2) Nogales, E.; Whittaker, M.; Milligan, R. A.; Downing, K. H. *Cell* **1999**, *96*, 79-88.
- (3) Goodsell, D. S.; Olson, A. J. *Trends Biochem. Sci* **1993**, *18*, 65-68.
- (4) Goodsell, D. S. *American Scientist* **2000**, *88*, 230-237.
- (5) Lehn, J.-M. *Angew. Chem. Int. Ed.* **1988**, *27*, 89-112.
- (6) Lehn, J.-M. *Supramolecular Chemistry, Concepts and Perspectives*; VCH: New York, 1995.
- (7) Whitesides, G. M.; Grzybowski, B. *Science* **2002**, *295*, 2418-2421.
- (8) Gellman, S. H. *Chem. Rev.* **1997**, *97*, 1231-1232.
- (9) MacGillivray, L. R.; Atwood, J. L. *Angew. Chem. Int. Ed.* **1999**, *38*, 1018-1033.
- (10) Zimmermann, S. C.; Wendland, M. S.; Rakow, N. A.; Zharov, I.; Suslick, K. S. *Nature* **2002**, *418*, 399-403.
- (11) Spillmann, H.; Dmitriev, A.; Lin, N.; Messina, P.; Barth, J. V.; Kern, K. *J. Am. Chem. Soc.* **2003**, *125*, 10725-10728.
- (12) Li, X.; Sinks, L. E.; Rybtchinski, B.; Wasielewski, M. R. *J. Am. Chem. Soc.* **2004**, *126*, 10810-10811.
- (13) Kim, M.-J.; MacDonnell, F. M.; Gimon-Kinsel, M. E.; DuBois, T.; Asgharian, N.; Griener, J. C. *Angew. Chem. Int. Ed.* **2000**, *39*, 615-619.
- (14) Gut, D.; Rudi, A.; Kopilov, J.; Goldberg, I.; Kol, M. *J. Am. Chem. Soc.* **2002**, *124*, 5449-5456.
- (15) Nguyen, T. Q.; Martel, R.; Avouris, P.; Bushey, M. L.; Brus, L.; Nuckolls, C. *J. Am. Chem. Soc.* **2004**, *126*, 5234-5242.

- (16) Percec, V.; Glodde, M.; Bera, T. K.; Miura, Y.; Shiyanovskaya, I.; Singer, K. D.; Balagurusamy, V. S. K.; Heiney, P. A.; Schnell, I.; Rapp, A.; Spiess, H.-W.; D., H. S.; Duan, H. *Nature* **2002**, *419*, 384 - 387.
- (17) Kamikawa, Y.; Nishii, M.; Kato, T. *Chem. Eur. J.* **2004**, *10*, 5942-5951.
- (18) Campagna, S.; Giannetto; Serroni, S.; Denti, G.; Trusso, S.; Mallamace, F.; Micali, N. *J. Am. Chem. Soc.* **1995**, *117*, 1754-1758.
- (19) MacDonnell, F. M.; Bodige, S. *Inorg. Chem.* **1996**, *35*, 5758-5759.
- (20) Gillard, R. D.; Hill, R. E. E.; Maskill, R. *J. Chem. Soc. (A)* **1970**, 707.
- (21) Gillard, R. D.; Hill, R. E. E.; Maskill, R. *J. Chem. Soc. (A)* **1970**, 1447.
- (22) Torres, A. S.; Maloney, D. J.; Tate, D.; MacDonnell, F. M. *Inorg. Chim. Acta.* **1999**, *293*, 37-43.
- (23) MacDonnell, F. M.; Kim, M.-J.; Bodige, S. *Coord. Chem. Rev.* **1999**, *185-186*, 535-549.
- (24) Kim, M.-J. In *Chemistry and Biochemistry*; University of Texas at Arlington: Arlington, TX, 2000.
- (25) Asgharian, N.; Wu, X.; Meline, R. L.; Derecskei, B.; Cheng, H.; Schelly, Z. A. *J. Mol. Liq.* **1997**, *72*, 315-322.
- (26) Hiort, C.; Lincoln, P.; Nordén, B. *J. Am. Chem. Soc.* **1993**, *115*, 3448-3454.
- (27) Bodige, S.; MacDonnell, F. M. *Tetrahedron Lett.* **1997**, *38*, 8159-8160.
- (28) Maloney, D. J.; MacDonnell, F. M. *Acta Cryst, Sec. C.* **1997**, *C53*, 705-707.
- (29) Gallagher, M. J.; Chen, D.; Jacobsen, B. P.; Sarid, D.; Lamb, L. D.; Tinker, F. A.; Jiao, J.; Huffman, D. R.; Seraphin, S. *Surf. Sci.* **1993**, *281*, L335-L340.
- (30) LeRoy, B. J.; Kong, J.; Pahilwani, V. K.; Dekker, C.; Lemay, S. G. *Phys. Rev. B: Condens. Matter* **2005**, *72*, 0754131-0754135.
- (31) Rivera, W.; Perez, J. M.; Ruoff, R. S.; Lorents, D. C.; Malhotra, R.; Lim, S.; Rho, Y. G.; Jacobs, E. G.; Pinizzotto, R. F. *J. Vac. Sci. Technol., B* **1995**, *13*, 327-330.

- (32) Lemay, S. G.; Janssen, J. W.; van den Hout, M.; Mooij, M.; Bronikowski, M. J.; Willis, P. A.; Smalley, R. E.; Kouwenhoven, L. P.; Dekker, C. *Nature* **2001**, *412*, 617-620.
- (33) Albrecht, P. M.; Lyding, J. W. *Superlattices Microstruct.* **2004**, *34*, 407-412.
- (34) Kowalczyk, P.; Klusek, Z.; Kozłowski, W.; Byszewski, P.; Olejniczak, W. *Appl. Phys. A* **2007**, *87*, 37-40.
- (35) Patole, S. N.; Pike, A. R.; Connolly, B. A.; Horrocks, B. R.; Houlton, A. *Langmuir* **2003**, *19*, 5457-5463.
- (36) Zareie, M. H.; Lukins, P. B. *Biochem. Biophys. Res. Commun.* **2003**, *303*, 153-159.
- (37) Hietschold, M.; Lackinger, M.; Griessl, S.; Heckl, W. M.; Gopakumar, T. G.; Flynn, G. W. *Microelectron. Eng.* **2005**, *82*, 207-214.
- (38) Iyer, V. S.; Yoshimura, K.; Enkelmann, V.; Epsch, R.; Rabe, J. P.; Mullen, K. *Angew. Chem. Int. Ed.* **1998**, *37*, 2696-2699.
- (39) Samori, P.; Simpson, C. D.; Mullen, K.; Rabe, J. P. *Langmuir* **2002**, *18*, 4183-4185.
- (40) Samori, P.; Severin, N.; Simpson, C. D.; Mullen, K.; Rabe, J. P. *J. Am. Chem. Soc.* **2002**, *124*, 9454-9457.
- (41) Ulrich, Z.; Jean-Marie, L.; Ahmed, M.; Martin, M. *Chem. Eur. J.* **2002**, *8*, 951-957.
- (42) Qiu, X.; Wang, C.; Zeng, Q.; Xu, B.; Yin, S.; Wang, H.; Xu, S.; Bai, C. *J. Am. Chem. Soc.* **2000**, *122*, 5550-5556.
- (43) Wei, Z.; Guo, S.; Kandel, S. A. *J. Phys. Chem. B* **2006**, *110*, 21846-21849.
- (44) Hudson, J. E.; Abruna, H. D. *J. Phys. Chem.* **1996**, *100*, 1036-1042.
- (45) Messina, P.; Dmitriev, A.; Lin, N.; Spillmann, H.; Abel, M.; Barth, J.; Kern, K. *J. Am. Chem. Soc.* **2002**, *124*, 14000-14001.
- (46) Yung, K. C.; Vess, T. M.; Myrick, M. L. *NATO ASI Ser., Ser. C* **1992**, *374*, 1171-1176.

- (47) Latterini, L.; Pourtois, G.; Moucheron, C.; Lazzaroni, R.; Bredas, J.-L.; Mesmaeker, A. K.-D.; De Schryver, F. C. *Chem. Eur. J.* **2000**, *6*, 1331-1336.
- (48) Figgemeier, E.; Merz, L.; Hermann, B. A.; Zimmermann, Y. C.; Housecroft, C. E.; Guentherodt, H. J.; Constable, E. C. *J. Phys. Chem. B* **2003**, *107*, 1157-1162.
- (49) Sasahara, A.; Pang, C. L.; Onishi, H. *J. Phys. Chem. B* **2006**, *110*, 4751-4755.
- (50) Kim, M.-J.; Konduri, R.; Ye, H.; MacDonnell, F. M.; Puntoriero, F.; Serroni, S.; Campagna, S.; Holder, T.; Kinsel, G.; Rajeshwar, R. *Inorg. Chem.* **2002**, *41*, 2471-2476.
- (51) Adeyemi, S. A.; Johnson, E. C.; Miller, F. J.; Meyer, T. J. *Inorg. Chem.* **1973**, *12*, 2371-2374.
- (52) MacDonnell, F. M.; Ali, M. M.; Kim, M.-J. *Comm. Inorg. Chem.* **2000**, *22*, 203-225.
- (53) Wang, D.; Xu, Q.-M.; Wan, L.-J.; Wang, C.; Bai, C.-L. *Langmuir* **2002**, *18*, 5133-5138.
- (54) Dretschkow, T.; Lampner, D.; Wandlowski, T. *J. Electroanal. Chem.* **1998**, *458*, 121-138.
- (55) Cunha, F.; Jin, Q.; Tao, N. J.; Li, C. Z. *Surf. Sci.* **1997**, *389*, 19-28.
- (56) Shoute, L. C. T.; Loppnow, G. R. *J. Am. Chem. Soc.* **2003**, *125*, 15636-15646.
- (57) Zhu, Y.; Jenekhe, S. A. *Polym. Prepr.* **2004**, *45*, 176-177.
- (58) Semenov, A.; Spatz, J. P.; Lehn, J.-M.; Weidl, C. H.; Schubert, U. S.; Möller, M. *Appl. Surf. Sci.* **1999**, *144-145*, 456-460.
- (59) Nakamura, T.; Matsumoto, T.; Tada, H.; Sugiura, K.-I. In *Chemistry of Nanomolecular Systems*; Schaefer, F. P., Toennies, J. P., Zinth, W., Eds.; Springer: Berlin, 2003; Vol. 70, pp 5-8.
- (60) Aviram, A.; Ratner, M. A. *Chem. Phys. Lett.* **1974**, *29*, 277-283.
- (61) Aviram, A. *J. Am. Chem. Soc.* **1988**, *110*, 5687.

- (62) Bachtold, A.; Hadley, P.; Nakanishi, T.; Dekker, C. *Science* **2001**, *294*, 1317.
- (63) Huang, Y.; Duan, X.; Cui, Y.; Lauhon, L. J.; Kim, K.-H.; Lieber, C. M. *Science* **2001**, *294*, 1313.
- (64) Reed, M. A. *Proc. IEEE* **1999**, *87*, 652.
- (65) Joachim, C.; Gimzewski, J. K.; Aviram, A. *Nature* **2000**, *408*, 541.
- (66) Tour, J. M.; Kozaki, M.; Seminario, J. M. *J. Am. Chem. Soc.* **1998**, *120*, 8486.
- (67) Zhou, C.; Deshpande, M. R.; Reed, M. A.; Jones, L.; Tour, J. M. *Appl. Phys. Lett.* **1997**, *71*, 611-613.
- (68) Chen, J.; Reed, M. A.; Rawlett, A. M.; Tour, J. M. *Science* **1999**, *286*, 1550.
- (69) Reed, M. A.; Chen, J.; Rawlett, A. M.; Price, D. W.; Tour, J. M. *App. Phys. Lett.* **2001**, *78*, 3735-3737.
- (70) Noh, Y.-Y.; Kim, J.-J.; Yase, K.; Nagamatsu, S. *Appl. Phys. Lett.* **2003**, *83*, 1243-1245.
- (71) Yamamoto, T.; Sakai, Y.; Aramaki, S. *Bull. Chem. Soc. Jpn.* **2006**, *79*, 959-961.
- (72) Ghosh, B. K.; Chakravorty, A. *Coord. Chem. Rev.* **1989**, *95*, 239.
- (73) Lahiri, G. K.; Bhattacharya, S.; Mukherjee, A. K.; Chakravorty, A. *Inorg. Chem.* **1987**, *26*, 3359.
- (74) Kalyanasundaram, K.; Nazeeruddin, M. K. *Inorg. Chim. Acta* **1994**, *226*, 213.
- (75) Harriman, A.; Sauvage, J.-P. *Chem. Soc. Rev.* **1996**, *25*, 41-48.
- (76) Kalyanasundaram, K.; Gratzel, M.; Pelizetti, E. *Coord. Chem. Rev.* **1986**, *69*, 57.
- (77) MacDonnell, F. M.; Kim, M.-J.; Wouters, K. L.; Konduri, R. *Coord. Chem. Rev.* **2003**, *242*, 47-58.
- (78) Parisse, P.; Picozzi, S.; Passacantando, M.; Ottaviano, L. *Thin Solid Films* **2007**, *515*, 8316-8321.

- (79) Mathur, S. C.; Kumar, B.; Roy, K. *Mol. Cryst. Liq. Cryst.* **1979**, *53*, 271-280.
- (80) Wolak, M. A.; Jang, B.-B.; Palilis, L. C.; Kafafi, Z. H. *J. Phys. Chem. B* **2004**, *108*, 5492-5499.
- (81) Mishra, L.; Yadaw, A. K.; Govil, G. *Indian J. Chem., Sect A* **2003**, *42A*, 1797-1814.
- (82) Grosshenny, V.; Harriman, A.; Hissler, M.; Ziessel, R. *Platinum Met. Rev.* **1996**, *40*, 26-35.
- (83) Buda, M.; Kalyuzhny, G.; Bard, A. J. *J. Am. Chem. Soc.* **2002**, *124*, 6090-6098.
- (84) Vos, J. G.; Kelly, J. M. *Dalton Trans.* **2006**, *41*, 4869-4883.
- (85) Welter, S.; Brunner, K.; Hofstraat, J. W.; De Cola, L. *Nature* **2003**, *421*, 54-57.
- (86) Janaratne, T. K. In *Chemistry and Biochemistry*; University of Texas at Arlington: Arlington, TX, 2006.
- (87) Jernigan, J. C.; Surridge, N. A.; Zvanut, M. E.; Silver, M.; Murray, R. W. *J. Phys. Chem.* **1989**, *93*, 4620-4627.
- (88) Surridge, N. A.; Zvanut, M. E.; Keene, F. R.; Sosnoff, C. S.; Silver, M.; Murray, R. W. *J. Phys. Chem.* **1992**, *96*, 962-970.
- (89) Maness, K. M.; Terrill, R. H.; Meyer, T. J.; Murray, R. W.; Wightman, R. M. *J. Am. Chem. Soc.* **1996**, *118*, 10609-10616.
- (90) Campagna, S.; Serroni, S.; Bodige, S.; MacDonnell, F. M. *Inorg. Chem.* **1999**, *38*, 692-701.
- (91) Kim, M.-J.; MacDonnell, F. M. *Unpublished results*.
- (92) Itoh, E.; Yamashita, T.; Miyairi, K. *Thin Solid Films* **2001**, *393*, 368-373.
- (93) Shannon, R. D. *Acta Crystallogr.* **1976**, *A32*, 751-767.
- (94) Yamada, M.; Hagiwara, H.; Torigoe, H.; Matsumoto, N.; Kojima, M.; Dahan, F.; Tuchagues, J.-P.; Re, N.; Iijima, S. *Chem. Eur. J.* **2006**, *12*, 4536-4549.

- (95) Aihara, Y.; Bando, T.; Nakagawa, H.; Yoshida, H.; Hayamizu, K.; Akiba, E.; Price, W. S. *J. Electrochem. Soc.* **2004**, *151*, A119-A122.
- (96) Webber, A. *J. Electrochem. Soc.* **1991**, *138*, 2586-2590.
- (97) Konduri, R.; Ye, H.; MacDonnell, F. M.; Serroni, S.; Campagna, S.; Rajeshwar, K. *Angew. Chem. Int. Ed.* **2002**, *41*, 3185-3187.
- (98) Konduri, R.; de Tacconi, N. R.; Rajeshwar, K.; MacDonnell, F. M. *J. Am. Chem. Soc.* **2004**, *126*, 11621-11629.
- (99) de Tacconi, N. R.; Lezna, R. O.; Konduri, R.; Onger, F.; Rajeshwar, K.; MacDonnell, F. M. *Chem. Eur. J.* **2005**, *11*, 4327-4339.
- (100) Chiorboli, C.; Fracasso, S.; Scandola, F.; Campagna, S.; Serroni, S.; Konduri, R.; MacDonnell, F. M. *Chem. Comm.* **2003**, 1658-1659.
- (101) Chiorboli, C.; Sandro, F.; Ravaglia, M.; Scandola, F.; Campagna, S.; Wouters, K. L.; Konduri, R.; MacDonnell, F. M. *Inorg. Chem.* **2005**, *44*, 8368-8378.
- (102) DeLaive, P. J.; Foreman, T. K.; Giannotti, C.; Whitten, D. G. *J. Am. Chem. Soc.* **1980**, *102*, 5627-5631.
- (103) Bolger, J.; Gourdon, A.; Ishow, E.; Launay, J.-P. *J. Chem. Soc., Chem. Comm.* **1995**, 1799-1800.
- (104) Bolger, J.; Gourdon, A.; Ishow, E.; Launay, J.-P. *Inorg. Chem.* **1996**, *35*, 2937-2944.
- (105) Majhi, P. R.; Ganta, R. R.; Vanam, R. P.; Seyrek, E.; Giger, K.; Dubin, P. L. *Langmuir* **2006**, *22*, 9150-9159.

BIOGRAPHICAL INFORMATION

Kelly Lyle Wouters was born on November 15th, 1975 in Vancouver, BC, Canada. He received a B.S. degree in Chemistry at The University of Texas at Austin in 1999. As a graduate student, he worked with Professor Frederick M. MacDonnell studying ruthenium polypyridyl complexes and their broad range of properties. In 2007, he received a Ph.D. in Chemistry at The University of Texas at Arlington.